UCLA

UCLA Electronic Theses and Dissertations

Title

Complex Heat Exchangers for Improved Performance

Permalink

https://escholarship.org/uc/item/4kv9n082

Author

Bran, Gabriela Alejandra

Publication Date

2016

Peer reviewed|Thesis/dissertation

UNIVERSITY OF CALIFORNIA

Los Angeles

Complex Heat Exchangers for Improved Performance

A dissertation submitted in partial satisfaction of the requirements for the degree Doctor of Philosophy in Mechanical Engineering

by

Gabriela Alejandra Bran

© Copyright by

Gabriela Alejandra Bran

ABSTRACT OF THE DISSERTATION

Complex Heat Exchangers for Improved Performance

by

Gabriela Alejandra Bran

Doctor of Philosophy in Mechanical Engineering
University of California, Los Angeles, 2016

Professor Hossein Pirouz Kavehpour, Co-Chair
Professor Adrienne Lavine, Co-Chair

A counter-flow heat exchanger transient one-dimensional numerical model was developed and verified against other authors results. Heat exchangers have been extensively studied due to their vast number of industrial applications where steady state operation is usually assumed. However, heat exchangers are also used in systems that operate under transient conditions such as energy generation, energy conversion, or energy storage.

After a detailed literature review, it was determined that there was a need for a more comprehensive study on the transient behavior of heat exchangers. Computational power was not readily available when most of the work on transient heat exchangers was done (1956 – 1986), so most of these solutions have restrictions, or very specific assumptions. More recently, authors have obtained numerical solutions for more general problems (2003 - 2013), but they have investigated very specific conditions, and cases. For a more complex heat exchanger (i.e. with heat generation), the transient solutions from literature are no longer valid. There was a need to develop a numerical

model that relaxes the restrictions of current solutions to explore conditions that have not been explored.

A one dimensional transient heat exchanger model was developed. There are no restrictions on the fluids and wall conditions. The model is able to obtain a numerical solution for a wide range of fluid properties and mass flow rates. Another innovative characteristic of the numerical model is that the boundary and initial conditions are not limited to constant values. The boundary conditions can be a function of time (i.e. sinusoidal signal), and the initial conditions can be a function of position. Four different cases were explored in this work. In the first case, the start-up of a system was investigated where the whole system is assumed to be at the same temperature. In the second case, the new steady state in case one gets disrupted by a smaller inlet temperature step change. In the third case, the new steady state in case one gets disrupted by a step change in one of the mass flow rates. The response of these three cases show that there are different transient behaviors, and they depend on the conditions imposed on the system. The fourth case is a system that has a sinusoidal time varying inlet temperature for one of the flows. The results show that the sinusoidal behavior at the inlet propagates along the channel. However, the sinusoidal behavior on one of the fluids does not fully translate to the other gets damped by the wall and the heat transfer coefficients that can be barely seen on the other flow.

A scaling analysis and a parametric study were performed to determine the influence the different parameters on the system have on the time a heat exchanger takes to reach steady state. The results show the dependency of t_{st}^* (time a system takes to reach steady state) on the dimensionless parameters M, C, NTU_h , NTU_c , and C_w . t_{st}^* depends linearly on C and C_w , and it is a power function of M. It was also shown that t_{st}^* has a logarithmic dependency on NTU_h and NTU_c . A correlation was generated to approximate the time a system takes to reach steady state

for systems where $C_{\rm w} << 1$.

A more complex heat exchanger with the specific application of solar energy storage was also investigated. This application involves a counter-flow heat exchanger with a reacting flow in one of the channels, and it includes varying properties, heat generation, varying heat transfer coefficient, and axial conduction. The application for this reactor heat exchanger is on solar energy storage, and the goals is to heat up steam to 650 °C by using the ammonia synthesis heat of reaction. One of the concerns for this system is the start-up time and also how disturbances in reacting flow can affect the steam outlet temperature. The transient behavior during the system start-up was presented. In order to achieve the desired outlet steam temperature at a reasonable time, the system must operate at high gas mass flow rates. If the inlet temperature of the gas suffers a step change, it affects the reaction rate as well as the outlet steam temperature. A small perturbation on the gas mass flow rate has an effect on the profile shape. However, the maximum temperature reached by the gas due to reaction is not affected, and consequently, it has little effect on the steam temperature.

Axial conduction in the reactor heat exchanger was also investigated, specifically in the gas section. Axial conduction cannot be assumed to be negligible in the reactor heat exchanger because of the iron-based catalytic bed. Results in this section show that axial conduction is detrimental for the system. It was found that for Peclet number greater than 100, axial conduction can be neglected. An alternative solution to address axial conduction was proposed, namely to include a well-insulated non-reacting section (without a catalytic bed) upstream of the reactor. The modified reactor heat exchanger was a novel solution to avoid the negative effect of axial conduction. Results show that by having a non-reacting section, axial conduction becomes unimportant.

The dissertation of Gabriela Alejandra Bran is approved.

Jeffrey Eldredge

Richard Wirz

Dante Simonetti

Hossein Pirouz Kavehpour, Committee Co-Chair

Adrienne Lavine, Committee Co-Chair

University of California, Los Angeles
2016

Dedicado a mis papás, Walter y Cecilia, y a mis hermanos Paola y Andre.

Table of Contents

Abstract of the Dissertation	ii
List of Figures	X
List of Tables	XV
Nomenclature	xvi
Acknowledgments	xix
Vita	xxi
Publications	xxi
Journal Publications	xxi
Conference Publications	xxi
Presentations	xxi
CHAPTER 1: Background on Transient Heat Exchangers	1
Motivation	1
Complex Heat Exchanger for Solar Energy Storage	1
Literature Review	3
CHAPTER 2: Numerical Model	12
Numerical Model	12
Assumptions	12
Differential Equations	12
Boundary and Initial Conditions	15

Nur	nerica	l Method	16
	Stab	ility	18
	Veri	fication of the numerical model	19
СН	APTI	ER 3: Numerical Experiments	25
Exp	lorati	on of transient behavior of a simple counter-flow heat exchanger	25
	Case	21: Step Change in Inlet Temperature – Effect of Start-up of System	26
	Case	2: Step Change in Inlet Temperature – Disturbance on Steady State Solution	30
	Case	e 3: Step Change in Inlet Mass Flow Rate – Disturbance on Steady State Solution	33
	Case	e 4: Time Varying Inlet Temperature of One of the Flows	34
	Con	clusion	37
Para	ametri	c Study for Time to Reach Steady State	37
	Proc	edure	38
	1.	Scaling Analysis	38
	2.	Parametric Study	39
	3.	General t_{st}^* Correlation	43
СН	APTI	ER 4: Counter Flow Reactor –Heat Exchanger Transient Behavior Analysis	46
Mot	tivatio	on	46
Am	monia	a-based Thermochemical Energy Storage System Concept	47
Nur	nerica	ll Model for Transient Reactor Heat Exchanger	49
Cvat	tem N	Iodeling	50

Reactor Heat Exchanger Model	
Verification of Numerical Model	56
Validation of the Model	57
Exploration of transient behavior of a complex counter-flow heat exchanger	60
Case 1: Start-up of the system – Inlet Gas Temperature	61
Case 2: Inlet Gas Temperature Disturbance	69
Case 3: Inlet Gas Mass Flow Rate Disturbance	72
Effect of Axial Conduction	75
Well-insulated Non-reacting Section	79
Effect of Gas Peclet Number	83
Summary	83
CHAPTER 5: Concluding Remarks and Future Research	85
Concluding Remarks	85
Future Work	89
1) Time a System takes to Reach Steady State	89
2) Modification of numerical model to analyze the dissociation receiver	90
Deferences	04

List of Figures

Figure 1 – Illustration of state-of-the-art molten salt CSP plant consisting of a solar field, TES, and
power block subcomponents. [3]
Figure 2 – Control volume analysis on a counter-flow heat exchanger which consists of the hot
fluid (orange), the wall (gray), and the cold fluid (blue).
Figure 3 – Equivalent thermal network of a counter flow heat exchanger [14]
Figure 4 - Counter flow heat exchanger with hot fluid entering through one end and cold fluid
entering through the opposite end. The fluids are separated by a wall, and the outer wall of the heat
exchanger is insulated
Figure 5 – Graphical representation of the grid. Solution will be obtained at different grid points
along the reactor length (x-axis) and at different points in time (y-axis)
Figure 6 – Geometry of the problem, domain of computations, and boundary conditions 20
Figure 7 – Energy balance for a transient one dimensional counter-flow heat exchanger model to
ensure energy conservation. Top graph: rate of heat as a function of time. Bottom graph: total rate
of heat as a function of time is always zero.
Figure 8 – Steady state solution for numerical model
Figure 9 – Comparison of Gvozdenac [10] results for verification of algorithm
Figure 10 - Steady state temperature of hot fluid (red continuous line), cold fluid (blue dashed
line), and the wall (green dotted line) for the following conditions: $M = 1$, $C = 1$, $C_w = 0.1$, NTU_h
$= 1, NTU_c = 1.$ 26
Figure 11 – Dimensionless temperature profiles as a function of dimensionless position for
different times: (a) the hot fluid, (b) the wall, and (c) the cold fluid for the following condition: M
$= 1 C = 1 C_{vv} = 0.1 NTU_b = 1 NTU_c = 1$

Figure 12 – Dimensionless temperature as a function of time for different x^* -locations for (a) the
hot dimensionless temperature, (b) the wall dimensionless temperature, and (c) the cold
dimensionless temperature
Figure 13 – Steady state temperature profiles before (dashed lines) and after (continuous lines) a
25% change in inlet temperature. Steady state temperature of hot fluid (red line), cold fluid (blue
line), and the wall (green line) for the following conditions: $M = 1$, $C = 1$, $C_w = 0.1$, $NTU_h = 1$,
$NTU_{c} = 1.$ 31
Figure 14 – Hot fluid temperature after reducing the inlet temperature of the hot fluid by 25% as a
function of x for specific times
Figure 15 - Transient behavior of hot fluid after a steady state solution is disturbed with a
temperature change at the inlet
Figure 16 – Steady state temperature profiles before (dashed lines) and after (continuous lines) a
25% decrease in hot fluid mass flow rate. Steady state temperature of hot fluid (red line), cold fluid
(blue line), and the wall (green line) for the following conditions: $C = 1$ and $C_w = 1$
Figure 17 – Time varying inlet temperature of the hot stream
Figure 18 – Dimensionless temperature of (a) hot fluid and (b) cold fluid as a function of time for
different x* locations
Figure 19 – Dimensionless hot temperature along the reactor for different dimensionless times.37
Figure 20 – Dimensionless time to reach steady state as a function of (a) M for $C = 1$ and $C = 2$,
and (b) C for $M = 1$ and $M = 2$. The following parameters were kept constant: $C_w = 0.1$, $NTU_h = 1$,
$NTU_{c} = 1.$ 41
Figure 21 – Dimensionless time the system takes to reach steady state as a function of (a) NTU_h
(left) and as a function of (b) NTU_c (right). The following parameters were kept constant: $M = 1$,

$C = 1, C_{\rm w} = 0.1.$ 42
Figure 22 – Dimensionless time the system takes to reach steady state as a function of $C_{\rm w}$. The
following parameters were kept constant: $M = 1$, $C = 1$, $NTU_h = 1$, and $NTU_c = 1$
Figure 23 $-t_{st}^*$ as a function of: (a) M , (b) C , (c) NTU_h and (d) NTU_c . Comparison between
numerical results and the correlation results
Figure 24 – Comparison between $t_{\rm st}^*$ numerical and correlation results
Figure 25 – Ammonia-based thermochemical energy storage system
$Figure\ 26-Schematic\ of\ the\ one\ dimensional\ radially\ lumped\ reactor\ heat\ exchanger\ model.\ .\ 50$
Figure 27 – Dimensions of small scale reactor heat exchanger
Figure 28 – Comparison of the steady state solution to a steady state problem (blue dashed lines)
and the solution to a transient problem (red starred lines). Left: mass fraction of N_2H_2 mixture as
a function of position x for different time steps. Right: gas temperature as a function of position x
for different time steps
Figure 29 – Side view geometry along the reactor heat exchanger build at UCLA [30] 57
Figure 30 – Reactor heat exchanger cross-sectional geometry
Figure 31 – Comparison between numerical results and experimental results for an ammonia based
reactor heat exchanger. Numerical results: gas temperature (red continuous line), inner wall (green
continuous line), outer wall (purple dashed line), and steam temperature (blue line). Experimental
results: gas temperature (red square markers), and steam temperature (blue square markers) 60
Figure 32 – Mass fraction of ammonia as a function of position for different time steps 63
Figure 33 – Mass fraction of ammonia as a function of time for different locations inside the
reactor
Figure 34 – Gas temperature as a function of position for different time steps. Error! Bookmark

not defined.

Figure 35 – Wall temperature as a function of position for different time steps
Figure 36 – Steam temperature as a function of position for different time steps
Figure 37 – Steady state temperature profiles of the gas, the steam, and the wall as a function of
axial position for a gas mass flow rate of 0.1 g/s and a steam mass flow rate of 0.08 g/s 66
Figure 38 – Left axis: Time the outlet steam temperature takes to reach steady state (blue axis) as
a function of gas mass flow rate for different initial gas temperatures. Right axis: Outlet steam
temperature (red axis) as a function of gas mass flow rate. Continuous red line is outlet steam
temperature from simulation, and dashed red line is the goal outlet steam temperature needed for
steam turbine. 68
Figure 39 - Steady state temperature of the gas (red), the wall (green), and the steam (blue) of
ammonia synthesis reactor heat exchanger as a function of position. Dashed line: Steady state
solution for a system with a gas inlet temperature of 600 °C. Continuous line: Steady state solution
after step change in gas inlet temperature from 600 °C to 512 °C
Figure 40 - Transient behavior after a step change in the inlet gas temperature of a steady state
system. (a) Ammonia mass fraction, (b) gas temperature, (c) steam temperature, and (d) wall
temperature as a function of position for different time steps
Figure 41 – Steady state temperature of the gas (red), the wall (green), and the steam (blue) of
ammonia synthesis reactor heat exchanger as a function of position. Dashed line: Steady state
solution for a system with a gas mass flow rate of 0.1 g/s. Continuous line: Steady state solution
after step change in gas mass flow rate to 0.075 g/s
Figure 42 – Transient behavior after step change in gas mass flow rate from 0.1 g/s to 0.075 g/s.
(a) Ammonia mass fraction, (b) gas temperature, (c) steam temperature, and (d) wall temperature

as a function of position for different time steps
Figure 43 – Effect of axial conduction on (a) the gas temperature, (b) the wall temperature, and
the (c) steam temperature
Figure 44 – Steady state temperature profiles for the gas (red), wall (green), and steam (blue) for
(a) no axial conduction and for (b) axial conduction ($Pe_g = 18$)
Figure 45 – Maximum dimensionless temperature of gas (red) and steam (blue) as a function of
gas Peclet number for an ammonia synthesis reactor heat exchanger
Figure 46 – Schematic of an ammonia synthesis reactor heat exchanger with a non-reacting section
at the beginning of the reactor.
Figure 47 – Steady state solution for a reactor heat exchanger with a non-reacting section length
of $x_{\rm uh} = 0.3$ m, with a gas mass flow rate of $\dot{m}_{\rm g} = 0.1{\rm g/s}$ for steam flow rate of $\dot{m}_{\rm g} = 0.08{\rm g/s}$.
Axial conduction was neglected. 81
Figure 48 – Temperature of the gas, the wall, and the steam as a function of position for different
effective thermal conductivities.
Figure 49 – Maximum dimensionless temperature of gas (red) and steam (blue) as a function of
gas Peclet number for an ammonia synthesis reactor heat exchanger with a non-reaction section.
83
Figure 50 – (a) Tower receiver with (b) concept sketch of dissociation receiver and (c) close view
of one of 80 individual panels
Figure 51 – Dimensions of the ammonia dissociation receiver, and the prescribed temperature at
the base of the receiver, along the dissociator tubes, and at the tip of the tubes

List of Tables

Table 1 – Dimensionless parameters proposed by Cima and London [5]	5
Table 2 – Solution for transient heat exchangers for $C^* = 0$.	9
Table 3 – Solutions for counter flow heat exchangers	10
Table 4 – Dimensionless parameters for system of equations describing the behavior of a transi	ent
heat exchanger.	.14
Table 5 – Dimensions of the ammonia dissociation receiver, and the prescribed temperature at	the
base of the receiver, along the dissociator tubes, and at the tip of the tubes.	. 92

Nomenclature

A	Pentagonal matrix in the system of linear equations $Ax = b$	-
$A_{\rm c}$	Cross-sectional Area	m^2
A_{s}	Surface area	m^2
Со	Courant number	-
D	Diameter	m
E_{a}	Activation Energy	J/mol
K_{a}	Equilibrium constant	
L	Length	m
M	Molar mass	kg/mol
Nu	Nusselt number	-
Pr	Prandtl number	-
P	Pressure	MPa
R	Universal gas constant	J/mol-K
$R_{ m tot}^{'}$	Total thermal resistance	m-K/W
Re	Reynolds number	-
T	Temperature	K or °C
a	Activity	-
b	Vector in the system of linear equations $Ax = b$	-
$c_{ m p}$	Specific heat	J/kg-K
f_{NH3}	Mass fraction	-
h	Heat transfer coefficient	W/m^2-K

k_0	Pre-exponential factor	kmol/s-m ³	
m	Number of time steps	-	
n	Exponent in eq. (6)	-	
ŗ'''	Rate of ammonia synthesis	kg/s-m ³	
t	Time	S	
$t_{ m st}$	Time $T_{s,o}$ takes to reach steady state	S	
$t_{ m d}$	Dwell time of C_{\min} fluid		
и	Velocity	m/s	
v	Number of grid size in x-direction	-	
$W_{ m i}$	Thickness of wall dividing the flows	m	
W_0	Thickness of the outer wall of reactor	m	
x	Position	m	
ho	Density	kg/m ³	
α	Exponent in Temkin-Pyzhev (Equation 57)	-	
$\eta_{ m o}$	Fin efficiency	-	
$\Delta h_{ m rxn}$	Enthalpy of reaction	J/kg	
Subscript or Superscript Symbols			
H_2	Hydrogen	-	
N_2	Nitrogen	-	
NH_3	Ammonia	-	
amb	ambient	-	
g	Gas mixture	-	
i	Inlet	-	

0	Outlet	-
pc	Pseudocritical	-
s	Steam	-
s,w	Steam property at wall temperature	-
0	Initial	-
h	Hot fluid	-
c	Cold fluid	-
W	Wall separating the two streams of heat exchanger	-
wi	Wall separating the two streams of reactor heat exchanger	-
wo	Outer wall of the reactor heat exchanger	
mix	Ammonia/Nitrogen-Hydrogen mixture	-
S	Steam	-
uh	Non-reacting	-

Acknowledgments

First, I would like to thank my parents, Cecilia and Walter Bran who have always believed in me and supported me unconditionally. They went through rough times to be able to give me and my siblings the best opportunities in life. They gave me the strength to pursue my dreams no matter how impossible they seemed. I also want to thank my sister Paula Bran who has been my role model and best friend since we were little girls. I would also like to thank my little brother, Andre Bran, because even in his odd way he has always been there in the important steps in my life.

I would like to thank my committee for always having the door open for any questions or concerns I had during my PhD work. I decided to continue my doctorate degree the day Prof. Wirz gave me the opportunity to join his lab. He has supported me throughout the years even after I was not working directly with him. For that, I will always be thankful. I admire Prof. Eldredge's work and ethics, and I was lucky to have him as my committee member and as a professor. Prof. Simonetti was always very helpful with every silly question I had on GC analysis, and he have me valuable advice for my future endeavors. Prof. Kavehpour welcomed me to his lab where I met some of my closest friends. He would always listen when I had any concern, and always had my back when I was struggling. I know I can always count on him. Finally, I would like to thank Prof. Lavine. She still doesn't believe me, but I wouldn't have finished my Ph.D. if it wasn't for her. Meeting with her once a week was the highlight of my week, because I could admire her train of thought, and how she tackles any problem she is given. She gave me career and life advice. No matter how silly my question, she would always answer without making me feel as if I should have known the answer. She has been my role model because of her intellect and her kind heart.

I would like to thank the people in my lab, because you guys and girls are awesome and

made my days more manageable. I would like to thank my friends from LA, from SD, and from SF because you were always understanding when I needed to stay home and work, or I wanted to go out and have fun. A special thanks to Aanchal, Rommina, and Kevin. The three of you, apart from being my roommates, have been a huge support during my Ph.D. path. You have been there for me in the ups and downs, and I hope I have done the same for you. You have become part of my family.

I would also like to mention the Rick Ainsworth and everyone in CEED for your infinite support since my undergraduate studies. Angie Castillo before she knew me decided to give me a chance. The GradSWE family that gave me the means to reach out and encourage girls to explore their career options.

The information, data, or work presented herein was funded by the Office of Energy Efficiency and Renewable Energy (EERE), U.S. Department of Energy, under Award Number DE-EE0006536.

Vita

Gabriela Alejandra Bran attended Saddleback college, and transfer to the University of California, Los Angeles where she got her bachelor's degree in mechanical engineering in June 2011. She started graduate school at UCLA right after, and got her M.S. in June 2014 in mechanical engineering.

Publications

Journal Publications

- Bran-Anleu, G., Lavine, A. S., Wirz, R. E., Kavehpour, H. P. (2014). "Algorithm to optimize transient hot-wire thermal property measurement." Review of Scientific Instruments, 85(4), 045105.
- Bran-Anleu, G, Wirz, R., "Material Compatibility of alloys with thermal energy storage fluid at high temperature." Manuscript in preparation.
- Bran-Anleu, G., Kavehpour, H. P., Lavine, A. S. "System modeling of an Ammonia-Based Energy Recovery System for start-up time." Manuscript in preparation.

Conference Publications

- Bran-Anleu, G, Kavehpour, H. P., Lavine, A. S. "Transient Behavior of an Ammonia-Based Energy Recovery System" *Proceedings of the 10th International Conference on Energy Sustainability*, June 26-30, 2016, Charlotte, North Carolina, USA.
- Lavine, A.S., Lovegrove, K.M., Jordan, J., Bran Anleu, G., Chen, C., Aryafar, H., and Sepulveda, A., (October, 2015), Thermochemical Energy Storage with Ammonia: Aiming for the SunShot Cost Target, SolarPACES 2015, Cape Town, South Africa, October 13-16, 2015.
- Bran-Anleu, G., Lavine, A. S., Wirz, R. E., Lakeh, R. B., & Kavehpour, H. P. (2013, November). "An Algorithm to Determine the Optimized Data Range in Transient Hotwire Thermal Property Measurement." In ASME 2013 International Mechanical Engineering Congress and Exposition (pp. V08CT09A068-V08CT09A068). American Society of Mechanical Engineers.

Presentations

 Bran-Anleu, Gabriela, Pirouz Kavehpour, and Adrienne Lavine. "System Modeling for Ammonia Synthesis Energy Recovery System." 68th Annual Meeting of the APS Division of Fluid Dynamics in Boston, MA, 2015.

•	ran-Anleu, G., "Optimization of Transient Heat Exchanger Performance for Improved Energy fficiency," 67th Annual Meeting of the APS Division of Fluid Dynamics, San Francisco, CA, lovember 23-25, 2014.			

CHAPTER 1: Background on Transient Heat Exchangers

Motivation

Heat exchangers have been extensively studied due to their vast number of industrial applications. They are used in multiple systems for energy generation, energy conversion, or energy storage.[1, 2] Any type of power plant, such as solar, hydro, or nuclear, requires heat exchangers as part of their thermodynamic power generation system. Heat exchangers are also found in air conditioning systems of cars and buildings. Many of these systems (e.g. air conditioning and solar power plants) function under transient conditions, but the design of the heat exchangers is typically optimized assuming steady state conditions.

It has been extremely difficult to obtain a comprehensive analysis of the transient behavior of heat exchangers due to their complexity. The thermal designs are configured from state of the art technology, proprietary concepts, and experience in design, fabrication, startup, and troubleshooting of heat exchangers in critical service. This becomes a problem when each application requires a different mode of operation. The goal of this work is to investigate the transient behavior of a simple counter-flow heat exchanger in order to apply the knowledge gained to more complex heat exchangers in the solar power industry. Exploring the transient behavior will also help determine if the desired behavior can be achieved in a timely manner and what parameters should be adjusted to modify the time a system takes to reach steady state.

Complex Heat Exchanger for Solar Energy Storage

The transient behavior of a more complex heat exchanger with the application in Concentrating Solar Power (CSP) was investigated. CSP consists of a solar field, thermal energy

storage (TES), and power block subcomponents as shown in Figure 1. The heliostats concentrate the energy from the sun to the receiver located at the top of the tower. The receiver uses the solar energy to heat up a working fluid that can be either stored or used to heat up supercritical steam.[3] One of the main challenges of CSP systems is the elevated total cost of the systems. Heat exchangers play a vital role in assuring high efficiency and economic competitiveness for solar energy storage at high temperature.[4] Challenges that are encountered in the design of heat exchangers for solar power plants include the cyclic operation, rapid startup and shutdown, and the unconventional thermophysical properties of the heat transfer fluid.

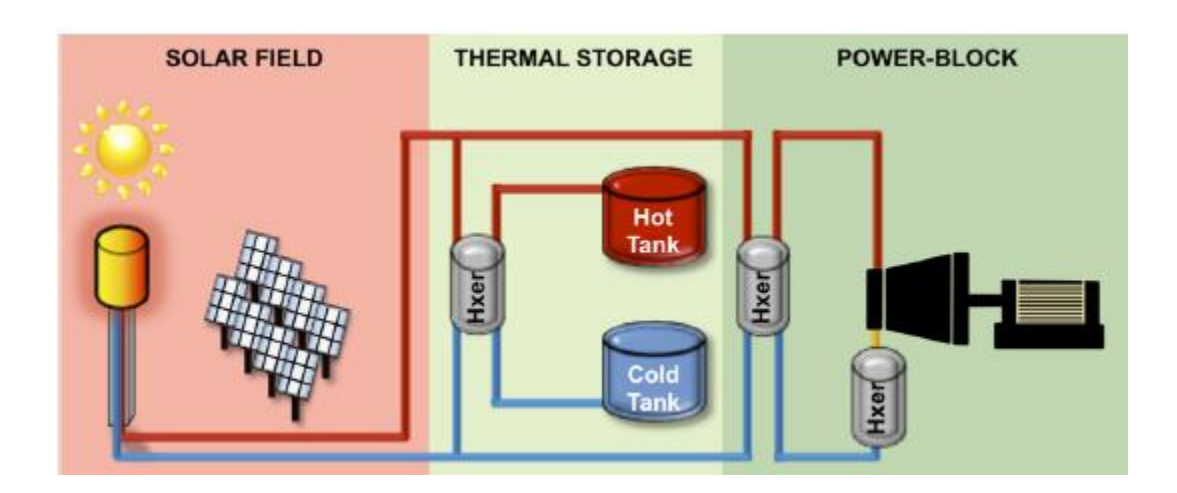


Figure 1 – Illustration of state-of-the-art molten salt CSP plant consisting of a solar field, TES, and power block subcomponents. [3]

The process control system that manages the flow rates of the overall system of a power plant unit can be improved if the transient response of the heat exchanger is well understood. The overall system performance can be improved if the transient response of the heat exchanger can be optimized for the desired applications. Also, thermal stresses might be affected by abrupt changes inside the heat exchanger. Understanding the effect that each parameter has on the heat exchanger transient response can help to predict and avoid material thermal damage.

Literature Review

A comprehensive study to fully understand the transient response of heat exchangers is necessary due to the complexity of the problem. The following assumptions have generally been made in the past to derive the governing differential equations for a counter-flow heat exchanger [5]:

- 1. The temperature of both fluids and the temperature of the wall are functions of time and axial position (one dimensional transient problem).
- 2. Heat transfer between the exchanger and the surroundings is negligible.
- 3. No heat is generated.
- 4. The mass flow rates of both streams do not vary with time.
- 5. The temperature of each fluid at the inlet is constant with time except for the imposed initial change.
- 6. The convective heat transfer coefficient on each side, and the thermal properties of both fluids and the wall, are constant.
- 7. Axial conduction is negligible.
- 8. The heat transfer surface area on each fluid side is not changing in the axial direction.
- 9. Fouling resistances are negligible.
- 10. The thermal capacitance of the heat exchanger enclosure is considered negligible relative to that of the heat transfer surface.

Applying these assumptions, a control volume analysis can be performed on a counterflow heat exchanger as shown in Figure 2. The system consists of two fluids, one cold and one hot, which are separated by a wall. Equation 1, Equation 3, and Equation 2 are the resulting one dimensional partial differential energy equations. Equation 1 and Equation 2 describe the thermal behavior of the hot fluid and the cold fluid. The first term of both equations represents the energy stored in the fluid which accounts for the system transients. The second term in the equations represents the advection term, and the last term represents the heat transfer between the wall and the fluid. Equation 3 represents the energy equation for the wall. The first term of the equation represents the energy stored in the wall, while the second and third terms represent the heat transfer from the hot fluid to the wall and the wall to the cold fluid.

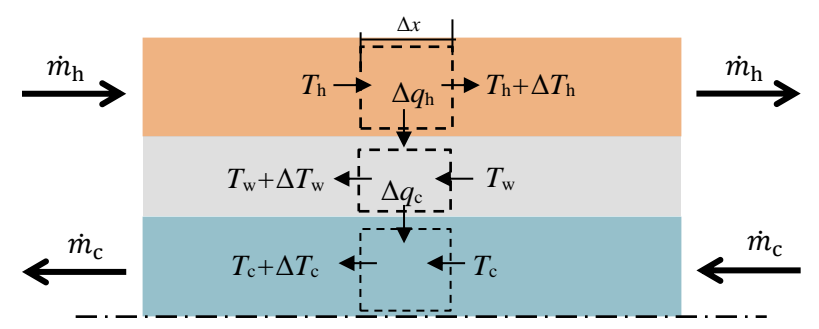


Figure 2 – Control volume analysis on a counter-flow heat exchanger which consists of the hot fluid (orange), the wall (gray), and the cold fluid (blue).

$$\left(\rho c_{\rm p} A_{\rm c}\right)_{\rm h} \left(\frac{\partial T_{\rm h}}{\partial t} + u_{\rm h} \frac{\partial T_{\rm h}}{\partial x}\right) + \left(\eta_{\rm o} h P\right)_{\rm h} \left(T_{\rm h} - T_{\rm w}\right) = 0$$
 Equation 1

$$\left(\rho c_{\rm p} A_{\rm c}\right)_{\rm c} \left(\frac{\partial T_{\rm c}}{\partial t} - u_{\rm c} \frac{\partial T_{\rm c}}{\partial x}\right) + \left(\eta_{\rm o} h P\right)_{\rm c} \left(T_{\rm c} - T_{\rm w}\right) = 0$$
 Equation 2

$$\left(\rho c_{\rm p} A_{\rm c}\right)_{\rm w} \frac{\partial T_{\rm w}}{\partial t} - \left(\eta_{\rm o} h P\right)_{\rm h} \left(T_{\rm h} - T_{\rm w}\right) - \left(\eta_{\rm o} h P\right)_{\rm c} \left(T_{\rm c} - T_{\rm w}\right) = 0$$
Equation 3

Cima and London [5] derived dimensionless parameters that until this day are widely used. The dimensionless parameters are defined in Table 4.

Table 1 – Dimensionless parameters proposed by Cima and London [5]

Table 1 Difficulties parameters proposed by emit and London [5	J
$X^* = \frac{x}{L}$ = dimensionless flow length variable	Equation 4
$t^* = \frac{t}{t_{ m d,min}}, t_{ m d} = \frac{t_{ m d,min}}{t_{ m d,max}}$	Equation 5
$C^* = \frac{C_{\min}}{C_{\max}} = \frac{\left(\dot{m}c_{\rm p}\right)_{\min}}{\left(\dot{m}c_{\rm p}\right)_{\max}} = \text{capacity ratio}$	Equation 6
$\overline{C}_{\mathrm{w}}^{*} = \frac{\overline{C}_{\mathrm{w}}}{\overline{C}_{\mathrm{min}}} = \text{wall capacity ratio}$	Equation 7
$NTU = \frac{UA}{C_{\min}}$ = number of transfer units	Equation 8
$R^* = \frac{(\eta_0 hA) \text{ on the } C_{\text{max}}}{(\eta_0 hA) \text{ on the } C_{\text{min}}} = \text{thermal resistance ratio}$	Equation 9

$$T^* = f(X^*, NTU, C^*, t^*, R^*, \overline{C}_{w}^*, t_{d}^*)$$

If Equation 1, Equation 3, and Equation 2 are rearranged, a dimensionless system of partial differential equations is obtained, with the parameters given in Table 1. Due to the complexity of the heat exchanger problem, analytical solutions have been calculated for simplified problems or very specific cases. London et al. [6, 7] presented an analytical solution for two limiting cases where $R^* = \infty$ and $R^* = 0$ for $C^* = 0$. In these limiting cases, the thermal resistance of one of the fluids is much smaller than the other fluid, and the "minimum" flow has a heat capacity ratio equal to zero, $(\dot{m}c_p)_{\min} = 0$. Rizika [8] obtained an analytical solution for all values of R^* , but for $C^* = 0$ and $0 \le t^* \le 1$. The temperature of the C_{\max} fluid can be approximated to be constant everywhere, which simplifies the problem. Cima and London [5] also found an analytical solution for problems

with $C^* = 1$ and $R^* = 1$. This solution is limited to fluids that have the same heat capacity ratio. Yin and Jensen [9] approximated the transient response of a counter flow heat exchanger by using an integral method. The authors simplified the problem by assuming that one of the fluids remains at a constant temperature. Gvozdenac [10, 11] obtained an analytical solution for the transient response of a counter flow heat exchanger by using the Laplace transform method. The collocation method is then used for solving the resulting integral equation. The author's solution assumes that the inlet temperature of one of the fluids is perturbed. Gvozdenac introduced slightly different dimensional distance, time, and temperature than those of Cima and London:

$$x = \frac{X}{L}NTU, z = \frac{t}{t^*}$$
 Equation 10
$$\theta_i(X,t) = \frac{T_i(X,t) - T}{\Delta T}, (i = 1,2,w)$$
 Equation 11
$$X^* = \frac{x}{L} = \text{dimensionless flow length variable}$$
 Equation 12
$$t^* = \frac{t}{t_{\text{d min}}}, \quad t_{\text{d}} = \frac{t_{\text{d,min}}}{t_{\text{d max}}}$$
 Equation 13

where T is the reference temperature and ΔT is a characteristic temperature difference. By applying the relations given, Gvozdenac comes up with the following dimensionless parameters:

$$NTU = \frac{(hA)_1 (hA)_2}{(hA)_1 + (hA)_2} \frac{1}{W_1}$$
 Equation 14

$$t^* = \frac{c_{\rm w} M_{\rm w}}{(hA)_1 + (hA)_2}$$
 Equation 15

$$K_1 = \frac{(hA)_1}{(hA)_1 + (hA)_2}, K_2 = 1 - K_1$$
 Equation 16

$$C_i = L \frac{W_i}{c_w M_w} \frac{1}{K_i U_i} (i = 1, 2)$$
 Equation 17

The accuracy of Gvozdenac's results depends on the number of collocation points, and it is very difficult to estimate the collocation numbers needed for the desired accuracy. Gvozdenac's solution is valid for a step change in the inlet temperature of only one of the fluids. Shah [12] and Bunce [13] present a summary of the analytical solutions found in the literature.

Even computational models in the literature that take into consideration the transient behavior of a heat exchanger have numerous restrictions that limit the generality of the problem being studied. Kandlikar et al. [14] developed a model for a counter-flow heat exchanger using thermal networks as shown in Figure 3. The solution assumes a step temperature change on only one of the fluids. The authors implemented the model using the commercial software called THERMONET-TransHX. Kandlikar generated tables with the efficiency of a counter-flow heat exchanger for specific nondimensional parameters. If any of the assumptions needs to be relaxed, then the thermal network analysis needs to be repeated and implemented using THERMONET-TransHX.

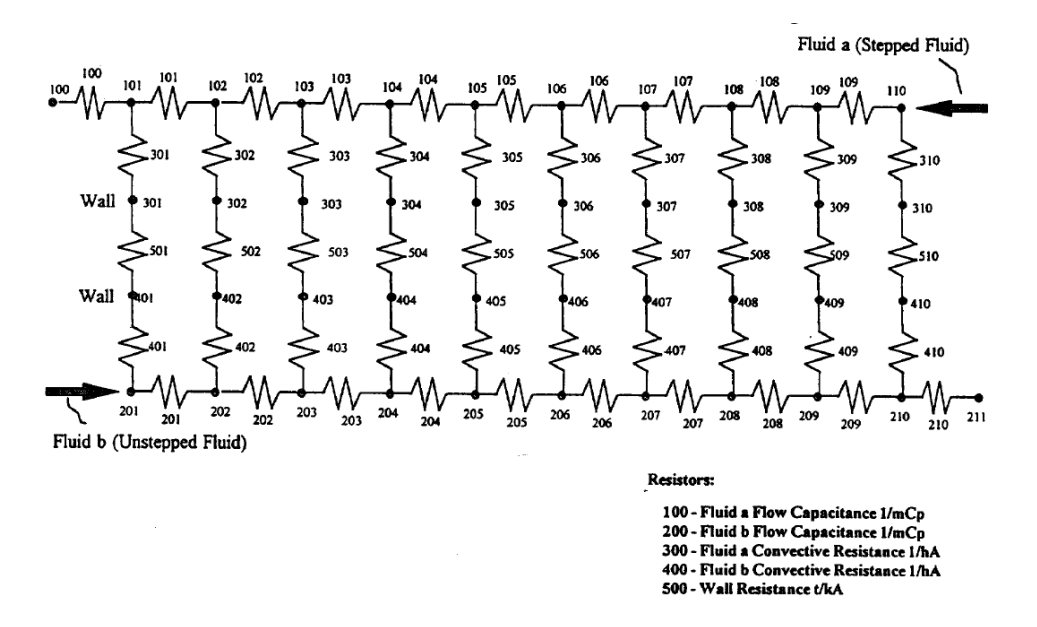


Figure 3 – Equivalent thermal network of a counter flow heat exchanger [14].

Abbasi et al. [15] developed a numerical model to solve for the transient response of a concentric parallel flow and counter flow heat exchangers. The effect of a step change and a sinusoidal time change in the inlet temperature in one of the streams was investigated. The results given were specific for water only, and only two different boundary conditions were explored. For more general results, a new study is needed.

Table 2 shows a summary of all the solution found by different authors for $C^*=0$, which means that one of the fluids is stationary or that $C_{\min} \ll C_{\max}$. This simplifies the problem by neglecting the advection term in one of energy equations on the fluids. These solutions are valid for either a parallel-flow or counter-flow heat exchanger. As shown in Table 2, there are other restrictions for the solutions found by the authors (second column). The solutions found were solved either analytically or by using the electromechanical analogy.

Table 2 – Solution for transient heat exchangers for $C^* = 0$.

$C^* = 0$	Restrictions	Solution Method	Reference
	• $R^* = \infty$ or $\overline{C_w}^* = 0$ • $R^* = 0$ or $\overline{C_w}^* = 0$	Analytical	London et al. (1956)
Cton shance	• $0 \le t^* \le 1$, $\overline{C_w}^* \le 1$	Analytical	Rizika (1956)
Step change in C_{max} fluid	• $R^* = 1$ and $\overline{C_w}^* > 5$ • $R^* = 1$ and $NTU = 3$ • $NTU = 3$ and $\overline{C_w}^* = 20$	Electromechanical analog	London et al. (1956)
	• $\overline{C_w}^* > 100$	Analytical	Myers et al. (1970)
Step change in C_{min} fluid	• $R^* = 1$ and $\overline{C_w}^* > 20$ • $R^* = 1$ and $NTU = 1$ • $NTU = 1$ and $\overline{C_w}^* \ge 20$	Electromechanical analog	London et al. (1959)
	• t*>1	Analytical	Myers et al. (1970)
Step change in C_{max} fluid or in \dot{m}_{min}	• t* > 1	Analytical	Yin and Jensen (2003)

Table 3 shows a summary of all the solutions found by different authors for counter flow heat exchangers. This simplifies the problem by neglecting the advection term in one of the energy equations of the fluids. As shown in Table 2, there are other restrictions for the solutions found by the authors (first column). The methods used to solve for the transient solution were analytical, electromechanical analogy, finite element, or thermal network.

Table 3 – Solutions for counter flow heat exchangers

Restrictions	Solution Method	Reference
• $R^* = 1$ or $C^* = 1$ $10 < \overline{C_w}^* < 40$ $6 \le NTU \le 8$	Electromechanical analog	Cima and London (1958)
• $R^* = 1$ and $\overline{C_w}^* > 20$ • $R^* = 1$ and $NTU = 1$ • $NTU = 1$ and $\overline{C_w}^* \ge 20$	Electromechanical analog	London et al. (1959)
• $C^* = 1, \overline{C_w}^* > 100, \ 1.5 \le NTU \le 8$ • $C^* = 1, \overline{C_w}^* > 100, \ 1.5 \le NTU \le 6$ $0.25 \le R^* \le 4$ Note: Solution for T_I	Electromechanical analog	London et al. (1964)
• t* > 1	Analytical	Myers et al. (1970)
• Gas to gas, limited range of C_w^* , inaccurate early times	Finite Difference	Romie (1984)
Gas to gas	Analytical	Gvozdenac (1987)
Step change in one fluidcommercial software	Thermal network	Kandlikar (1995)
Step change in one fluidSinusoidal inlet in one fluid	Finite Difference	Abbasi et al. (2013)

After reviewing the literature, it was concluded that a more rigorous numerical model needed to be developed. In the current research, an in-house computational model was developed and exercised to fully understand the physics of the transient behavior of a heat exchanger. The results obtained by Gvozdenac were used to verify the numerical model. The model was used to determine the parameters and conditions that dominate the transients in a heat exchanger. Also, it was important to understand how a transient solution differs from the steady state solution. The sensitivity of the outlet stream temperature to a sudden change to the working fluid inlet conditions such as temperature and mass flow rate were investigated. This information will be used to design thermal systems, guide efforts to reduce sources of inefficiency in existing systems, and evaluate system economics. The numerical model solves a non-dimensional system of differential equations

that describe the behavior of a counter-flow heat exchanger.

In chapter 2, the numerical model will be explained in detailed. In Chapter 3, a scaling analysis was performed to determine what influences the time a heat exchanger takes to reach steady state. In addition, a parametric study was then performed to determine the effect the dimensionless parameters have on the time the system takes to reach steady state. In chapter 4, a more complex heat exchanger with a specific application was investigated. It was of special interest to look at a heat exchanger with varying properties, heat generation, varying heat transfer coefficient, and axial conduction.

CHAPTER 2: Numerical Model

A numerical model was developed to fully understand the parameters that will predominate in a transient heat exchanger problem. The numerical model is meant to solve three coupled partial differential energy equations – one equation for the hot fluid, one equation for the cold fluid, and one equation for the wall separating both fluids. The bulk temperatures of both fluids and the wall are calculated as a function of time and space (*x*-direction). In contrast with the solutions presented by other authors, the numerical model relaxes the restrictions mentioned in Table 1 and Table 2. It can be used to solve problems with a wide range of dimensionless parameters, as well as different types of boundary and initial conditions. The transient model is also able to get the time the system takes to reach steady state.

Numerical Model

Assumptions

The model makes the following assumptions:

- 1. Temperature averaged over the cross-section (in the storage term) is the same as the bulk temperature (velocity-weighted average in the advection term).
- 2. Thermal capacitance of the heat exchanger outer wall is negligible.

Differential Equations

The following differential equations for the counter-flow heat exchanger shown in Figure 4 were obtained:

$$\left(\rho c_{\rm p} A_{\rm c}\right)_{\rm h} \left(\frac{\partial T_{\rm h}}{\partial t} + u_{\rm h} \frac{\partial T_{\rm h}}{\partial x}\right) - \left(k A_{\rm c}\right)_{\rm h} \frac{\partial^2 T_{\rm h}}{\partial x^2} + \left(h P\right)_{\rm h} \left(T_{\rm h} - T_{\rm w}\right) = 0$$
 Equation 18

$$\left(\rho c_{\rm p} A_{\rm c}\right)_{\rm c} \left(\frac{\partial T_{\rm c}}{\partial t} - u_{\rm c} \frac{\partial T_{\rm c}}{\partial x}\right) - \left(k A_{\rm c}\right)_{\rm c} \frac{\partial^2 T_{\rm c}}{\partial x^2} + \left(h P\right)_{\rm c} \left(T_{\rm c} - T_{\rm w}\right) = 0$$
 Equation 19

$$\left(\rho c_{\rm p} A_{\rm c}\right)_{\rm w} \frac{\partial T_{\rm w}}{\partial t} - (kA)_{\rm w} \frac{\partial^2 T_{\rm w}}{\partial x^2} - (hP)_{\rm h} \left(T_{\rm h} - T_{\rm w}\right) - (hP)_{\rm c} \left(T_{\rm c} - T_{\rm w}\right) = 0$$
 Equation 20

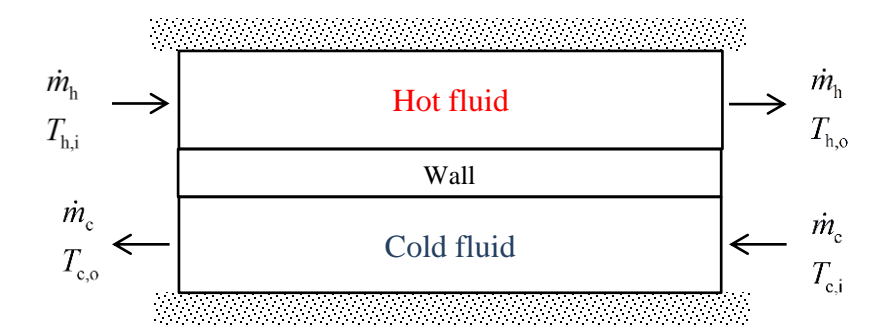


Figure 4 – Counter flow heat exchanger with hot fluid entering through one end and cold fluid entering through the opposite end. The fluids are separated by a wall, and the outer wall of the heat exchanger is insulated.

Equation 18, Equation 19, and Equation 20 are the one dimensional partial differential energy equations. These equations are identical to Equation 1, Equation 2, and Equation 3, except for the extra term representing axial conduction. The following dimensionless distance, time, and temperature were used to rewrite Equation 18, Equation 19, and Equation 20 in non-dimensional form in an attempt to recover the characteristic properties of the system:

$$x^* = \frac{x}{L}, \quad t^* = \frac{t}{t_{\text{r,h}}}, \quad \rightarrow t_{\text{r,h}} = \frac{L}{u_{\text{h}}}$$
 Equation 21

$$\theta_{k} = \frac{T_{k} - T_{c,o}}{T_{h,i} - T_{c,o}}, \quad k = h, c, w$$
Equation 22

where $t_{r,h}$ is the residence time of the hot fluid.

The non-dimensional forms of the differential equations result in the following:

$$\frac{\partial \theta_{h}}{\partial t^{*}} + \frac{\partial \theta_{h}}{\partial x^{*}} - \frac{1}{Pe_{h}} \frac{\partial^{2} \theta_{h}}{\partial x^{*2}} + NTU_{h} (\theta_{h} - \theta_{w}) = 0$$
Equation 23
$$C \frac{\partial \theta_{c}}{\partial t^{*}} - M \frac{\partial \theta_{c}}{\partial x^{*}} - \frac{C\beta}{Pe_{h}} \frac{\partial^{2} \theta_{c}}{\partial x^{*2}} + NTU_{c} (\theta_{c} - \theta_{w}) = 0$$
Equation 24

$$C_{w} \frac{\partial \theta_{w}}{\partial t} - \frac{C_{w} \beta_{w}}{P e_{h}} \frac{\partial^{2} \theta_{w}}{\partial x^{*2}} + NTU_{h} \left(\theta_{w} - \theta_{h}\right) + NTU_{c} \left(\theta_{w} - \theta_{c}\right) = 0$$
 Equation 25

Each dimensionless parameter is defined in Table 4. The fluids and wall temperatures are a function of the dimensionless parameters presented in Table 4:

$$\theta_k = f(x^*, t^*, C, C_w, M, NTU_h, NTU_c, Pe_h, \beta, \beta_w)$$
 for $k = h, c, w$.

Table 4 – Dimensionless parameters for system of equations describing the behavior of a transient heat exchanger.

Dimensionless parameter	Representation	
$C = \frac{\left(\rho A_{c} c_{p}\right)_{c}}{\left(\rho A_{c} c_{p}\right)_{h}}, \qquad C_{w} = \frac{\left(\rho A_{c} c_{p}\right)_{w}}{\left(\rho A_{c} c_{p}\right)_{h}}$	Storage	Equation 26
$M = \frac{\left(\dot{m}c_{\rm p}\right)_{\rm c}}{\left(\dot{m}c_{\rm p}\right)_{\rm h}}$	Advection	Equation 27
$NTU_{h} = \frac{\left(hA_{s}\right)_{h}}{\left(\dot{m}c_{p}\right)_{h}} = \frac{\left(hP\right)_{h}L}{\left(\rho c_{p}uA_{c}\right)_{h}}, \qquad NTU_{c} = \frac{\left(hP\right)_{c}L}{\left(\rho c_{p}uA_{c}\right)_{h}}$	Heat exchange	Equation 28
$Pe_{\rm h} = \frac{Lu_{\rm h}}{\alpha_{\rm h}}, \beta = \frac{\alpha_{\rm c}}{\alpha_{\rm h}}, \beta_{\rm w} = \frac{\alpha_{\rm w}}{\alpha_{\rm h}},$	Axial conduction	Equation 29

Four different categories were defined to describe the dimensionless parameters: storage, advection, heat exchange, and axial conduction terms. C and C_w represent the storage terms. C is the ratio of the cold fluid storage term and the hot fluid storage term, and C_w is the ratio of the wall

storage term and the hot fluid storage term. M represents the advection in the system; it is the ratio of the cold fluid advection term and the hot fluid advection term. NTU_h represents the heat transfer between the hot fluid and the wall; it is the ratio of the heat transfer to the wall and the advection heat transfer in the hot fluid. NTU_c represents the heat transfer between the cold fluid and the wall; it is the ratio of the heat transfer between the cold fluid and the advection heat transfer in the hot fluid. NTU_h and NTU_c are not based on the minimum fluid but always on the hot fluid.

Boundary and Initial Conditions

The boundary conditions for the energy equations of the hot and cold fluids are specified by Equation 30 and Equation 31. These boundary conditions can either be constant or they can vary with time. The wall is set to have no heat flux at x = 0 and x = L as described in Equation 32.

$$\theta_{h}(x^{*}=0,t^{*}) = \theta_{h,i}(t^{*})$$
 Equation 30
$$\theta_{c}(x^{*}=1,t^{*}) = \theta_{c,i}(t^{*})$$
 Equation 31
$$\frac{\partial \theta_{w}}{\partial x^{*}}\Big|_{x^{*}=0} = \frac{\partial \theta_{w}}{\partial x^{*}}\Big|_{x^{*}=1} = 0$$
 Equation 32
$$\frac{\partial^{2} \theta_{w}}{\partial x^{*2}}\Big|_{x^{*}=0} = \frac{\partial^{2} \theta_{w}}{\partial x^{*2}}\Big|_{x^{*}=1} = 0$$
 Equation 33

The initial temperature of both fluids and the wall also need to be specified (Equation 34-Equation 36). The initial temperatures can be constant or they can vary with location.

$$\theta_{h}(x^{*}, t^{*} = 0) = \theta_{h,0}(x^{*})$$
 Equation 34
$$\theta_{c}(x^{*}, t^{*} = 0) = \theta_{c,0}(x^{*})$$
 Equation 35
$$\theta_{w}(x^{*}, t^{*} = 0) = \theta_{w,0}(x^{*})$$
 Equation 36

Numerical Method

An algorithm was developed to obtain the numerical solution of the system of partial differential equations (PDE) described in Equation 23-Equation 25. The equations were discretized in the *x*-direction and in time. In this section, *i* will be used as the position index, and *n* will be used as the time index as shown in Figure 5. For example, the function $\theta(x, t)$ is discretized as $\theta(x_i, t_n)$. From this point on, the non-dimensional temperatures will be written as:

$$\theta(x_i, t_n) =: \theta_i^n$$

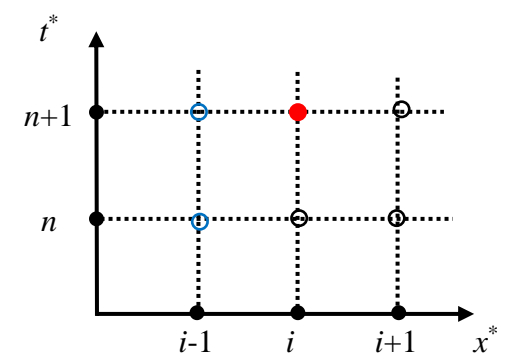


Figure 5 – Graphical representation of the grid. Solution will be obtained at different grid points along the reactor length (x-axis) and at different points in time (y-axis).

The Crank-Nicolson method was used for the discretization in time of Equation 23, Equation 24, and Equation 25. The advection term was discretized using the first-order upwind scheme. The conduction term was discretized using the center difference scheme. To illustrate this, one can look at Figure 5. The discretization of the advection term uses the information at position i-1 (upwind scheme) at time n and n+1 (Crank-Nicolson method) to find the value at i. The discretization of the conduction term uses the information at position i-1 and i+1 (center difference scheme) at time n and n+1 (Crank-Nicolson method) to find the value at i at time n+1. Equation 37-Equation 39 show the discretized equations.

$$\frac{\theta_{h,i}^{n+1} - \theta_{h,i}^{n}}{\Delta t^{*}} + \frac{\theta_{h,i}^{n} - \theta_{h,i-1}^{n}}{2\Delta x^{*}} + \frac{\theta_{h,i-1}^{n+1} - \theta_{h,i-1}^{n+1}}{2\Delta x^{*}} - \dots
\dots - \frac{1}{Pe_{h}} \frac{\theta_{h,i+1}^{n+1} - 2\theta_{h,i}^{n+1} + \theta_{h,i-1}^{n+1}}{2\Delta x^{*2}} - \frac{1}{Pe_{h}} \frac{\theta_{h,i+1}^{n} - 2\theta_{h,i}^{n} + \theta_{h,i+1}^{n}}{2\Delta x^{*2}} + \dots
\dots + \frac{NTU_{h}}{2} \left(\theta_{h,i}^{n} - \theta_{w,i}^{n}\right) + \frac{NTU_{h}}{2} \left(\theta_{h,i}^{n+1} - \theta_{w,i}^{n+1}\right) = 0$$
Equation 37

$$M \frac{\theta_{c,i}^{n+1} - \theta_{c,i}^{n}}{\Delta t^{*}} + \frac{C}{2} \frac{\theta_{c,i}^{n} - \theta_{c,i-1}^{n}}{\Delta x^{*}} + \frac{C}{2} \frac{\theta_{c,i}^{n+1} - \theta_{c,i-1}^{n+1}}{\Delta x^{*}} - \dots$$

$$\dots - \frac{1}{2Pe_{c}} \frac{\theta_{c,i+1}^{n+1} - 2\theta_{c,i}^{n+1} + \theta_{c,i-1}^{n+1}}{\Delta x^{*2}} - \frac{1}{2Pe_{c}} \frac{\theta_{c,i+1}^{n} - \theta_{c,i}^{n} + \theta_{c,i-1}^{n}}{\Delta x^{*2}} + \dots$$

$$\dots + \frac{NTU_{c}}{2} \left(\theta_{c,i}^{n} - \theta_{w,i}^{n}\right) + \frac{NTU_{c}}{2} \left(\theta_{c,i}^{n+1} - \theta_{w,i}^{n+1}\right) = 0$$
Equation 38

$$\frac{\theta_{\mathbf{w},i}^{n+1} - \theta_{\mathbf{w},i}^{n}}{\Delta t^{*}} - \frac{1}{2Pe_{\mathbf{w}}} \frac{\theta_{\mathbf{w},i+1}^{n+1} - 2\theta_{\mathbf{w}i}^{n+1} + \theta_{\mathbf{w},i-1}^{n+1}}{\Delta x^{*2}} - \frac{1}{2Pe_{\mathbf{c}}} \frac{\theta_{\mathbf{w},i+1}^{n} - 2\theta_{\mathbf{w},i}^{n} + \theta_{\mathbf{w},i-1}^{n}}{\Delta x^{*2}} + \dots$$

$$\dots + \frac{NTU_{\mathbf{c}}}{2} \left(\theta_{\mathbf{w},i}^{n} - \theta_{\mathbf{c},i}^{n}\right) + \frac{NTU_{\mathbf{c}}}{2} \left(\theta_{\mathbf{w},i}^{n+1} - \theta_{\mathbf{c},i}^{n+1}\right) + \dots$$

$$\dots + \frac{NTU_{\mathbf{h}}}{2} \left(\theta_{\mathbf{w},i}^{n} - \theta_{\mathbf{h},i}^{n}\right) + \frac{NTU_{\mathbf{h}}}{2} \left(\theta_{\mathbf{w},i}^{n+1} - \theta_{\mathbf{h},i}^{n+1}\right) = 0$$
Equation 39

The n+1 terms in Equation 37-Equation 39 were grouped on the left hand side of the equation, and the n terms were moved to the right to get the following equation:

$$A\theta^{n+1} = b$$
 Equation 40

A is a pentagonal matrix composed of dimensionless parameters in Table 4. The size of A is determined by the size of the grid in the x-direction. If v is the number of grids in the x-direction, then the size of A is $3v-2\times3v-2$. The vector b is composed of a combination of known temperatures at time n, boundary conditions at time n and n+1, and dimensionless parameters in Table 4. The

algorithm finds the dimensionless solution θ^{n+1} by marching in time. Equation 40 is solved to get the temperature of both fluids and the wall as a function of position at each time step. The vector θ^{n+1} is defined as follows:

$$egin{aligned} eta_{\mathrm{h,2}} & eta_{\mathrm{h,3}} & dots & eta_{\mathrm{h,v}} & eta_{\mathrm{h,v}} & eta_{\mathrm{w,1}} & eta_{\mathrm{w,2}} & dots & eta_{\mathrm{c,1}} & eta_{\mathrm{c,2}} & dots & eta_{\mathrm{c,v-1}} & eta_{\mathrm{c,v-1}} & dots & dots & eta_{\mathrm{c,v-1}} & dots & do$$

It is composed of the dimensionless bulk temperatures of both fluids and the wall along the reactor for a specific time step.

Stability

The stability of the algorithm is ensured by restricting the Courant (*Co*) number of both fluids to be less than 0.1. A Courant number (*Co*) is defined for the hot fluid and the cold fluid in Equation 41 and Equation 42, respectively. The following relationship is used to ensure convergence:

$$Co_{\rm h} = \frac{\Delta t^*}{\Delta x^*} < 0.1$$
 Equation 41

$$Co_{\rm c} = \frac{M\Delta t^*}{C\Delta x^*} < 0.1$$
 Equation 42

where Δt^* and Δx^* are the time step and position step, respectively. [16-19]

A fixed number of data points for the *x*-position is chosen. Note: this is highly dependent on the computational capabilities. If *A* is extremely large, solving for θ^{n+1} in Equation 40 for each time step will significantly slow down the algorithm. Therefore, Δx^* needs to be fine, but cannot be extremely small. For this work, the size of *A* (3*v*-2×3*v*-2) is limited to be less than 5000×5000. Once Δx^* is determined, then Δt^* is calculated by solving Equation 41 and Equation 42, and choosing the minimum Δt^* to ensure stability of both equations containing the advection term.

As mentioned before, the transient model is able to get the steady state solution and the time the system takes to reach steady state. This is done by evaluating the dimensionless temperature change between temperatures at time n and n+1 at each location. A condition was established that determines when the system can be considered to be at steady state. For this work, the condition was the following:

$$Abs(\theta_i^{n+1} - \theta_i^n) < \eta$$

The value of η will be given later for each specific case.

Verification of the numerical model

Three different methods were used to verify the transient one dimensional counter-flow heat exchanger numerical model. An energy balance was calculated at each time step to ensure that energy is conserved. Then, the steady state solution of the numerical model was compared to the solution of the steady state problem using the Effectiveness – *NTU* Method [20]. Finally, the transient solution of the algorithm was compared to the analytical results obtained by Gvozdenac [10]. For the verification of the algorithm, dimensional values were used for comparison purposes. *Problem Statement for Verification*

A coaxial pipe with a counter flow, as shown in Figure 6, was used for the verification. Both of the streams were set to an initial temperature $T_{\rm h,0} = T_{\rm c,0} = 30$ °C. The inlet temperature

increases to $T_{h|x=0, t>0} = T_{h,i} = 100$ °C at $t^*>0$. The heat capacitance of the wall was assumed to be much smaller than the capacitance of both of the fluids, and the heat conduction in the axial direction was assumed to be negligible.

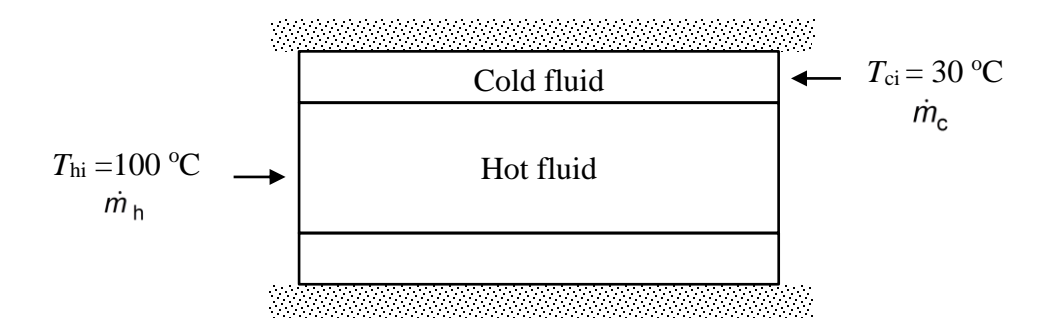


Figure 6 – Geometry of the problem, domain of computations, and boundary conditions.

First Verification Method: Energy Balance

An energy balance was performed to ensure that the energy equation is satisfied. The storage term, advection term, and the heat transfer term in Equation 18, Equation 19, and Equation 20 (except for the conduction term, which was set to zero for this simulation) were calculated independently at each point using the numerical model temperature data and fluid conditions. The terms were added, and as expected the terms add up to zero, as shown in Figure 7, ensuring that energy is being conserved in the numerical model. Figure 7 also shows the importance of each of the terms in Equation 18, Equation 19, and Equation 20. For this specific case, the wall capacity is negligible compared to the rest of the terms. The storage term for one of the fluids (in this case the hot fluid) is significant at early times. This is mainly due to the step change imposed at the inlet of this fluid at t > 0. At later times, the transient effect decreases while the advection term of the cold fluid increases. Also, the time it takes for the system to reach steady state can be determined from Figure 7. Once the system reaches steady state, the magnitude of the different

energy terms won't change with time anymore. It can be assumed that the system has reached steady state at approximately 600 seconds.

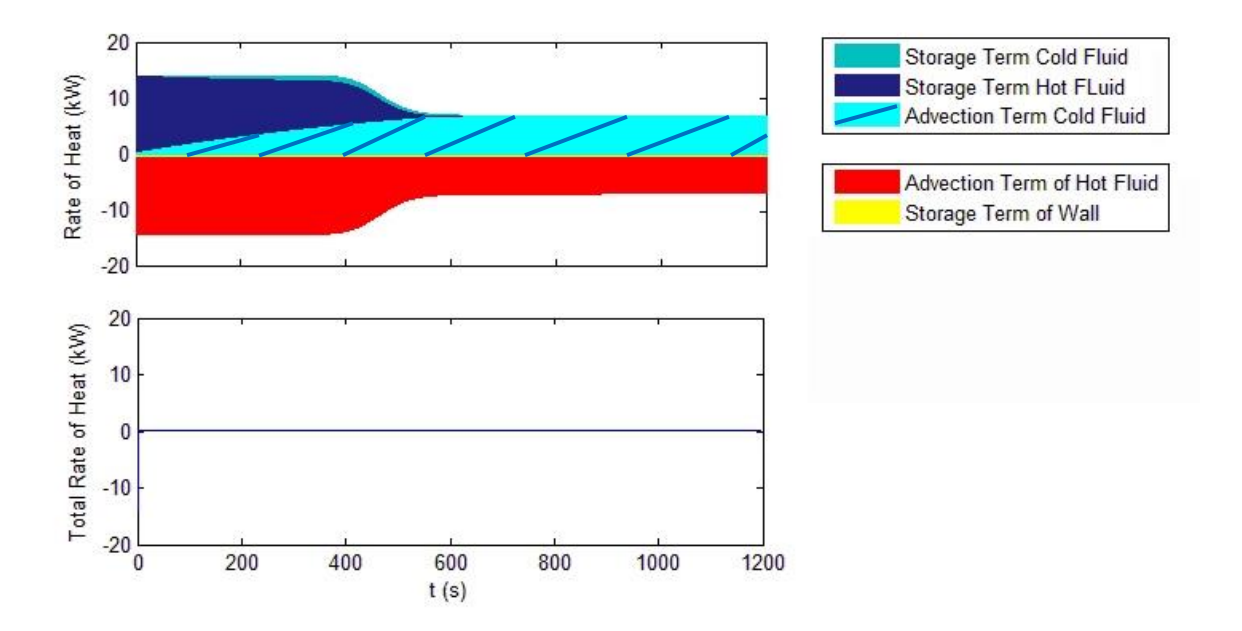


Figure 7 – Energy balance for a transient one dimensional counter-flow heat exchanger model to ensure energy conservation. Top graph: rate of heat as a function of time. Bottom graph: total rate of heat as a function of time is always zero.

Second Verification Method: Steady State Solution

The numerical model steady state results were compared with the analytical solution of a steady state counter-flow heat exchanger solution [21]. The steady state solution was calculated using the Effectiveness-NTU method. The hot outlet temperature is $T_h = 73$ °C at x = L, and the cold outlet temperature is $T_c = 42$ °C at x = 0. The steady state outlet temperatures obtained from the numerical model match the solution obtained using the Effectiveness-NTU method as shown in Figure 8.

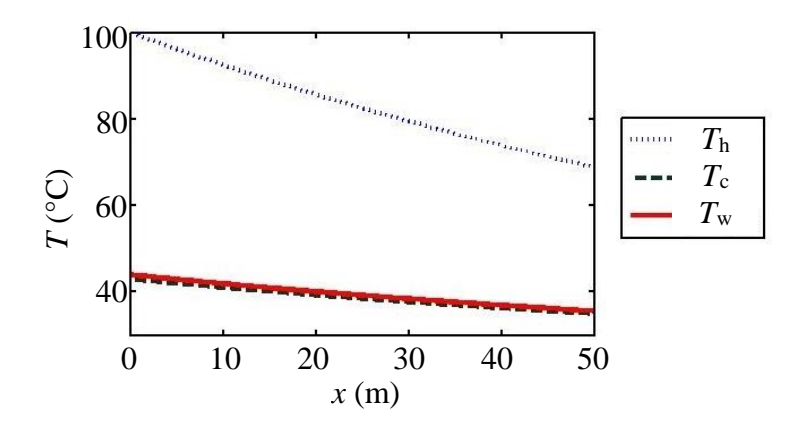


Figure 8 – Steady state solution for numerical model.

Third Verification Method: Transient solution (Gvozdenac)

The last method to verify the numerical model was to compare the numerical results with the analytical results obtained by Gvozdenac [10]. The author presents the spatial temperature distributions for both fluids and the wall for various dimensionless time steps, z. Gvozdenac illustrates the temperature distribution for the following conditions: NTU = 1, $\omega = 0.5$, $K_1 = 0.25$, $C_1 = 1.5$, and $C_2 = 0.5$ for z = 1, 2, 3, and 4 (see Equation 14 - Equation 17 for dimensionless number definitions).

Figure 9 shows the agreement between Gvozdenac results (black solid lines) and the results obtained from the numerical model developed here (dashed colored lines). The solutions for z = 2, z = 3, and z = 4 are in complete agreement. However, the solution at z = 1 deviates when the temperature of the hot fluid undergoes a step change. This is the result of the upwind scheme used for the advection term in the discretization of the differential equations, and if the grid is refined then our solution approaches Gvozdenac solution. For the work presented here, it was not of special interest to capture the sharp step, so the grid was not refined for future runs.

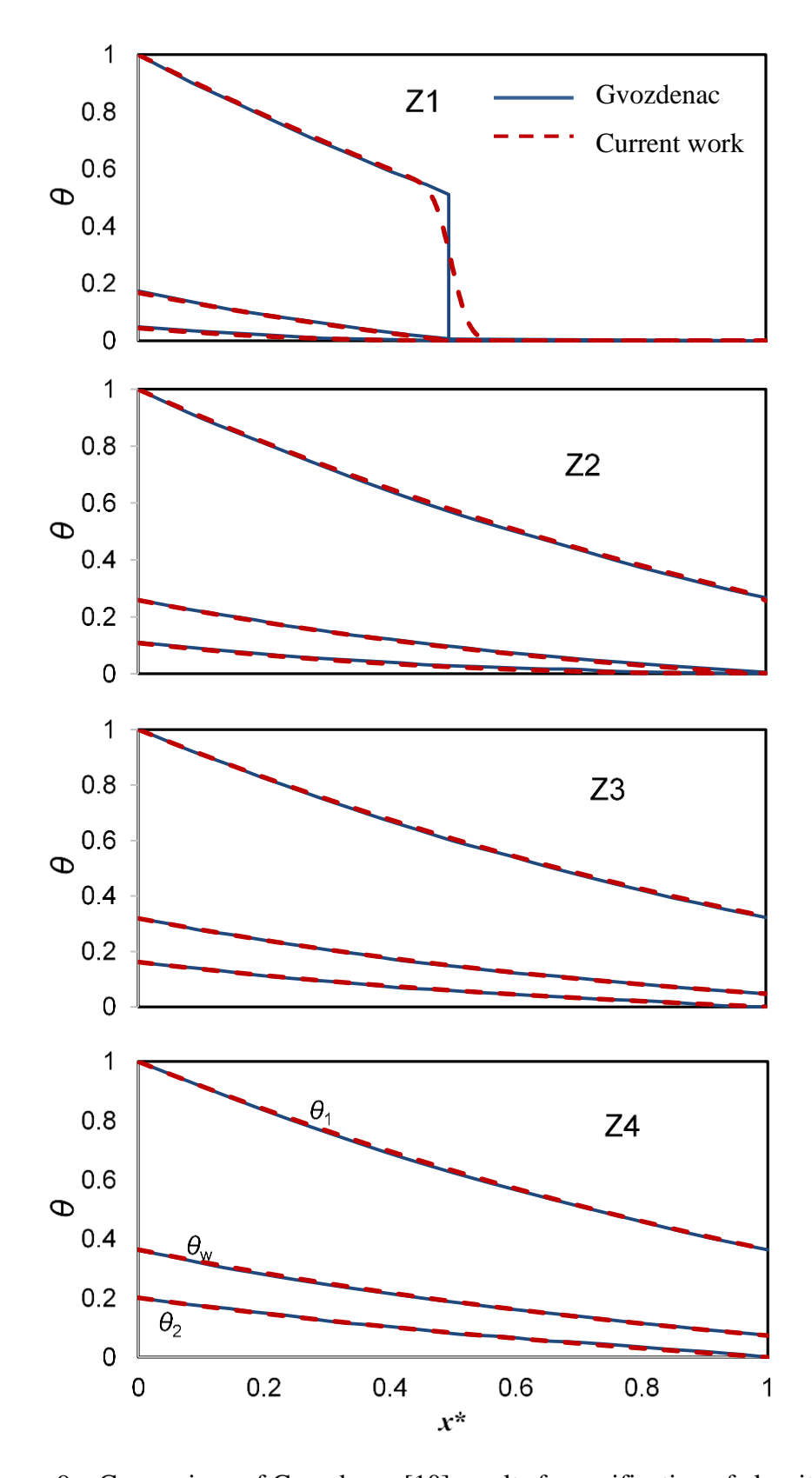


Figure 9 – Comparison of Gvozdenac [10] results for verification of algorithm.

The three different methods for verification show that the algorithm is conserving energy and getting accurate steady state outlet flow temperatures, and that the transient temperature distributions match those of a previous author.

CHAPTER 3: Numerical Experiments

Exploration of transient behavior of a simple counter-flow heat exchanger

In industry, steady state is usually assumed when analyzing a heat exchanger. For example, for a system with the following conditions: M = 1, C = 1, $C_w = 0.1$, $NTU_h = 1$, $NTU_c = 1$, one would assume that the heat exchanger behaves as shown in Figure 10. This figure shows the steady state temperature profiles of the hot (red) and cold (blue) streams as well as the wall (green). The linear profiles are a consequence of the choice of C = 1. At steady state, the hot outlet temperature is 0.66, and the cold outlet temperature is 0.33 resulting in a 33% effectiveness. With new technologies arising, it is important to understand what happens before the system has reached steady state, and how this behavior may affect the effectiveness of the system. It is also important to know how long the system takes to reach steady state.

Four different cases that cause different transient behavior in the system were investigated. Case one will be referred to as the start-up of the system. It consists of a system that is initially $(t^*=0)$ at the same temperature everywhere, and at $t^*=0^+$, a step change is imposed on one of the flows. Case two is when the system in case one has reached steady state, another *step change in the inlet temperature* is imposed. Case three is when the system in case one has reached steady state, another *step change in the mass flow rate* is imposed. Case four is when the system is initially at a uniform temperature, and a step change is imposed at the inlet of one of the flows, but the new inlet temperature oscillates with time. Axial conduction was neglected in all these cases since it is usually negligible under typical flow conditions.

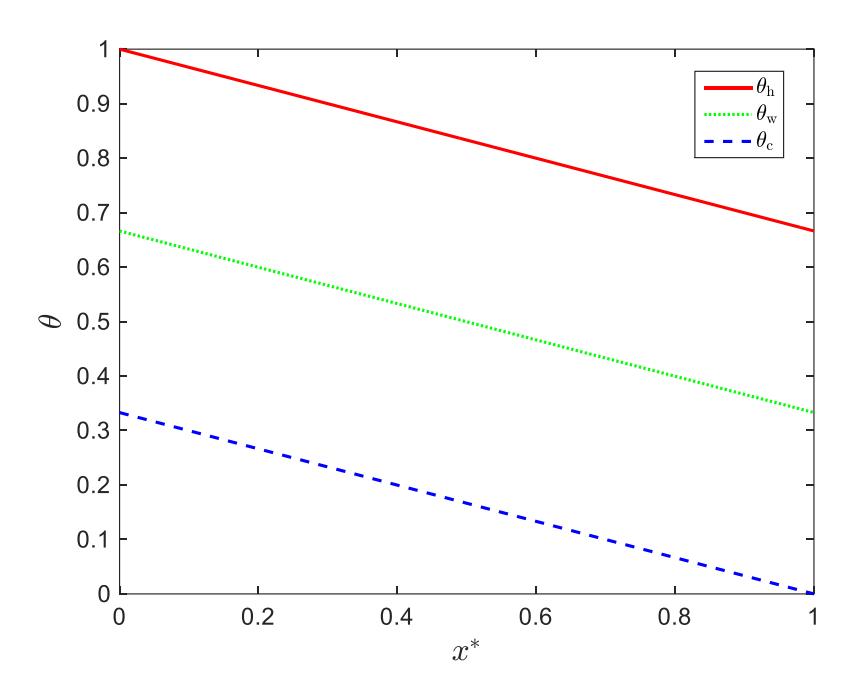


Figure 10 – Steady state temperature of hot fluid (red continuous line), cold fluid (blue dashed line), and the wall (green dotted line) for the following conditions: M = 1, C = 1, $C_w = 0.1$, $NTU_h = 1$, $NTU_c = 1$.

Case 1: Step Change in Inlet Temperature – Effect of Start-up of System

The first situation consists of a system that initially ($t^*=0$) has the same temperature for both fluids and the wall. This means that there is no heat transfer within the system because $\theta_h = \theta_c = \theta_w = 0$. At $t^*=0^+$, a step change is imposed at the inlet of one of the fluids. For this example, it was chosen to impose a step change to make one of the fluids hotter by making $\theta_h = 1$. The following conditions were modelled: M=1, C=1, $C_w=0.1$, $NTU_h=1$, $NTU_c=1$. These conditions were chosen to have two fluids with identical characteristics so that the transient behavior is not influenced more by one of the fluids. A dimensionless time-step of $\Delta t^*=1\times10^{-3}$ and a position-step $\Delta x^*=1\times10^{-2}$ were used resulting in a Courant number of 0.1.

Figure 11 shows the spatial dimensionless temperature profiles of the hot and cold fluids as well as the wall along the channels for different times. These dimensionless temperatures show

the transient behavior caused by a step change in the inlet temperature of one of the fluids. In Figure 11a, the dimensionless temperature along the tube at $t^* = 0$ is $\theta_h(t^* = 0, x^*) = 0$. For $t^* = 0^+$, the inlet temperature changes to $\theta_h(t^* > 0, x^* = 0) = 1$. In this scenario, the results shown in Figure 11a demonstrates two different transient behaviors, referred to here as a wave-like behavior and a linear behavior. At very early times, the fluid with the new inlet temperature advances along the channel displacing the fluid at the initial temperature, causing steep drops in temperature between the new (high) and initial (low) temperatures. This wave-like behavior propagates along the heat exhanger until it reaches $x^* = 1$. The residence time $t_r = u_h/L$ determines how long it takes for the fluid at the new temperature to reach the outlet of the channel. Recall that the dimensionless time is normalized by the residence time, therefore $t^* = 1$ corresponds to the time when the hot fluid has reached the end of the channel. From $t^*=0$ to $t^*=1$, the initial temperature is still having a large effect on the system temperature as shown in Figure 11a. In the region to the left of the drops, the temperature decreases with distance as it advances through the channel, because of the heat transfer to the colder wall. At times greater than $t^*=1$, the fluid at the initial temperature has been completely displaced, and the change in temperature along the reactor becomes linear everywhere. The slope of this linear temperature profile decreases with time resulting in an increase in the outlet hot temperature. The system finally reaches a new steady state (Figure 10). The temperature of the wall is influenced by the temperature of the hot fluid, but mostly shows a linear behavior as shown in Figure 11b. The temperature of the cold fluid only shows a linear behavior because the cold fluid inlet temperature hasn't changed, but the slope increases with time as shown in Figure 11c.

Around $t^*=4$, the system has reached a new steady state. These two different transient behaviors are strongly dependent on the dimensionless parameters C, M, NTU_h , NTU_c , and C_w , and the initial and boundary conditions. The wave-like behavior of the hot fluid is due to the inlet

temperature step change. After the wave passes a point in the heat exchanger, the hot fluid temperature starts increasing because of the combined effect of the new inlet temperature and the fact that the temperature of the cold fluid is increasing so the heat transfer from the hot to the cold fluid decreases (Figure 11c).

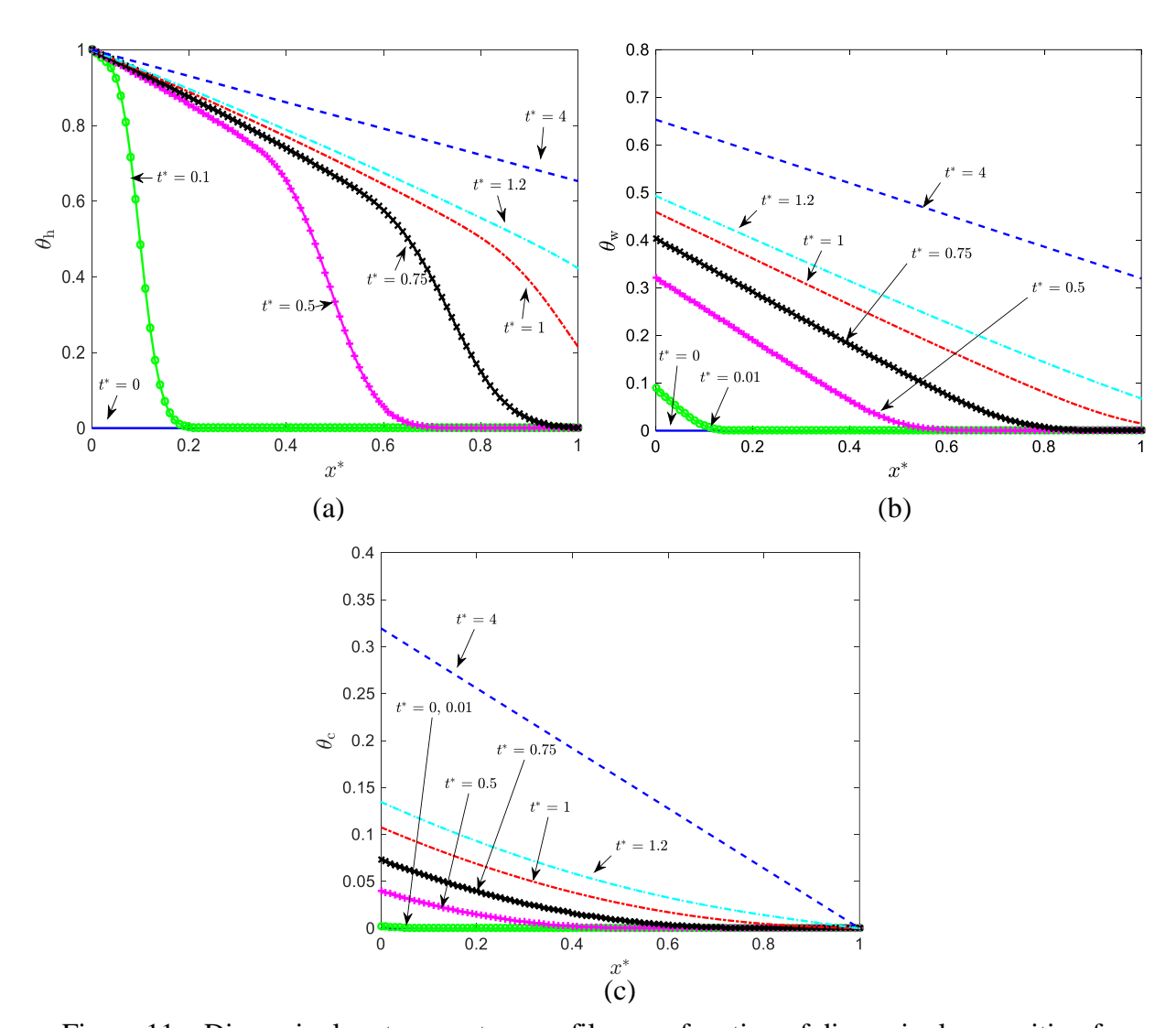


Figure 11 – Dimensionless temperature profiles as a function of dimensionless position for different times: (a) the hot fluid, (b) the wall, and (c) the cold fluid for the following condition: $M=1, C=1, C_{\rm w}=0.1, NTU_{\rm h}=1, NTU_{\rm c}=1.$

One can determine when the system has reached steady state by examining the temperature change over time. If the temperature change is small from one time step to the next, then it can be assumed that the system has reached steady state. If the criterion to determine steady state is strict $(\Delta\theta < 1\times10^{-4})$, then the hot fluid takes $t_h^* = 7.40$ to reach steady state. For this example, the parameter $t_{r,h} = 0.0233$ s ($t_{r,h}^* = 1$). The cold fluid took $t_c^* = 7.49$. It is important to notice that Figure 12a, b, and c show that the transient behavior is only significant for roughly $t_r^* < 3$. For $t_r^* > 3$, the temperatures in the whole system slowly plateau to the steady state temperatures.

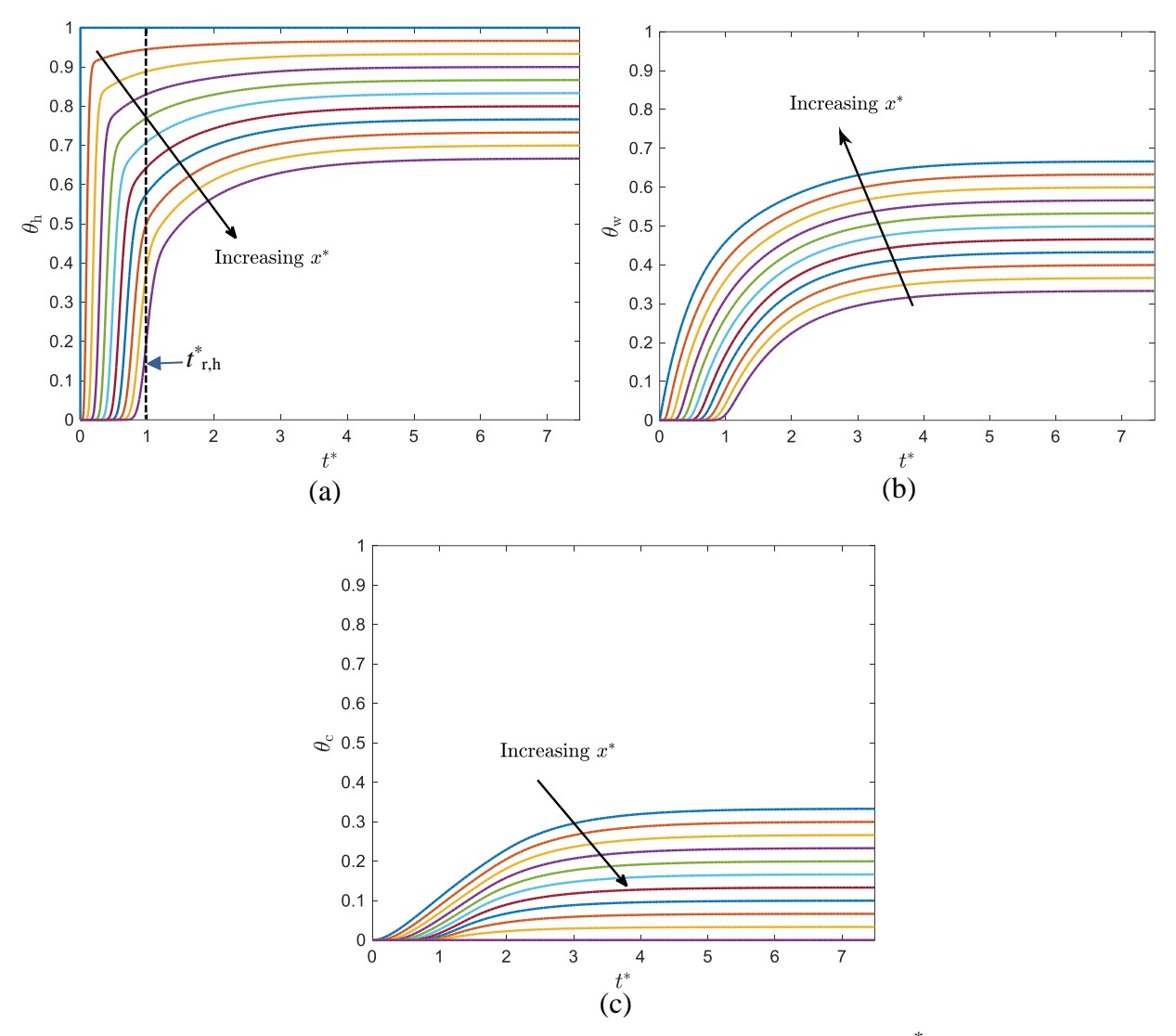


Figure 12 – Dimensionless temperature as a function of time for different x^* -locations for (a) the hot dimensionless temperature, (b) the wall dimensionless temperature, and (c) the cold dimensionless temperature.

Case 2: Step Change in Inlet Temperature – Disturbance on Steady State Solution

Case two is when the system in the first scenario has reached steady state (Figure 10), another step change at the inlet temperature is imposed. The hot inlet temperature was changed from $\theta_h = 1$ to $\theta_h = 0.75$ (25% decrease) at $t^* = 0^+$. All of the other conditions remained the same: M = 1, C = 1, $C_w = 0.1$, $NTU_h = 1$, $NTU_c = 1$. Figure 13 shows the steady-state dimensionless

temperature profiles of the hot fluid (red line), cold fluid (blue line), and the wall (green line) before (dashed lines) and after (continuous lines) a 25% change in inlet temperature. At $t^* = 0^+$, the temperature at the inlet of the hot fluid is decreased to $\theta_h|_{x^*=0} = 0.75$ as shown in Figure 13. The wall damps the oscillations in the cold stream temperature. The inlet temperature of the hot fluid decreases by 25%, but the outlet cold fluid decreases by less than 10%.

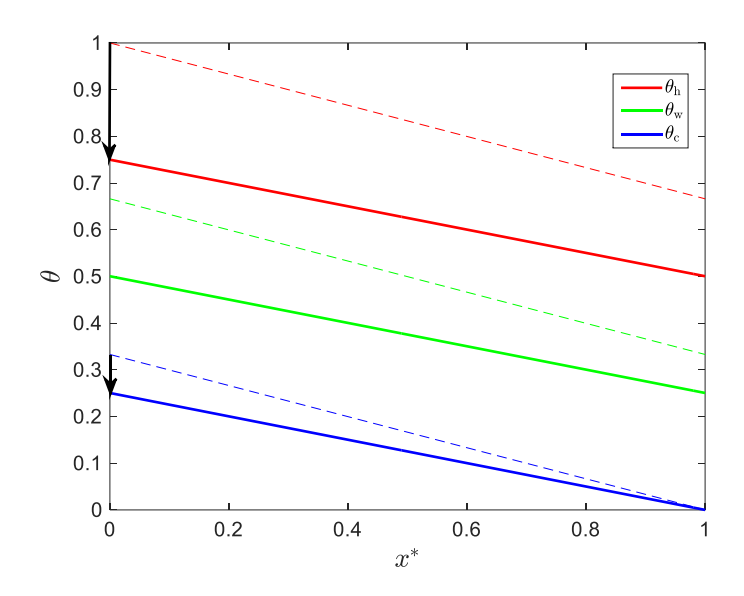


Figure 13 – Steady state temperature profiles before (dashed lines) and after (continuous lines) a 25% change in inlet temperature. Steady state temperature of hot fluid (red line), cold fluid (blue line), and the wall (green line) for the following conditions: M = 1, C = 1, $C_{\rm w} = 0.1$, $NTU_{\rm h} = 1$, $NTU_{\rm c} = 1$.

Figure 14 shows the hot fluid temperature profiles at selected dimensionless times. From $t^*=0$ to $t^*=1$, the initial temperature is still having a large effect. At times greater than $t^*=1$, the change in temperature along the reactor becomes linear. Around $t^*=6$, the system has reached steady state. The transient behavior for this case is very similar to case one. The wave-like behavior is still observed in this case, but for this case, the wave moves in between the old and new steady states shown in Figure 13. After the residence time, the wave-like behavior reaches the end of the channel, and a linear temperature profile is observed everywhere. The outlet temperature decreases

until the system reaches steady state.

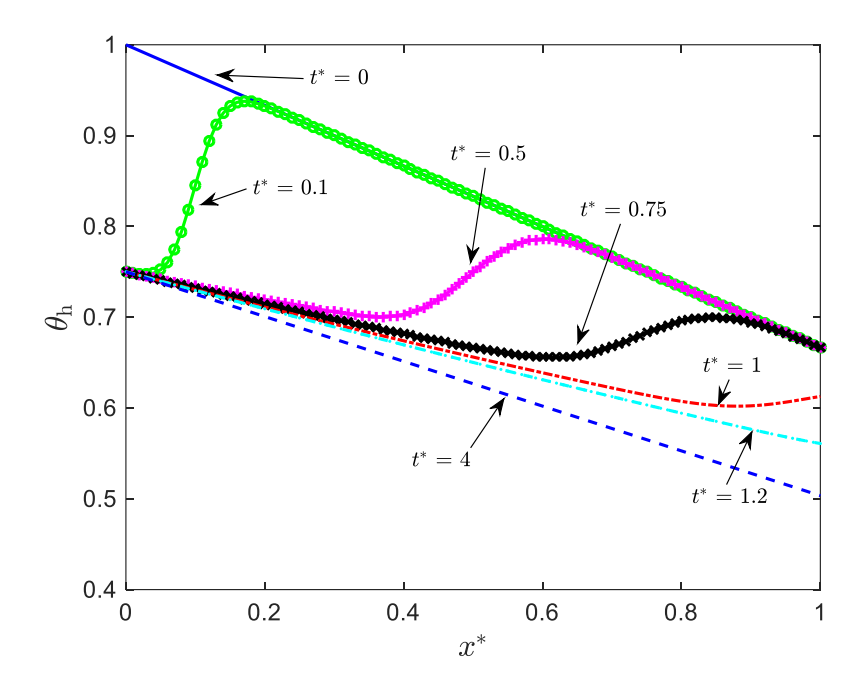


Figure 14 – Hot fluid temperature after reducing the inlet temperature of the hot fluid by 25% as a function of x for specific times.

Figure 15 shows the dimensionless temperature of the hot fluid as a function of time at different locations along the channel. At early times, the temperature far from the heat exchanger inlet has not been changed by the step change at the inlet. At time progresses, the temperature starts dropping until it reaches the new steady state. The outlet temperature of the hot fluid decreases by less than 20% with a 25% decrease in the inlet temperature. The temperature difference between the hot and the cold fluid is smaller, which causes a decrease in the heat transfer to the wall.

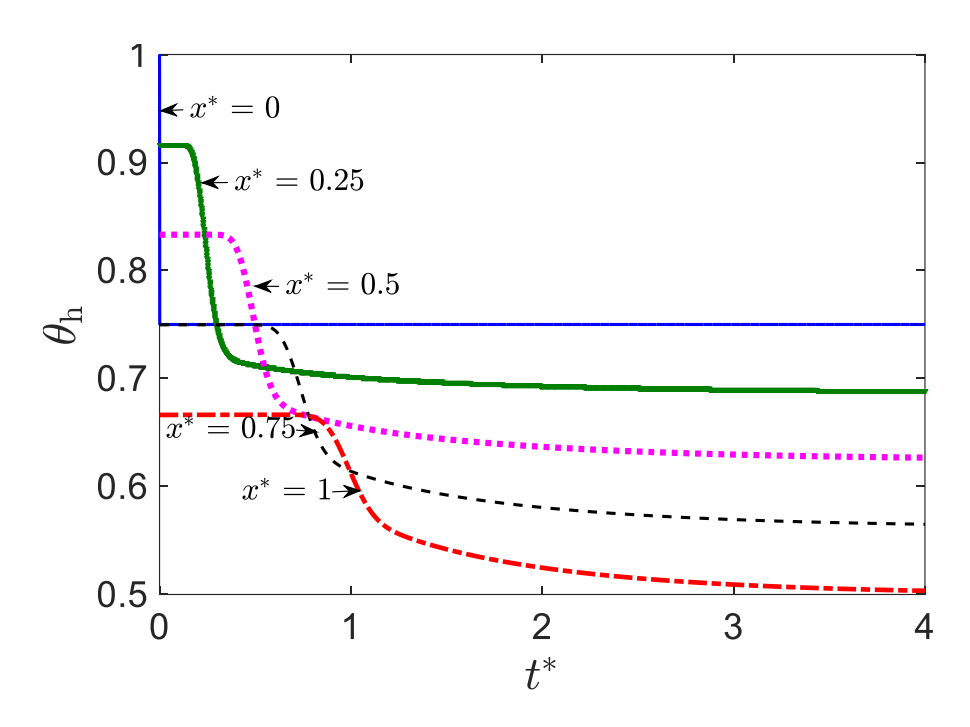


Figure 15 – Transient behavior of hot fluid after a steady state solution is disturbed with a temperature change at the inlet.

Case 3: Step Change in Inlet Mass Flow Rate – Disturbance on Steady State Solution

The case three is when a step change in one of the *mass flow rates* disrupts the steady state of case one (Figure 10). The hot mass flow rate was changed from $\dot{m}_h = 0.1 \,\mathrm{g/s}$ to $\dot{m}_h = 0.075 \,\mathrm{g/s}$ at $t^* = 0^+$. The dimensionless parameters M, NTU_h , and NTU_c change because they depend on the mass flow rate of the hot fluid. All of the other conditions stay the same: C = 1, and $C_w = 1$.

Figure 16 shows the effect a disturbance in one of the fluid's mass flow rates has on a steady state system. The initial steady state temperature profiles of both fluid and the wall are shown in dashed lines dashed lines, red for the hot fluid, green for the wall, and blue for the cold fluid. At $t^* = 0^+$, the mass flow rate of the hot fluid is decreased causing a change in the slope of the temperature profiles as shown in Figure 13. The "new" steady state solution is also shown in Figure 16 (continuous lines).

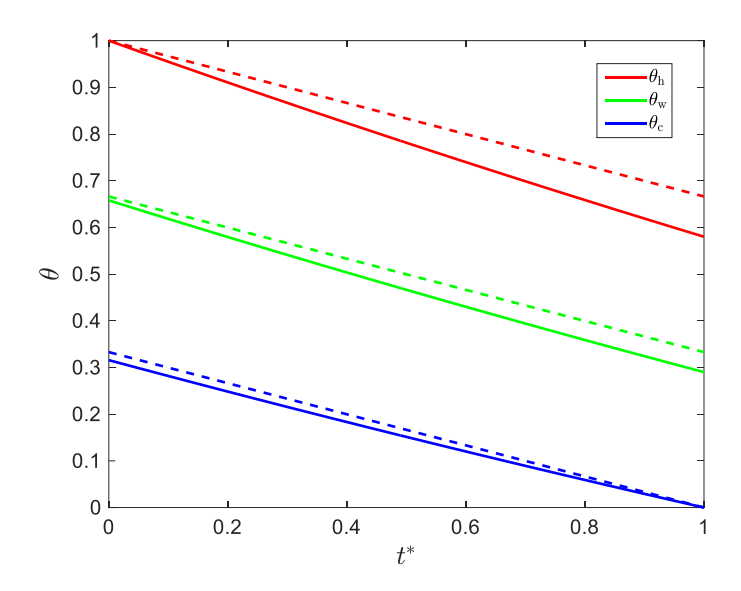


Figure 16 – Steady state temperature profiles before (dashed lines) and after (continuous lines) a 25% decrease in hot fluid mass flow rate. Steady state temperature of hot fluid (red line), cold fluid (blue line), and the wall (green line) for the following conditions: C = 1 and $C_w = 1$.

Case 4: Time Varying Inlet Temperature of One of the Flows

The fourth situation consists of a system that has both fluids and the wall at the same temperature at t^* = 0. The following conditions were modelled: M = 1, C = 1, $C_w = 1$, $NTU_h = 1$, $NTU_c = 1$. At $t^* > 0$, a step change is imposed in the inlet temperature of one of the fluids, specifically, a temperature step change of $\theta_h = 1$ is imposed at the inlet. The hot inlet temperature then varies sinusoidally with time as follows:

$$\theta_{\rm h} = \frac{1}{10} \left[\frac{\cos(10t^*)}{2} + 0.5 \right] + 0.9$$

The inlet temperature of the hot stream oscillates from 0.9 to 1 as shown in Figure 17.

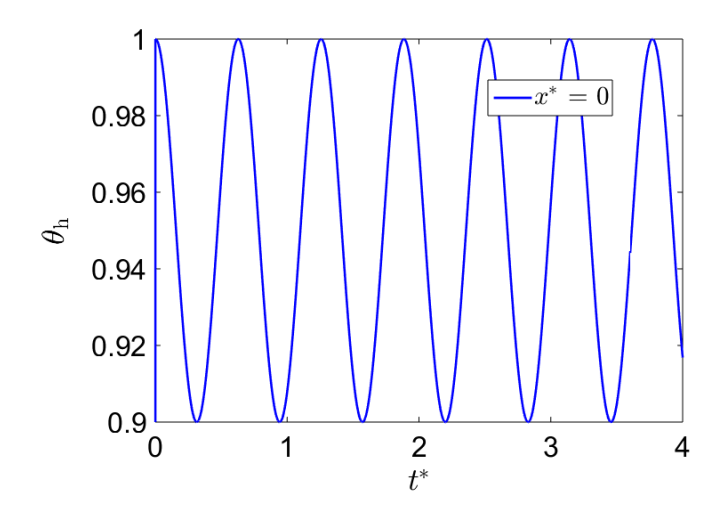
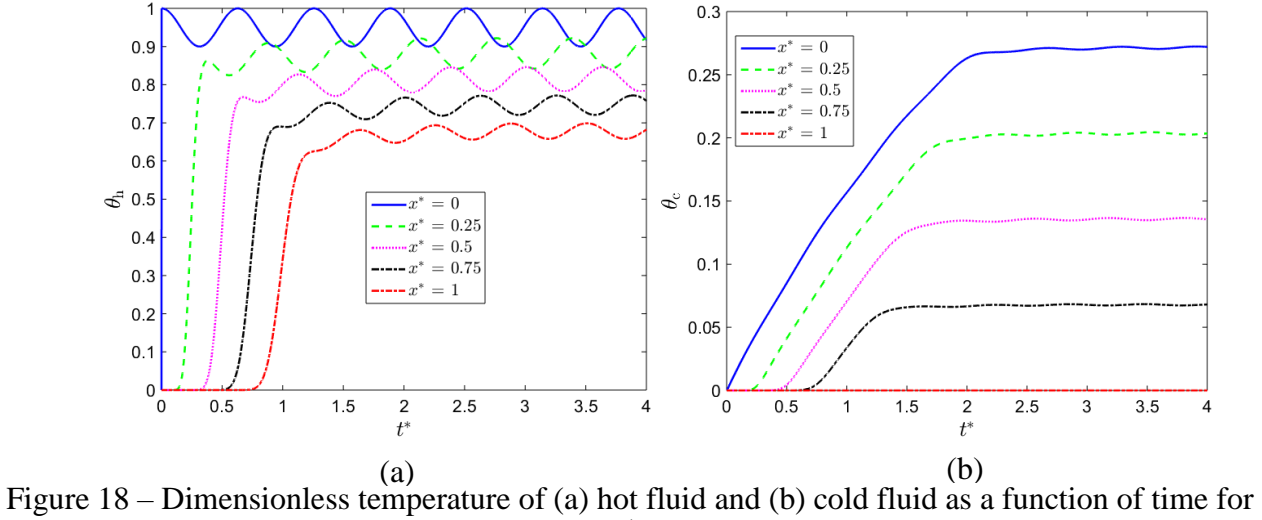


Figure 17 – Time varying inlet temperature of the hot stream.

Figure 18a and b show the dimensionless temperature profiles of the hot and cold fluids, respectively, at different locations along the channel. At $t^* = 0$, $\theta_h = \theta_c = \theta_w = 0$ everywhere. At $t^* = 0^+$, the inlet temperature of one of the flows changes to $\theta_h = 1$, and then it starts oscillating from 1 to 0.9, as shown in Figure 18a for $x^* = 0$. The oscillating behavior at the inlet then propagates along the channel. In contrast with Cases 1 - 3, Case 4 does not reach steady state due to the time varying boundary condition (although it does reach a steady-periodic solution). Figure 18b shows the dimensionless temperature of the cold fluid as a function of time for different positions along the channel. The oscillation observed in the hot fluid temperature gets damped by the heat exchange through the wall, and then to the cold fluid. The cold fluid temperature oscillations are considerably smaller compared to the oscillations observed in the hot fluid. It is important to notice that this might not be the case for a system with different conditions.



different x^* locations.

Figure 19 shows the dimensionless temperatures of the hot fluid along the channel for different time steps greater than the residence time. These dimensionless temperatures show the transient behavior caused by the oscillating inlet temperature on the hot fluid. The two limiting inlet dimensional temperatures are shown in Figure 19: $\theta_h = 1$ ($t^* = 2.5$) and $\theta_h = 0.9$ ($t^* = 8.5$). The outlet temperature oscillates between the outlet temperatures for $t^* = 2.5$ and $t^* = 8.5$.

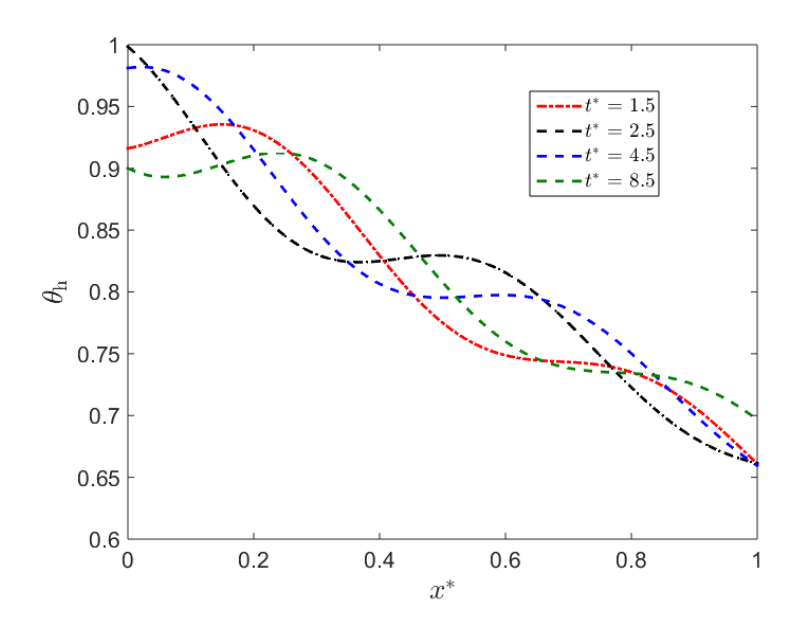


Figure 19 – Dimensionless hot temperature along the reactor for different dimensionless times.

Conclusion

The results obtained for the four different cases show that there exist different transient behaviors. For a system with different parameters, the transient behavior might be different. Therefore, a parametric study needs to be done in order to determine the effect of the parameters on the transient behavior.

Parametric Study for Time to Reach Steady State

It is of special interest to explore the effect that the non-dimensional parameters M, C, C_w , NTU_h , and NTU_c have on the transient behavior of a heat exchanger. The time that a system takes to reach steady state would help to determine the importance of the transients in the system. Also, if the time to reach steady state can be calculated before actually solving the differential equations that describe the system, the design parameters of the heat exchanger can be selected so that the system reaches steady state at a faster rate. The objective of this section is to obtain a correlation

to estimate the time that the system takes to reach steady state.

Procedure

A full study was performed to determine the time that a system takes to reach steady state and to explore how the dimensionless parameters affect this time. The following method was followed:

- 1. A scale analysis was performed using Equation 23 Equation 25 to determine the relationship between the non-dimensional parameters in Table 4 and the time the system takes to reach steady state.
- 2. The numerical model was used to perform a parametric study where each dimensionless number in Table 4 was varied independently to determine its relationship to the time the system takes to reach steady state. The results were plotted, and a curve fit was obtained for each case.
- 3. From steps 1 and 2, a general form to estimate the time it takes for the system to reach steady state was obtained.

1. Scaling Analysis

A scaling analysis on the non-dimensional differential equations (Equation 23 - Equation 25) was performed to determine a parameter that can indicate the duration of the transient effects. The time derivative of temperature can be approximated as $\Delta\theta/\Delta t$. Similarly, the *x*-derivative can be approximated as $\Delta\theta/l$, where l=1 is the dimensionless length of the heat exchanger. The storage terms to each of the other terms in the equations will be equated, one by one, to determine a characteristic time for each phenomenon – that is when the transient is dominated by each other term in the equations individually.

Advection terms

$$\frac{\Delta\theta_{\rm h}}{t_{\rm h}^*} \sim \frac{\Delta\theta_{\rm h}}{l} = \frac{\Delta\theta_{\rm h}}{1} \implies t_1^* \sim 1 \text{ for the hot fluid, and}$$
 Equation 43

$$C \frac{\Delta \theta_{\rm c}}{t_{\rm c}^*} \sim M \frac{\Delta \theta_{\rm c}}{l} = M \frac{\Delta \theta_{\rm c}}{1} \implies t_2^* \sim \frac{C}{M}$$
 for the cold fluid.

It can be seen that t_h^* is of the order of 1, and t_c^* is of the order of C/M. These relations can be used to estimate the order of magnitude of the time to reach steady state t_{st}^* due to the advection term and the storage term. A similar scaling analysis can be performed with the heat exchange terms $(NTU_h\Delta\theta)$ for the hot fluid and $NTU_c\Delta\theta$ for the cold fluid):

Heat Exchange Terms

$$\frac{\Delta \theta_{\rm h}}{t_{\rm h}^*} \sim \Delta \theta_{\rm h} \left(NTU_{\rm h} \right) \Rightarrow t_3^* \sim \frac{1}{NTU_{\rm h}}$$
 for the hot fluid, and Equation 45

$$C \frac{\Delta \theta_{\rm c}}{t_{\rm c}^*} \sim \Delta \theta_{\rm c} (NTU_{\rm c}) \Rightarrow t_4^* \sim \frac{C}{NTU_{\rm c}}$$
 for the cold fluid. Equation 46

The same analysis needs to be performed on the wall energy equation:

$$C_{\rm w} \frac{\Delta \theta_{\rm w}}{t_{\rm w}^*} \sim \Delta \theta_{\rm w} \left(NTU_{\rm h} \right) \Rightarrow t_5^* \sim \frac{C_{\rm w}}{NTU_{\rm h}}$$
 for the hot fluid, or Equation 47

$$C_{\rm w} \frac{\Delta \theta_{\rm w}}{t_{\rm w}^*} \sim \Delta \theta_{\rm w} (NTU_{\rm c}) \Rightarrow t_6^* \sim \frac{C_{\rm w}}{NTU_{\rm c}}$$
 for the cold fluid. Equation 48

These relations can be used to estimate the magnitude of the time the system takes to reach steady state when two terms balance with each other. However, a more general relationship needs to be found.

2.Parametric Study

At least two different transient behaviors were observed in Cases 1-3. From those results,

it was concluded that there were different factors that affect t_{st}^* . The numerical model was used to perform a parametric study where each dimensionless number in Table 2 was varied independently to see how it affects the time the system takes to reach steady state. The base case was a system with the following conditions: M = 1, C = 1, $C_w = 1$, $NTU_h = 1$, $NTU_c = 1$.

Effect of Dimensionless Parameter M and C

The dimensionless parameters in Table 4 were kept constant, but M (see Equation 27) varies by varying the mass flow rate of the cold fluid. This ensures that M is the only parameter that changes. M was varied from 0 to 4. The time it takes for the system to reach steady state was determined by monitoring the temperature change over time. Once all of the dimensionless temperatures meet the following criterion $(\theta^{n+1} - \theta^n)/\Delta t^* < 1 \times 10^{-4}$, then the system was assumed to be at steady state.

In order to find the dependence of the time the system takes to reach steady state on M, $t_{\rm st}^*$ is plotted as a function of M as shown in Figure 20a. Two cases were run: one for C=1, and one for C=2. The equation obtained from the fitted curve shows an inverse relationship to M as Equation 44 predicted. For the case of C=1, the following equation was obtained:

$$t_{\rm st}^* = 1.8 \left(\frac{1}{M}\right) + 2$$
.

For the case of C = 2, the following equation was obtained:

$$t_{\rm st}^* = 1.3 \left(\frac{2}{M}\right) + 3.$$

It is important to notice that for M < 1, $t_{\rm st}^*$ increases dramatically. The same procedure was performed to find the time to reach steady state dependence on C. The dimensionless time is plotted as a function of C as shown in Figure 20b. Two cases were run: one for M = 1, and one for M = 2. The dependence on C is linear as predicted in Equation 44. For the case of M = 1, the following

equation was obtained:

$$t_{\rm st}^* = 1.9C + 1.8$$
.

For the case of M = 2, the following equation was obtained:

$$t_{\rm st}^* = 0.6C + 2$$
.

As C increases, t_{st}^* also increases.

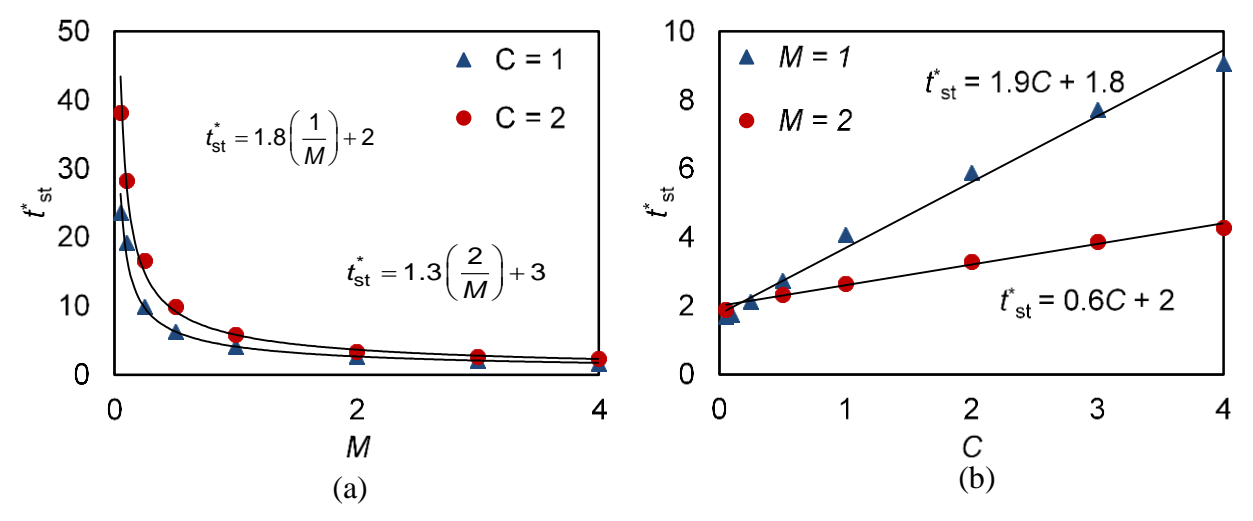


Figure 20 – Dimensionless time to reach steady state as a function of (a) M for C = 1 and C = 2, and (b) C for M = 1 and M = 2. The following parameters were kept constant: $C_w = 0.1$, $NTU_h = 1$, $NTU_c = 1$.

Effect of Dimensionless Parameter NTU_h and NTU_c

The same procedure was performed to find the time to reach steady state dependence on NTU_h and NTU_c . Figure 21a shows t_{st}^* as a function of NTU_h , and Figure 21b shows t_{st}^* as a function of NTU_c . Both plots show a logarithmic dependence on NTU_h and NTU_c . Note that this behavior was not predicted by the scaling analysis performed before (Equation 45 and Equation 46). As NTU_h or NTU_c increase, t_{st}^* also increases.

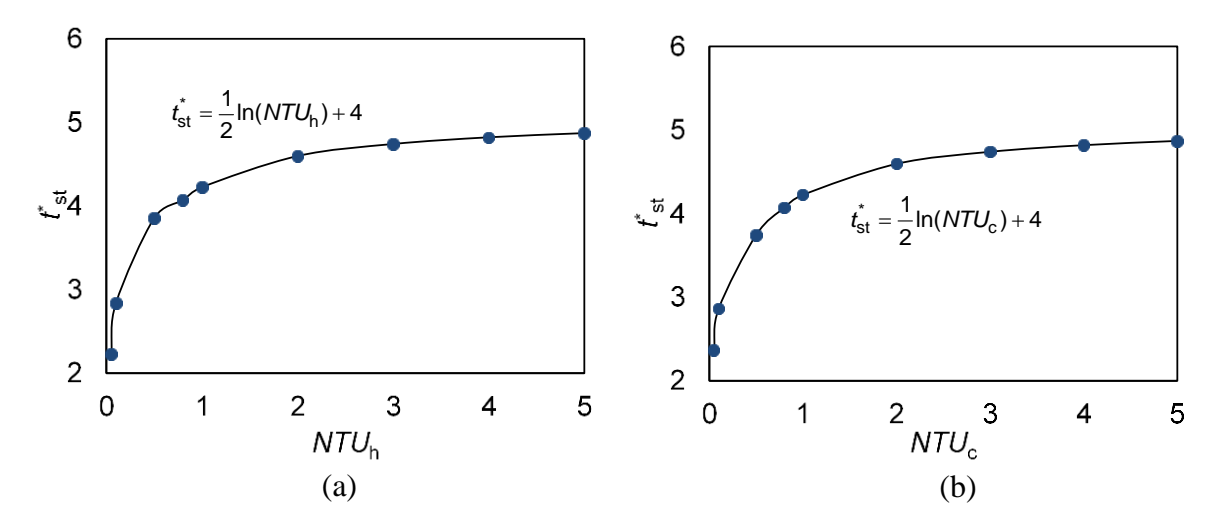


Figure 21 – Dimensionless time the system takes to reach steady state as a function of (a) NTU_h (left) and as a function of (b) NTU_c (right). The following parameters were kept constant: M = 1, C = 1, $C_w = 0.1$.

Effect of Dimensionless Parameter C_w

Finally, the dependence of $t_{\rm st}^*$ on $C_{\rm w}$ was obtained. Figure 22 shows $t_{\rm st}^*$ as a function of $C_{\rm w}$. As predicted by Equation 47 and Equation 48, $t_{\rm st}^*$ is linearly dependent on $C_{\rm w}$. It is important to notice that the slope in Figure 22 is very steep. $t_{\rm st}^*$ increases rapidly as $C_{\rm w}$ increases. This behavior was expected because an increase in $C_{\rm w}$ correlates with an increase of thermal mass of the wall.

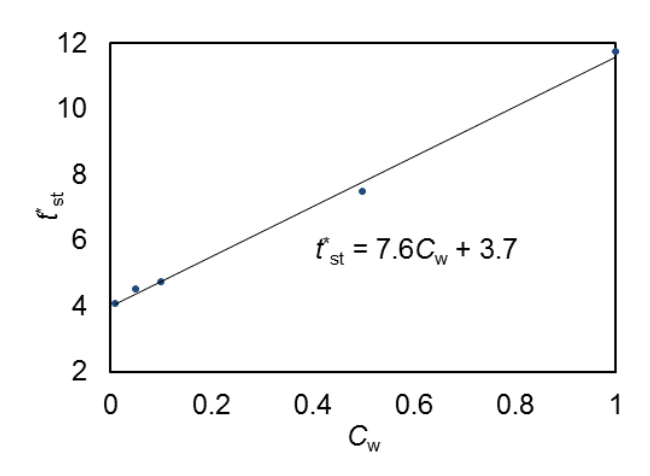


Figure 22 – Dimensionless time the system takes to reach steady state as a function of C_w . The following parameters were kept constant: M = 1, C = 1, $NTU_h = 1$, and $NTU_c = 1$.

3.General $t_{\rm st}^*$ Correlation

At least two different transient behaviors were observed in Cases 1-3. From those results, it was concluded that there were different factors that affect t_{st}^* . After the scaling analysis and the parametric study was performed, it was of special interest to find an equation that can predict how long a system takes to reach steady state. The information gathered in the parametric study was used to find a correlation that can predict t_{st}^* . The following equation was predicted:

$$t_{\text{st}}^* = t_1^* + t_2^* + t_3^* + t_4^* + t_5^* + t_6^*$$
 Equation 49

The total time for the system to reach steady state is a linear relation between the dimensionless times from the hot fluid differential equation $(t_1^* \text{ and } t_2^*)$, from the cold fluid differential equation $(t_3^* \text{ and } t_4^*)$, and the wall $(t_5^*, \text{ and } t_6^*)$.

There will be some discrepancies in the coefficients of this equation because of the criterion chosen to determine if the system is at steady state. The following correlation was found for systems where $C_{\rm w} << 1$:

$$t_{\text{st}}^* = t_1^* + t_2^* + t_3^* + t_4^*$$
 Equation 50

$$t_{\text{st}}^* = 1 + \frac{1}{2} \ln \left(NTU_{\text{h}} \right) + 2 \frac{C}{M} + \frac{C}{2} \ln \left(NTU_{\text{c}} \right)$$
 Equation 51

 ${t_5}^*$ and ${t_6}^*$ are neglected because $C_{\rm w} << 1$.

From Figure 22, it was found that t_{st}^* is linearly dependent on C_w as shown in Equation 47 and Equation 48. However, these equations also suggests that t_5^* and t_6^* are functions of NTU_h and

 NTU_c . The dependence on NTU_h and NTU_c was not determined, so the correlation is only valid for systems where $C_w \ll 1$. Notice that the coefficients chosen in the correlation are slightly different from those found in the curve fitting. Figure 23 shows the comparison between the numerical results and the results obtained from the correlation.

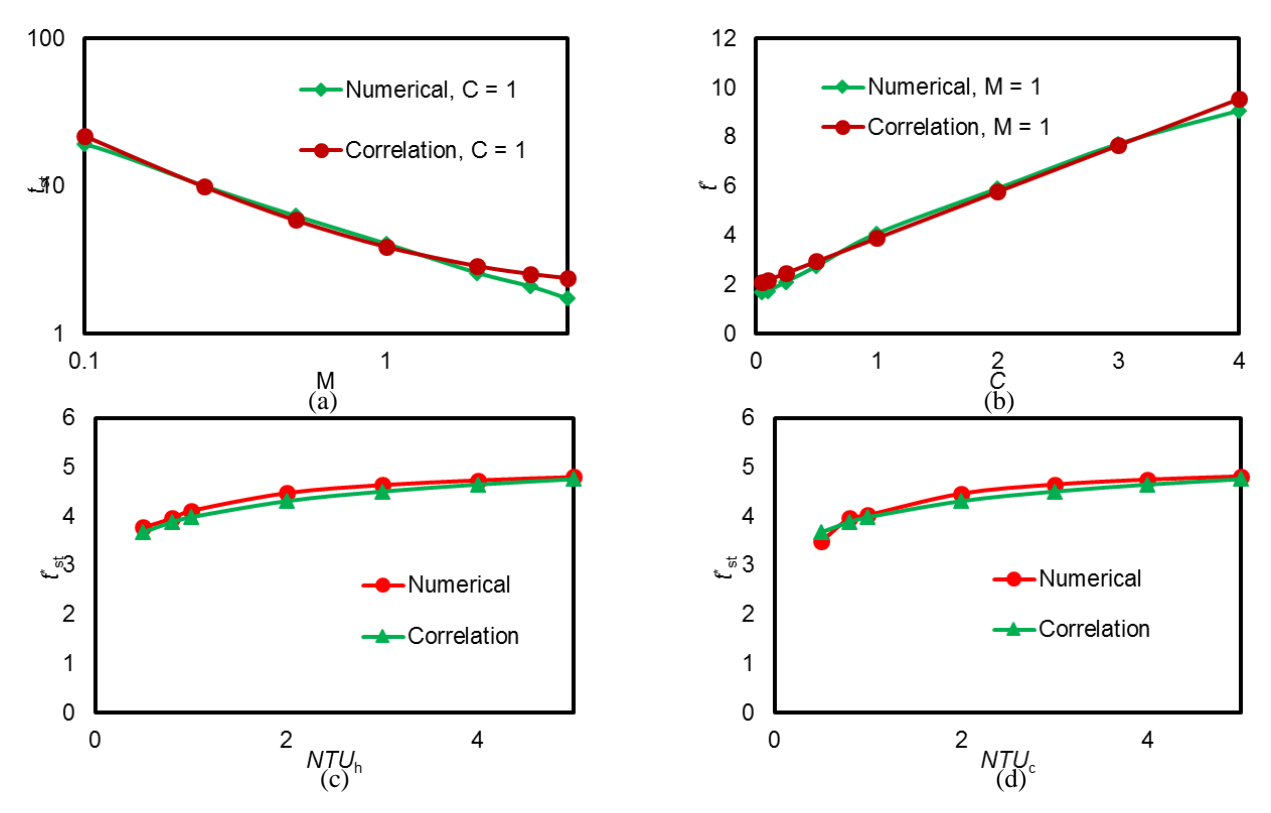


Figure $23 - t_{st}^*$ as a function of: (a) M, (b) C, (c) NTU_h and (d) NTU_c . Comparison between numerical results and the correlation results.

Figure 24 shows a comparison between t_{st}^* obtained from the numerical model (y-axis), and t_{st}^* obtained from the correlation (x-axis). The scattering on Figure 24 is due to the criterion chosen for this analysis. In this analysis the criterion was very strict, however if a different criterion is chosen, t_{st}^* would be slightly higher or slightly lower.

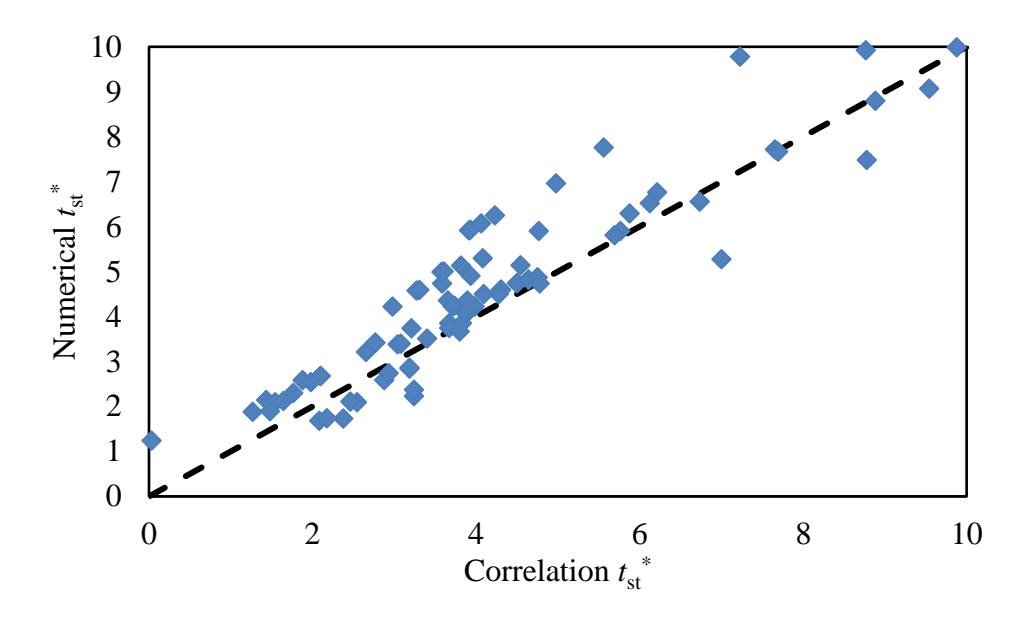


Figure 24 – Comparison between $t_{\rm st}^*$ numerical and correlation results.

CHAPTER 4: Counter Flow Reactor –Heat Exchanger Transient Behavior Analysis

In this chapter, an ammonia synthesis reactor heat exchanger was investigated. The numerical model described in Chapter 2 was modified to study the transient behavior of an ammonia synthesis reactor heat exchanger used for energy storage. The energy released by the ammonia synthesis reaction is used to heat supercritical steam to temperatures on the order of 650°C as required for a supercritical steam Rankine cycle. The goal was to explore the different transient behaviors in the ammonia synthesis reactor heat exchanger. Also, an optimum design for a rapid startup was investigated.

Motivation

The global demand for nonrenewable energy sources is growing faster than the world's ability to increase supply, resulting in elevated gasoline and electricity prices and energy dependency on other countries. Renewable energy can become a significant part of the national and global clean energy supply and can be effectively used to move the United States towards energy independence. Solar energy, in particular, has the potential to meet our energy needs if economically viable energy storage can be incorporated into CSP plants, allowing solar energy to be dispatched as a base load power plant. State-of-the-art CSP plants use molten salt as the thermal energy storage fluid. Molten salt has limitations such as degradation under thermal cycling, corrosiveness, and cost.

An ammonia thermochemical energy storage system is an alternative solution to the stateof-the-art molten salt TES system for concentrating solar power. State-of-the-art CSP plants use molten salt to store thermal energy. In contrast, TCES technologies store and release energy by making and breaking chemical bonds. Thermochemical storage has the potential for significantly higher volumetric energy density than sensible energy storage. Some of the advantages of this emerging technology include its high energy density, no heat losses during the storage duration, and the possibility of long storage periods.

Ammonia-based Thermochemical Energy Storage System Concept

The concept of ammonia-based TCES as conceived and developed at Australian National University (ANU) is described in the review paper by Dunn et al. [22]. The ammonia storage system is based on the reversible dissociation and synthesis of ammonia:

$$2NH_3 + \Delta H_{rxn} \rightleftharpoons N_2 + 3H_2$$
 Equation 52

A schematic of an ammonia-based CSP is shown in Figure 25. The heliostats concentrate the energy from the sun to the receiver located at the top of the tower. An endothermic reactor located in the receiver uses the solar energy to power the reaction to partially disassociate ammonia into hydrogen and nitrogen. The resulting hydrogen-nitrogen-ammonia mixture is used to preheat the incoming ammonia and is stored underground at ambient temperature for later use. Under the pressures and temperatures of storage, ammonia will be in the liquid phase, which helps to separate the ammonia from the hydrogen and nitrogen gas mixture. In the energy recovery process, the hydrogen-nitrogen mixture is preheated, and the reverse reaction is carried out: a hydrogen-nitrogen mixture flowing through a catalyst bed undergoes the exothermic ammonia synthesis reaction. The heat generated by the reaction is then used to heat up supercritical steam to run the turbine. It is important to mention that the ammonia-based TCES is not limited to run with a supercritical steam Rankine cycle; a sCO₂ Brayton cycle could also be used instead of a supercritical steam cycle, as will be discussed later. This closed loop system operates at elevated

pressure (in the range 10 to 30 MPa) for reasons which will be explained later.

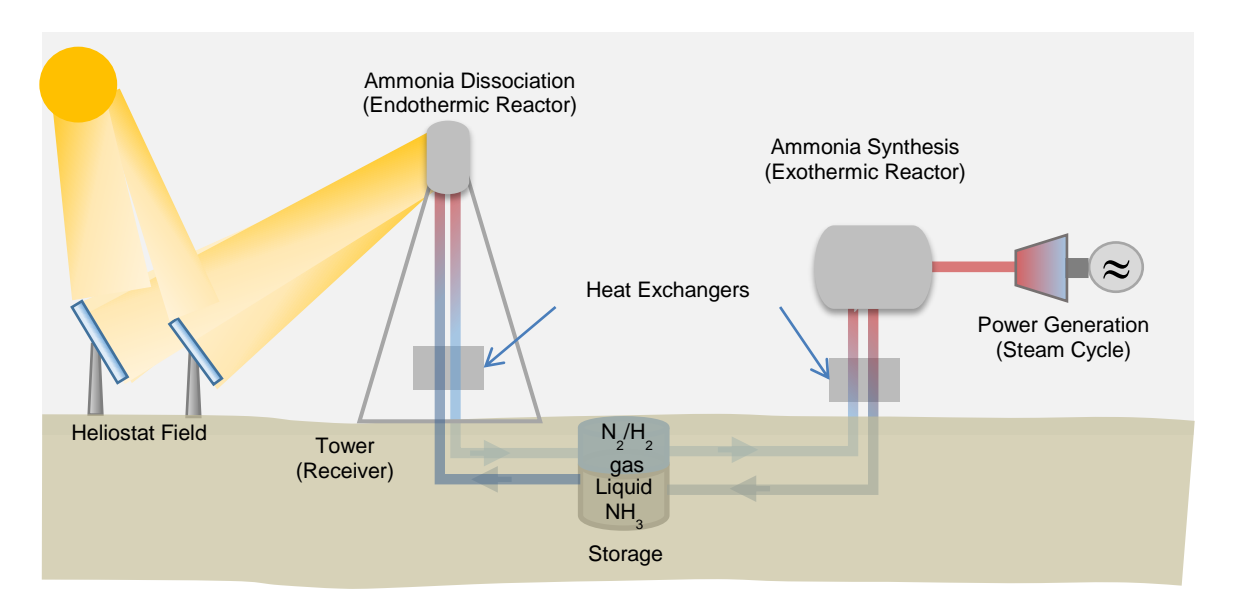


Figure 25 – Ammonia-based thermochemical energy storage system.

Relative to other proposed TCES technologies, ammonia-based TCES has many benefits:

- The reactants and products are abundant and cheap.
- The reversible dissociation-synthesis reaction has no side reactions.
- At the proposed operating temperatures ammonia, nitrogen, and hydrogen remain stable.
- Ammonia (which is liquid at ambient temperature and modest pressure) and the hydrogen/nitrogen gas mixture can be stored in the same tank with automatic phase separation.
- Ammonia synthesis and handling has been widely studied in industry
- There has been significant prior research and development of solar TCES using ammonia at the Australian National University (ANU).
- Ammonia-based TCES can work for all different types of CSP (parabolic trough, dish, tower) because the dissociation reaction can be carried out over a range of temperatures with different catalysts [23].

At the same time, there are some challenges associated with ammonia for TCES:

- The enthalpy of reaction is modest: $\Delta Hr = 66,800 \text{ kJ/kmol}$ at 298 K and 30 MPa (a typical pressure proposed for the reaction [24]).
- The products are gases, and therefore possess low density; the required storage volume is the same order of magnitude as for two-tank molten salt, but at an elevated pressure.

This idea was extensively investigated at the Australian National University (ANU) [22, 23, 25-34]. Despite these drawbacks, the many positive attributes of ammonia TCES make it a strong candidate for further investigation and development.

Numerical Model for Transient Reactor Heat Exchanger

A steady state two-dimensional computational model for the ammonia synthesis process was developed at ANU [35]. Although this model provides useful information of the system behavior under steady state, the model does not provide any information on the transient regime. Another limitation of this computational model is that it solves the differential equations by marching in space from one end of the reactor to the other. This method does not allow the user to input the inlet temperature of both of the fluids in the counter-flow heat exchanger. The inlet temperature of the hydrogen/nitrogen mixture and the outlet temperature of the steam are required as inputs.[35] This becomes a problem because the ammonia synthesis reaction is strictly linked to the outlet temperature of the steam. The initial guess of the temperatures can result in a non-realistic scenario.

A transient numerical model was developed for a transient counter-flow reactor heat exchanger. This model was used to determine the optimum conditions for the system to reach steady state in a reasonable amount of time as well as getting the operational temperatures needed for the power block. The algorithm also provides information on the response to disturbances in

the system. It is desired to determine the startup time of the reactor. An optimum system should take a maximum of 10 minutes to get to the operational temperatures to generate the desired energy. The goal is to determine if the system is able to reach steady state in 10 min or under.

System Modeling

The model consists of a transient one dimensional concentric tube counter-flow reactor heat exchanger as shown in Figure 26. There is gas (H₂/N₂) flowing through the channel that contains an iron-based catalyst bed. The catalyst bed is separated from the steam by an Inconel wall. The radially lumped temperatures of the gas, steam, and wall are each modeled. Axial conduction is neglected. Heat transfer between the reactor and the surroundings is negligible (although this can readily be modified).

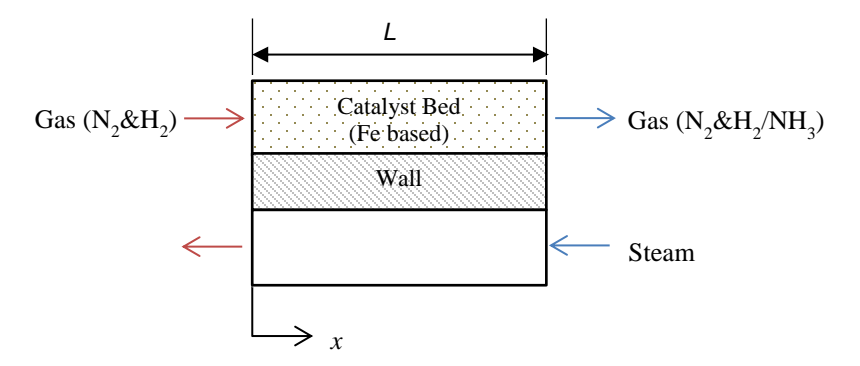


Figure 26 – Schematic of the one dimensional radially lumped reactor heat exchanger model.

The numerical model solves the four coupled differential equations shown below:

$$\begin{split} \left(\rho c_{\mathrm{p}} A_{\mathrm{c}}\right)_{\mathrm{g}} \left(\frac{\partial T_{\mathrm{g}}}{\partial t} + u_{\mathrm{g}} \frac{\partial T_{\mathrm{g}}}{\partial x}\right) - \left(k A_{\mathrm{c}}\right)_{\mathrm{g}} \frac{\partial^2 T_{\mathrm{g}}}{\partial x^2} + (h P)_{\mathrm{g}} \left(T_{\mathrm{g}} - T_{\mathrm{w}}\right) = \dot{r}''' A_{\mathrm{c,g}} \Delta h_{\mathrm{rxn}} \end{split}$$
 Equation 53
$$\left(\rho c_{\mathrm{p}} A_{\mathrm{c}}\right)_{\mathrm{s}} \left(\frac{\partial T_{\mathrm{s}}}{\partial t} - u_{\mathrm{s}} \frac{\partial T_{\mathrm{s}}}{\partial x}\right) - \left(k A_{\mathrm{c}}\right)_{\mathrm{s}} \frac{\partial^2 T_{\mathrm{s}}}{\partial x^2} + (h P)_{\mathrm{s}} \left(T_{\mathrm{s}} - T_{\mathrm{w}}\right) = 0 \end{split}$$
 Equation 54
$$\left(\rho c_{\mathrm{p}} A_{\mathrm{c}}\right)_{\mathrm{w}} \frac{\partial T_{\mathrm{w}}}{\partial t} - \left(k A\right)_{\mathrm{w}} \frac{\partial^2 T_{\mathrm{w}}}{\partial x^2} - (h P)_{\mathrm{g}} \left(T_{\mathrm{g}} - T_{\mathrm{w}}\right) - (h P)_{\mathrm{s}} \left(T_{\mathrm{s}} - T_{\mathrm{w}}\right) = 0 \end{split}$$
 Equation 55
$$\left(\rho A_{\mathrm{c}}\right)_{\mathrm{g}} \left(\frac{\partial f_{\mathrm{NH}_3}}{\partial t} + u_{\mathrm{g}} \frac{\partial f_{\mathrm{NH}_3}}{\partial x}\right) = \dot{r}''' A_{\mathrm{c,g}} \end{split}$$
 Equation 56

where \dot{r}''' is the rate of production of mass of ammonia per unit volume, given by the Temkin-Pyzhev [36] expression:

$$\dot{r}''' = k_0 \exp\left[-\frac{E_a}{RT_g}\right] \left(K_a^2 a_{N_2}^2 \left(\frac{a_{H_2}^3}{a_{NH_3}^2}\right)^{\alpha} - \left(\frac{a_{NH_3}^2}{a_{H_2}^3}\right)^{(1-\alpha)}\right) M_{NH_3}$$
 Equation 57

Equation 53, Equation 54, and Equation 55 are the energy equations for the catalyst bed channel, the steam section, and the wall, respectively. The first term of Equation 53 represents the storage term; the second term represents advection in the flow; the third term represents the axial conduction in the channel, and fourth term represents the heat transferred from the gas to the wall. The heat generated by the reaction is represented in the last term of Equation 53. Equation 54 is very similar to Equation 53, except there is no heat generated, and the last term represents the heat transferred from the wall to the steam. Equation 55 has the wall storage term (first term), the axial conduction on the wall (second term), the heat transferred from the gas to the wall (third term), and the heat transferred from the wall to the steam (last term). Equation 56 is the mass species

balance on the gas in the catalyst bed. Both Equation 53 and Equation 56 contain the reaction rate, \dot{r}''' which can be calculated using Equation 57. The reaction rate is a function of gas temperature and composition.

The supercritical steam heat transfer coefficient was calculated using Jackson's correlation for forced convective heat transfer in water at supercritical pressures 2 a modified version of the Krasnoschekov and Protopopov equation [37]:

$$Nu_{s} = \frac{h_{s}D_{h,s}}{k_{s}} 0.0183 Re_{s}^{0.82} Pr_{s}^{0.5} \left(\frac{\rho_{s,w}}{\rho_{s}}\right)^{0.3} \left(\frac{\overline{c}_{p}}{c_{p}}\right)^{n}$$
Equation 58

$$\begin{split} n &= 0.4 \quad \text{for } T_{\text{s}} \leq T_{\text{w}} \leq T_{\text{pc}} \text{ and for } 1.2T_{\text{pc}} \leq T_{\text{s}} \leq T_{\text{w}}; \\ n &= 0.4 + 0.2 \bigg(\frac{T_{\text{w}}}{T_{\text{pc}}} - 1 \bigg) \quad \text{for } T_{\text{s}} \leq T_{\text{pc}} \leq T_{\text{w}}; \\ n &= 0.4 + 0.2 \bigg(\frac{T_{\text{w}}}{T_{\text{pc}}} - 1 \bigg) \bigg[1 - 5 \bigg(\frac{T_{\text{s}}}{T_{\text{pc}}} - 1 \bigg) \bigg] \\ \text{for } T_{\text{pc}} \leq T_{\text{s}} \leq 1.2T_{\text{pc}} \text{ and } T_{\text{s}} \leq T_{\text{w}} \end{split}$$

The steam Nusselt number in Equation 58 is a function of the Reynolds number, Prandtl number, steam and wall temperature, and the steam pseudocritical temperature. It is important to notice that this correlation takes into account the rapid changes of steam properties due to the pseudocritical temperature. The pseudocritical temperature (T_{pc}) of steam at 26 MPa is 386.35 °C.

The boundary condition for the mass fraction equation is specified in Equation 59 and Equation 60. The boundary conditions for the energy equations of the gas and the steam are specified by Equation 61 - Equation 64. The inlet boundary conditions on the flows can be either constant or vary with time. The wall at x = 0 and x = L is set to have no heat flux as described in Equation 65.

$$\begin{aligned} \left. f_{\text{NH}_3}(x=0,t) = f_{\text{NH}_3,i} \right| & \text{Equation 59} \\ \left. \frac{\partial f_{\text{NH}_3}}{\partial x} \right|_{x=L} & = 0 \end{aligned} \qquad \qquad \text{Equation 60} \\ T_g(x=0,t) = T_{g,i} & \text{Equation 61} \\ \left. \frac{\partial T_g}{\partial x} \right|_{x=L} & = 0 \end{aligned} \qquad \qquad \text{Equation 62} \\ T_s(x=L,t) = T_{s,i} & \text{Equation 63} \\ \left. \frac{\partial T_s}{\partial x} \right|_{x=0} & = 0 \end{aligned} \qquad \qquad \text{Equation 64} \\ \left. \frac{\partial T_w}{\partial x} \right|_{x=0} & = \frac{\partial T_w}{\partial x} \right|_{x=1} & = 0 \end{aligned} \qquad \qquad \text{Equation 65}$$

The initial temperature of the gas, the steam, and the wall also need to be specified. Equation 68, Equation 67, Equation 68, and Equation 69 are the initial conditions on the gas, steam, wall, and the mass fraction, respectively. These initial conditions can be either constant or vary with *x* along the reactor.

$$T_{\rm g}(x,t=0) = T_{\rm g,0}$$
 Equation 66
$$T_{\rm s}(x,t=0) = T_{\rm s,0}$$
 Equation 67
$$T_{\rm w}(x,t=0) = T_{\rm w,0}$$
 Equation 68
$$f_{\rm NH_3}(x,t=0) = f_{\rm NH_2,0}$$
 Equation 69

The gas is assumed to be at a constant pressure of 30 MPa. The steam is assumed to be at a constant pressure of 26 MPa. The properties of the gas and steam are only functions of temperature, but are found at the previous time step. The properties of the wall are assumed

constant at all times, and locations.

Crank-Nicolson backward difference scheme was chosen for the discretization of Equation 53, Equation 54, and Equation 55. The reaction rate is calculated using the known temperature and gas composition at the previous time in Equation 57. Equation 56 is then used to solve for the new mass fraction of ammonia. Once the mass fraction and the reaction rate are known at each position, the system of Equation 53, Equation 54, and Equation 55 are solved simultaneously to get the temperature of the gas, the wall, and the steam at each position for the new time step. The following expressions were obtained:

$$\begin{split} \left(A_{c}\rho c_{p}\right)_{g,i}^{n} \frac{T_{gi}^{n+1} - T_{gi}^{n}}{\Delta t^{*}} + \left(A_{c}\rho c_{p}u\right)_{g,i}^{n} \frac{T_{gi}^{n} - T_{g,i-1}^{n}}{2\Delta x^{*}} + \frac{T_{gi}^{n+1} - T_{g,i-1}^{n+1}}{2\Delta x} - \dots \\ \dots - (kA)_{g} \frac{T_{gi+1}^{n+1} - T_{gi}^{n+1} + T_{gi-1}^{n+1}}{2\Delta x^{2}} - (kA)_{g} \frac{T_{g,i+1}^{n} - T_{g,i}^{n} + T_{g,i-1}^{n}}{2\Delta x^{2}} + \dots \\ \dots + \frac{(hP)_{g}}{2} \left(T_{g,i}^{n} - T_{w,i}^{n}\right) + \frac{(hP)_{g}}{2} \left(T_{g,i}^{n+1} - T_{w,i}^{n+1}\right) + \left(\dot{r}^{\textit{m}}A_{c,g}\Delta h_{rxn}\right)_{g,i}^{n} = 0 \\ \left(A_{c}\rho c_{p}\right)_{s,i}^{n} \frac{T_{s,i}^{n+1} - T_{s,i}^{n}}{\Delta t} + \left(A_{c}\rho c_{p}u\right)_{s,i}^{n} \frac{T_{s,i}^{n} - T_{s,i-1}^{n}}{2\Delta x} + \left(A_{c}\rho c_{p}u\right)_{s,i}^{n} \frac{T_{s,i+1}^{n+1} - T_{s,i}^{n+1}}{2\Delta x} - \dots \\ \dots - (kA)_{s}^{n} \frac{T_{s,i+1}^{n+1} - T_{s,i}^{n+1} + T_{s,i-1}^{n+1}}{2\Delta x^{2}} - (kA)_{s}^{n} \frac{T_{s,i+1}^{n} - T_{s,i}^{n} + T_{s,i-1}^{n}}{2\Delta x^{2}} + \dots \\ \dots + \frac{(hP)_{s}^{n}}{2} \left(T_{s,i}^{n} - T_{w,i}^{n}\right) + \frac{(hP)_{s}^{n}}{2} \left(T_{s,i}^{n+1} - T_{w,i}^{n+1} + T_{w,i-1}^{n+1}} - (kA)_{w}^{n} \frac{T_{w,i+1}^{n} - T_{w,i}^{n} + T_{w,i-1}^{n}}{2\Delta x^{2}} + \dots \\ \dots + \frac{(hP)_{s}^{n}}{2} \left(T_{s,i}^{n} - T_{w,i}^{n}\right) + \frac{(hP)_{s}^{n}}{2} \left(T_{s,i}^{n+1} - T_{w,i}^{n+1} - T_{w,i}^{n+1}\right) + \dots \\ \dots + \frac{(hP)_{s}^{n}}{2} \left(T_{s,i}^{n} - T_{w,i}^{n}\right) + \frac{(hP)_{s}^{n}}{2} \left(T_{s,i}^{n+1} - T_{w,i}^{n+1} - T_{w,i}^{n+1}\right) + \dots \\ \dots + \frac{(hP)_{s}^{n}}{2} \left(T_{s,i}^{n} - T_{w,i}^{n}\right) + \frac{(hP)_{s}^{n}}{2} \left(T_{s,i}^{n+1} - T_{w,i}^{n+1} - T_{w,i}^{n+1}\right) = 0 \end{split}$$

The Courant number (Co) for both of the fluids is calculated, and the highest Co number is used to calculate the position and time step size required for the stability of the system. The

following relationship is used to insure convergence:

$$Co_i = \frac{u_i \Delta t}{\Delta x} < 0.1, \ (i = h,c)$$
 Equation 70

where Δt and Δx are the time and position step, respectively.

Reactor Heat Exchanger Model

A small scale concentric tube reactor heat exchanger designed at UCLA [38, 39] was modeled to explore the transient response of the synthesis reaction and its effect on the supercritical steam. The dimensions of the small scale reactor are presented in Figure 27. The steam enters the inner tube at x = L, while the gas enters the annulus that contains the catalyst bed at x = 0. An Inconel wall separates the gas from the steam.

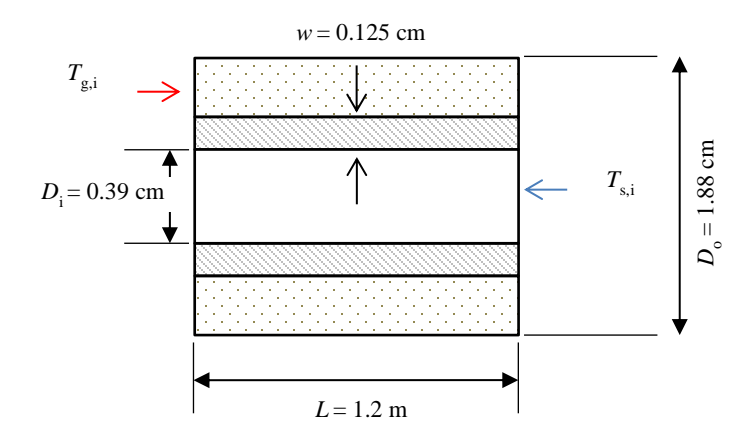


Figure 27 – Dimensions of small scale reactor heat exchanger.

The steam inlet temperature remains at 288°C. The mass flow rate of the gas is 0.1 g/s, while the mass flow rate of the steam is 0.08 g/s. An average heat transfer coefficient between the wall and the gas was calculated using the heat transfer coefficient described by Richardson et al. [24]. The average value calculated was 200 W/m²-K. The heat transferred between the wall and

the steam is calculated using Equation 58 at each time step.

Verification of Numerical Model

The synthesis reactor heat exchanger transient numerical model was verified. The transient numerical model was used to obtain the steady state solution for a reactor heat exchanger (includes chemical reaction). Axial conduction was negligible for this study. The results were compared to the solution obtained from a steady state model developed by Lavine at UCLA. Figure 28 (left) shows the mass fraction of N₂H₂ mixture as a function of position *x* as time increases. Figure 28 (right) shows the gas temperature as a function of position *x* as time increases. From Figure 28, one can see the excellent agreement between both steady state solutions.

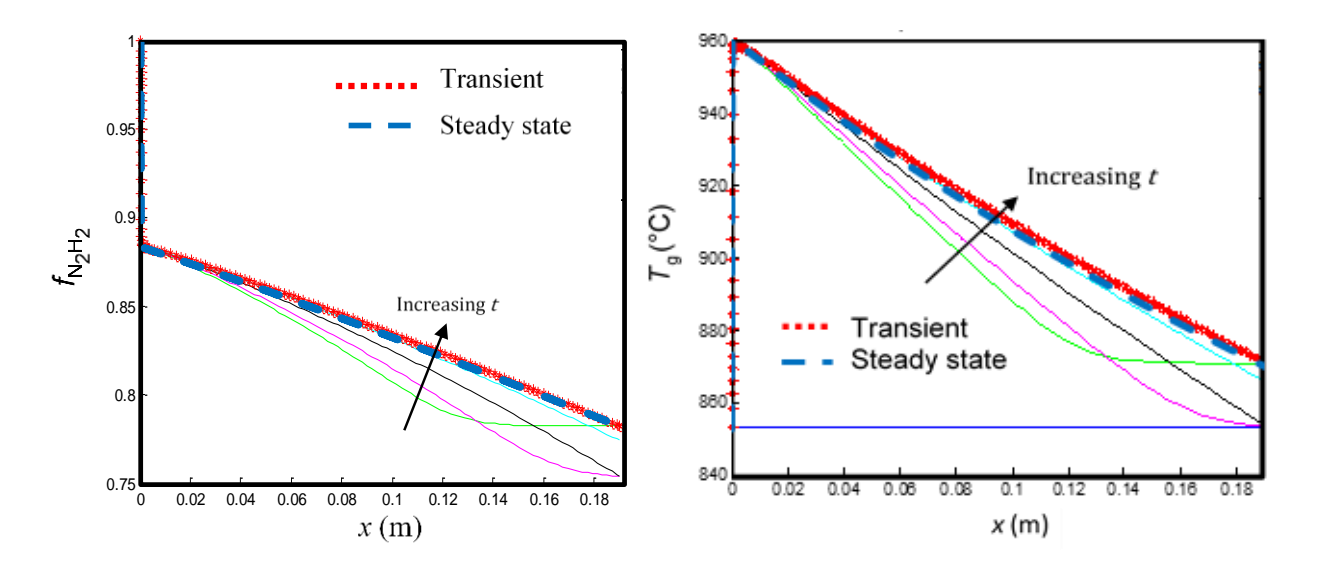


Figure 28 – Comparison of the steady state solution to a steady state problem (blue dashed lines) and the solution to a transient problem (red starred lines). Left: mass fraction of N_2H_2 mixture as a function of position x for different time steps. Right: gas temperature as a function of position x for different time steps.

Validation of the Model

The numerical model was also validated by comparing the results to the experimental results obtained from the synthesis reactor heat exchanger built at UCLA (Refer to reference [40] for more details on the experiment). The reactor heat exchanger at UCLA side view is shown in Figure 29. The reactor heat exchanger consists of a tube-in-tube configuration with the catalyst bed in the outer annulus and steam flow through the inner tube. In order to improve steam heat transfer, a third tube within the inner tube was inserted so that the steam channel is a narrow annulus—the gap is 0.7 mm. By decreasing the lateral dimension of the steam channel, the steam heat transfer coefficient is increased.

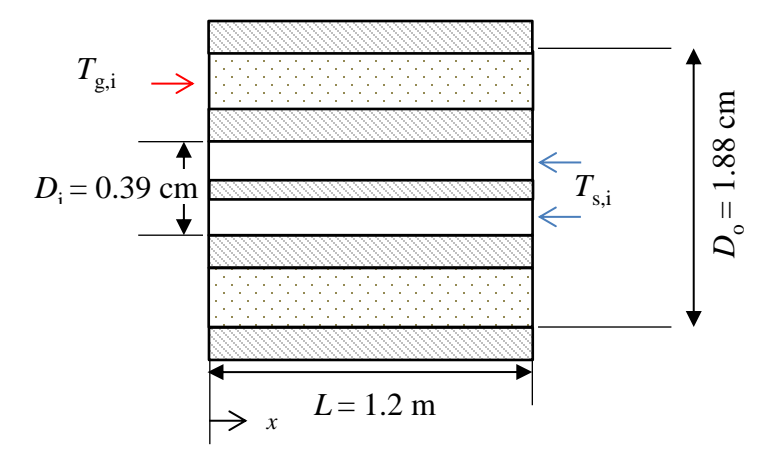


Figure 29 – Side view geometry along the reactor heat exchanger build at UCLA [40]

The model was modified to better predict the behavior of the real system. Equation 53, Equation 54, and Equation 55 were modified to include an outer wall, thermal losses, and axial conduction, and an extra equation for the outer wall was included as shown below:

$$\left(\rho c_{p} A_{c}\right)_{\text{wo}} \frac{\partial T_{\text{wo}}}{\partial t} - (kA)_{\text{wo}} \frac{\partial^{2} T_{\text{wo}}}{\partial x^{2}} - (hP)_{g} \left(T_{g} - T_{\text{wo}}\right) - \frac{\left(T_{\text{wo}} - T_{\text{amb}}\right)}{R_{\text{tot}}^{2}} = 0$$
 Equation 71
$$\left(\rho c_{p} A_{c}\right)_{g} \left(\frac{\partial T_{g}}{\partial t} + u_{g} \frac{\partial T_{g}}{\partial x}\right) - \left(kA_{c}\right)_{g} \frac{\partial^{2} T_{g}}{\partial x^{2}} + (hP)_{g} \left(T_{g} - T_{\text{wi}}\right) + \dots$$

$$\dots + (hP)_{g} \left(T_{g} - T_{\text{wo}}\right) = \dot{r}''' A_{c,g} \Delta h_{\text{rxn}}$$
 Equation 73
$$\left(\rho c_{p} A_{c}\right)_{s} \left(\frac{\partial T_{s}}{\partial t} - u_{s} \frac{\partial T_{s}}{\partial x}\right) - \left(kA_{c}\right)_{s} \frac{\partial^{2} T_{s}}{\partial x^{2}} + (hP)_{s} \left(T_{s} - T_{\text{wi}}\right) = 0$$
 Equation 74
$$\left(\rho c_{p} A_{c}\right)_{\text{wi}} \frac{\partial T_{\text{wi}}}{\partial t} - (kA)_{\text{wi}} \frac{\partial^{2} T_{\text{wi}}}{\partial x^{2}} - (hP)_{g} \left(T_{g} - T_{\text{wi}}\right) - (hP)_{s} \left(T_{s} - T_{\text{wi}}\right) = 0$$
 Equation 74

Equation 71 is the energy balance on the reactor heat exchanger outer wall. The subscripts w_0 and w_i are used to distinguished the outer wall thickness from the wall dividing the gas from the steam. The outer wall has thermal losses to the environment (last term). The total thermal resistance, R'_{tot} , is the thermal resistance for conduction across the insulation plus the resistance for convection (see Equation 75). The fourth term in the gas energy equation (Equation 72) represents the heat exchange from the gas to the outer wall.

$$R_{\text{tot}}' = \frac{\ln\left(\frac{D_4 + 2w_{\text{ins}}}{D_4}\right)}{2\pi k_{\text{eff}}} + \frac{1}{2\pi h_{\text{air}}(D_4 2w_{\text{ins}})}$$
Equation 75

The diameters of the heat exchanger reactor are shown in Figure 30; the reactor is 1.2 m long, and the start of the catalyst bed is 0.06 m from the inlet of the reactor.

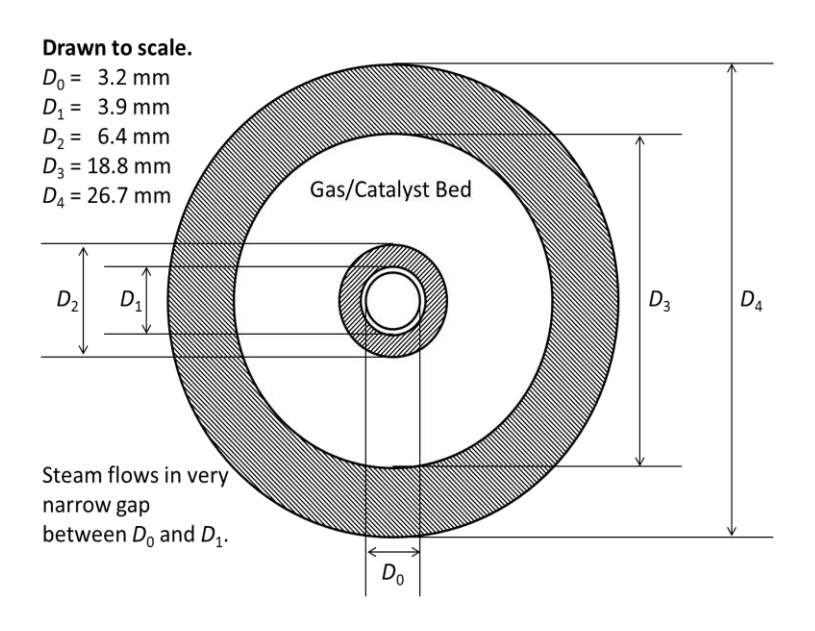


Figure 30 – Reactor heat exchanger cross-sectional geometry

The effective thermal conductivity in the gas/catalyst bed was equal to 5 W/m-K. In the experiment, the gas flow rate was set to 1.01 g/s, and the steam mass flow rate was set to 0.51 g/s. The inlet gas temperature was adjusted to 615 °C, and the steam inlet temperature was adjusted to 350°C (nominally). The gas temperature is measured by thermocouples placed on the outer wall, and the steam temperature is measured along the inner tube (D_0). The insulation thickness is $w_{ins} = 0.235$ m. The catalyst bed starts 0.06 m from the inlet of reactor (x = 0 m). In the numerical model, the same conditions from the experiment were set. A constant outer wall surface convection coefficient of 5 W/m²-K was used. A well-insulated section with no catalyst was added to the model. The reaction starts at x = 0.06 m from the inlet of the reactor (x = 0 m).

The temperature of the gas temperature (red continuous line), inner wall (green continuous line), outer wall (purple dashed line), and steam temperature (blue line) from the numerical model are presented in. The experimental gas (red square markers) and steam (blue square markers) temperature are also presented in Figure 31. The model is able to predict the temperature of the steam. The model is able to predict the gas temperature from x = 0 m - 0.6 m. The discrepancy

between the numerical and experimental gas temperature for x > 0.6 m is due to the assumption of a constant outer wall surface heat transfer coefficient.

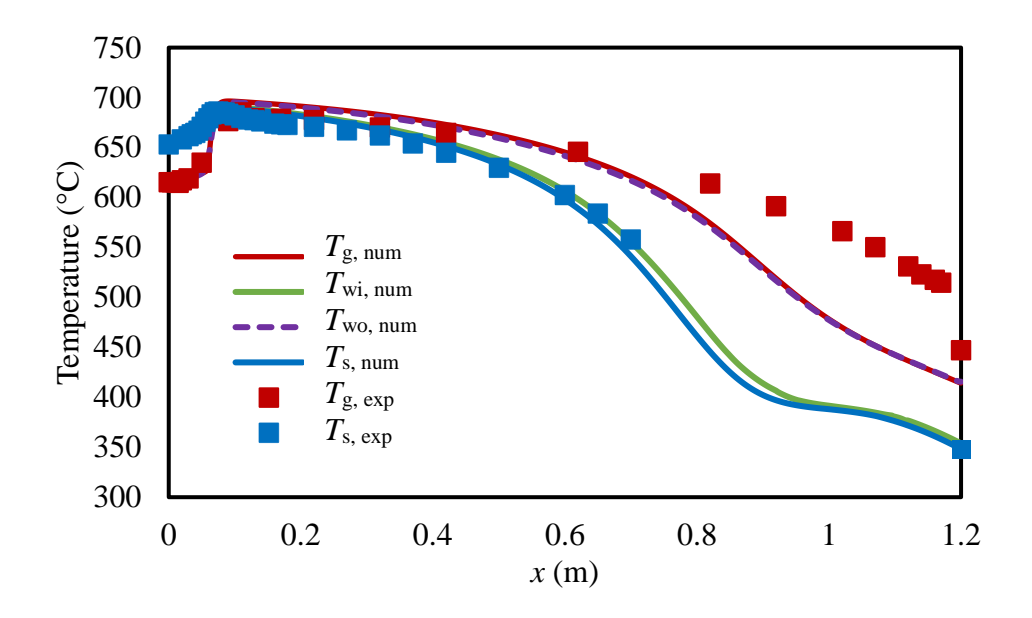


Figure 31 – Comparison between numerical results and experimental results for an ammonia based reactor heat exchanger. Numerical results: gas temperature (red continuous line), inner wall (green continuous line), outer wall (purple dashed line), and steam temperature (blue line). Experimental results: gas temperature (red square markers), and steam temperature (blue square markers).

Exploration of transient behavior of a complex counter-flow heat exchanger

Three different cases that cause different transient behaviors in the system were investigated. Case one will be referred to as the start-up of the system. It consists of a system that is initially (t = 0 s) at uniform temperature, and at t > 0 s, a temperature and ammonia mass fraction step change is imposed on the flow that contains the catalyst. Case two is when the system in case one has reached the new steady state, another *step change in the inlet temperature* is imposed. Case three is when the system in case one has reached steady state, a *step change in the mass flow rate* is imposed.

Case 1: Start-up of the system – Inlet Gas Temperature

The gas, the steam, and the wall are assumed to be at an initial temperature of 288 °C. Initially, the gas in the annulus is at chemical equilibrium with an ammonia mass fraction of 0.215. The inlet temperature of the gas experiences a step change in temperature from 288 °C to 600 °C for t > 0. Also, an ammonia mass fraction of 0.001 is imposed at the inlet of the gas stream.

Figure 32 shows the mass fraction of the ammonia along the reactor for different time steps. The mass fraction experiences a step change at the inlet from 0.215 to 0.001 as shown in Figure 32. This is the step change specified by Equation 61. Figure 33 shows the mass fraction as a function of time for different positions along the reactor. At very early times, the step change in the mass fraction and temperature at the inlet have not propagated along the reactor. This can be seen in Figure 33; for x > 0.5 m, the mass fraction is still at the equilibrium mass fraction, so no reaction has happened yet.

The temperature profiles of the gas, the wall, and the steam along the reactor heat exchanger for different time steps are shown in Figure 34, Figure 35, and Figure 36, respectively. At t = 0 seconds, the gas temperature is at 288 °C everywhere (Figure 34). For t > 0, the inlet gas temperature experiences a step change to 600 °C and stays constant as indicated by Equation 66. The step change in the inlet temperature and mass fraction disturbs the equilibrium state resulting in ammonia synthesis. An increase in the ammonia mass fraction from 0.001 to 0.11 can be observed in Figure 32. A rapid increase is observed very close to the inlet due to the ammonia synthesis reaction as shown in Figure 32. At very early times (t = 100 s), the chemical equilibrium has not been disrupted at locations far from the inlet. The ammonia mass fraction at x > 0.8 m is still at equilibrium. For example, at x = 1.2 m, it takes approximately 200 s for a significant change to occur in the mass fraction as shown in Figure 33. Once the perturbations at the inlet have

propagated, three types of behavior are observed. For locations near the inlet (e.g. x = 0.1 m), the ammonia mass fraction decreases due to the influence of the incoming gas. For points further downstream (e.g. x = 0.25 to 0.9 m), the ammonia mass fraction at first increases due to the ammonia synthesis reaction and subsequently decreases because of the incoming gas. For points downstream (e.g. x = 1.2 m) the ammonia mass fraction increases and reaches an elevated steady-state value. The effect the reaction has on the gas temperature can be observed in Figure 34. Close to the inlet (x = 0.1 m - 0.5 m), the temperature increases to temperatures higher than the inlet temperature of the gas. For example, the temperature at x = 0.1 m reaches 95 °C higher than the inlet temperature. This is due to the exothermic chemical reaction occurring inside of the catalyst bed. The gas temperature along the reactor decreases as shown in Figure 34. The decrease in gas temperature along the reactor is due to the heat transfer to the steam.

The steam temperature along the reactor for different time steps is shown in Figure 36. The steam enters the inner tube of the reactor at x = 1.2 m at a temperature of 288 °C. As is flows through the channel, the steam is heated up by the reaction in the catalyst bed. In Figure 36, one can observe a change in the steam temperature behavior when the pseudocritical temperature is reached.

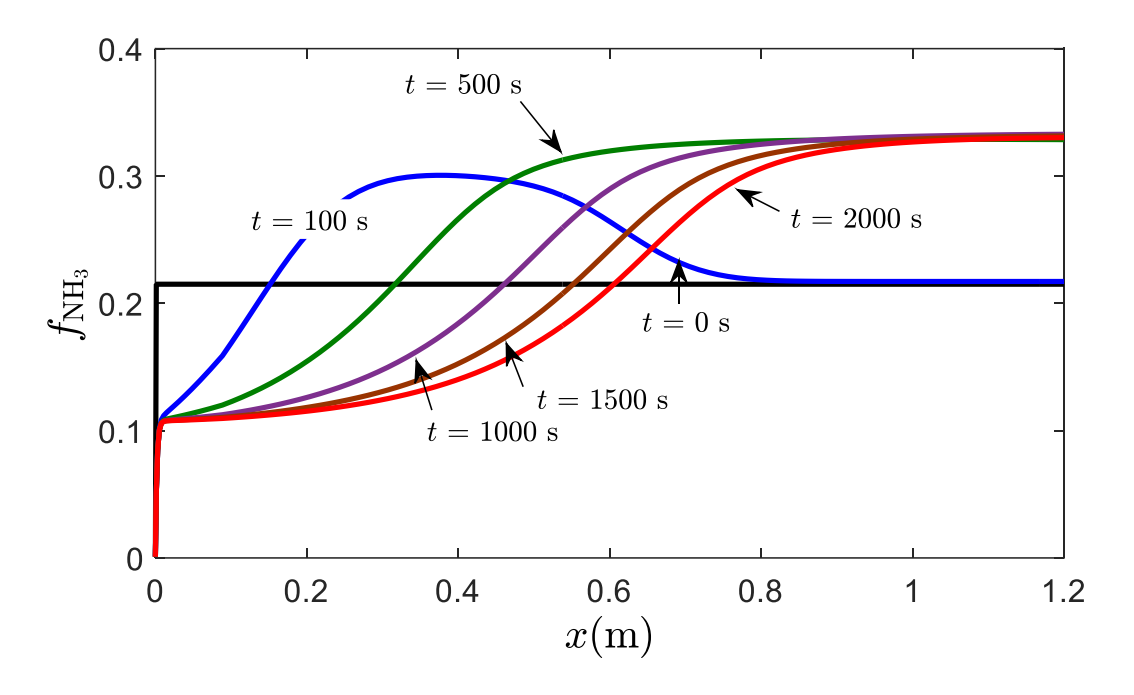


Figure 32 – Mass fraction of ammonia as a function of position for different time steps.

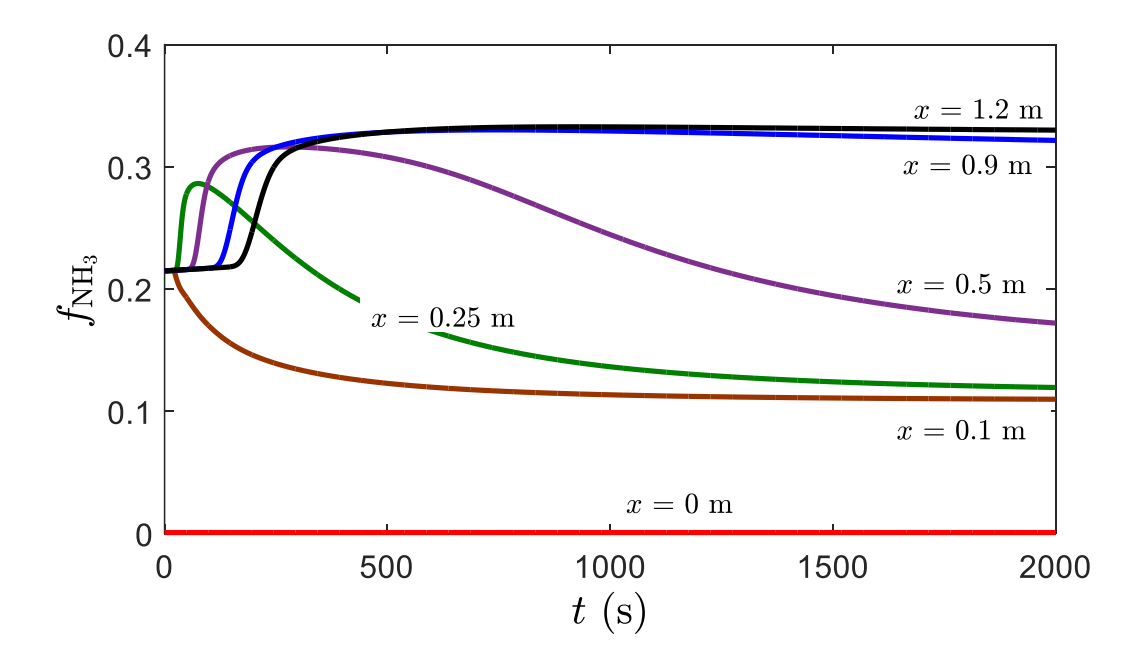


Figure 33 – Mass fraction of ammonia as a function of time for different locations inside the reactor.

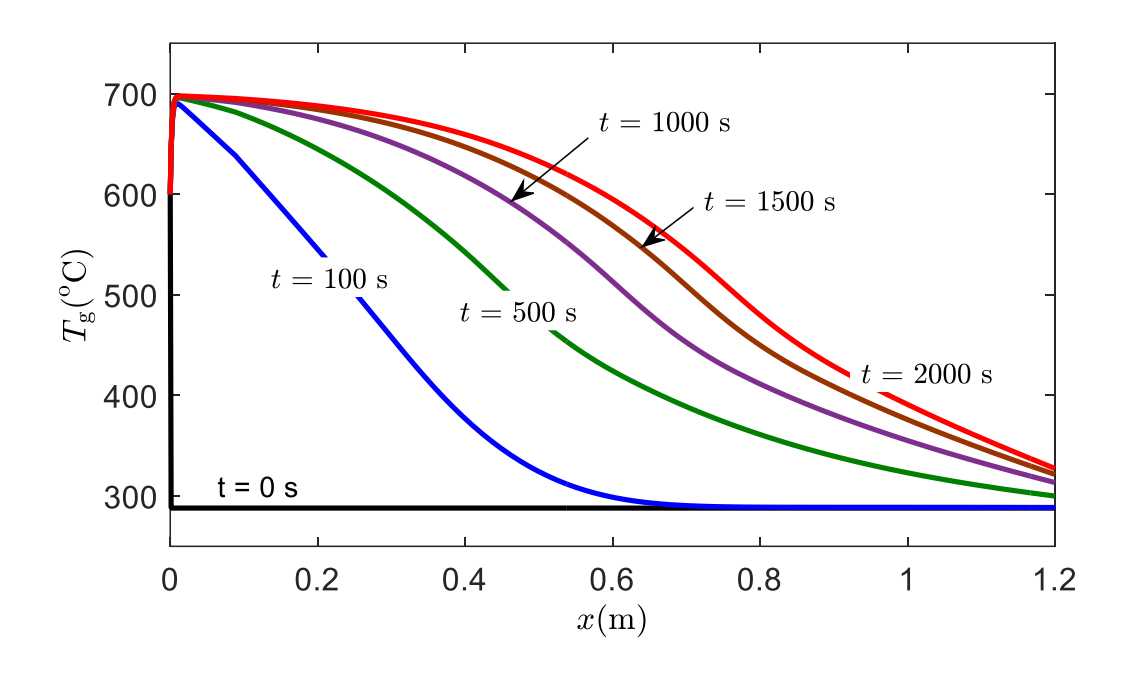


Figure 34 – Gas temperature as a function of position for different time steps.

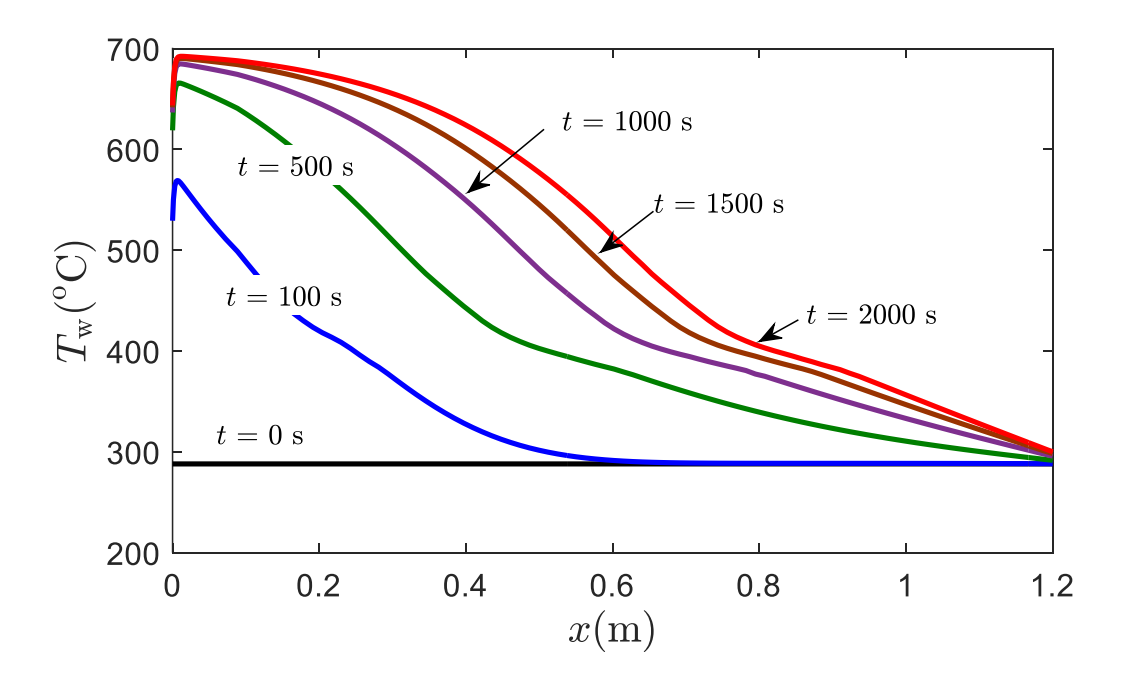


Figure 35 – Wall temperature as a function of position for different time steps.

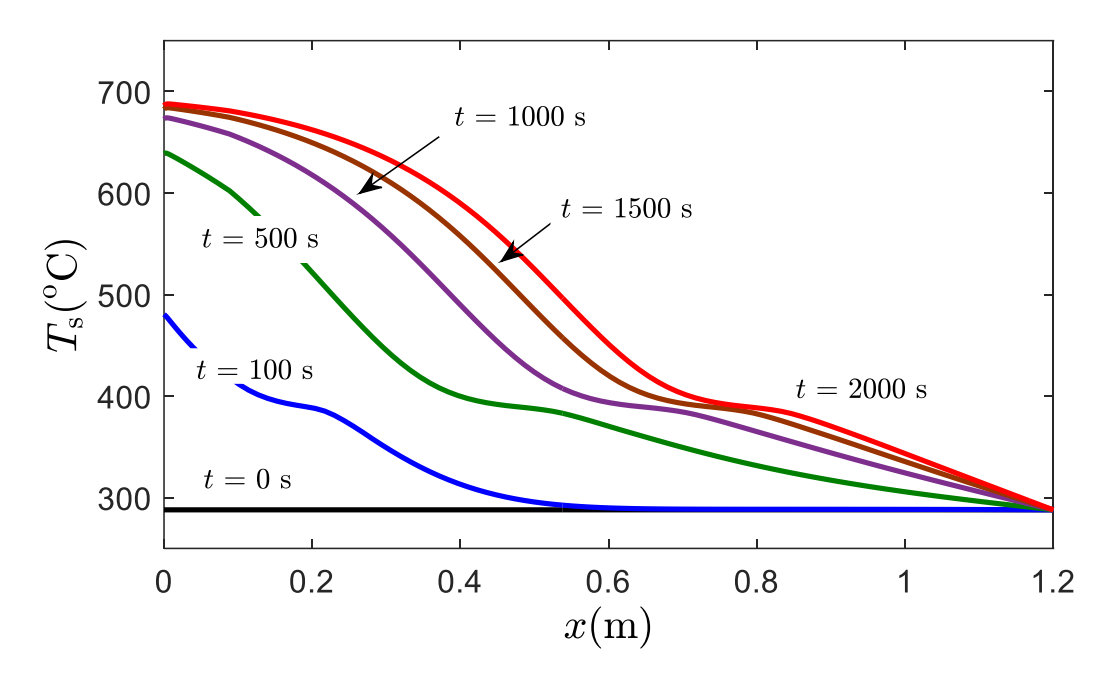


Figure 36 – Steam temperature as a function of position for different time steps.

It is important to know how fast the steam outlet temperature reaches steady state, and if at steady state, the steam outlet temperature has reached the target temperature of 650 °C. The outlet mass fraction reaches steady state in approximately 13 minutes. The gas and steam outlet temperatures reach steady state in 10 minutes and 7 minutes, respectively. The steady state results are shown in Figure 37. The gas temperature enters the channel at 600 °C. The reaction starts immediately after the gas enters the catalyst bed, causing the gas temperature to reach a maximum of 695 °C in a very short distance. Thereafter, the gas temperature starts decreasing due to the heat transfer to the wall and then to the steam. The steam enters the inner tube at 288 °C, and exits at 692 °C. It is important to note that the desired outlet steam temperature of 650 °C was exceeded for the parameters selected in this example. By overdesigning, the system can reach 650 °C steam temperature earlier than the steady-state is reached.

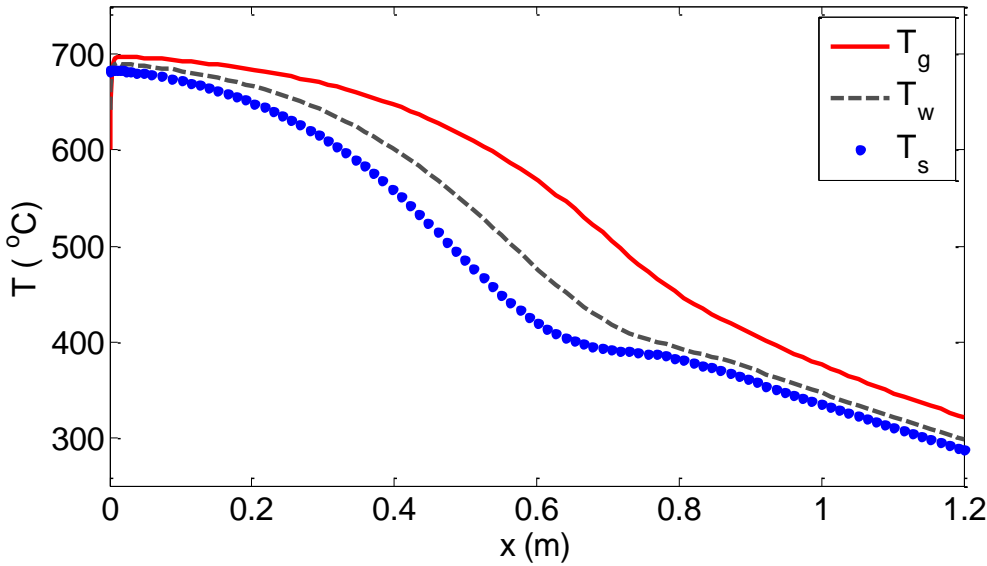


Figure 37 – Steady state temperature profiles of the gas, the steam, and the wall as a function of axial position for a gas mass flow rate of 0.1 g/s and a steam mass flow rate of 0.08 g/s.

It is of special interest to investigate the effect the gas mass flow rate has on the time the outlet steam temperature takes to reach steady state. All the parameters specified above were kept constant except for the gas mass flow rate. The gas mass flow rate was varied between 0.01 g/s and 1 g/s. The results are presented for different initial gas temperatures ranging from the inlet steam temperature (288 °C) to the inlet gas temperature (600 °C).

Figure 38 shows the time the outlet steam temperature takes to reach steady state (left axis) as a function of gas mass flow rate for the different initial conditions. The time the steam outlet temperature takes to reach steady state decreases as the gas mass flow rate increases. For gas mass flow rates greater than 0.2 g/s, the time t_{st} is almost constant. However, for gas mass flow rates smaller than 0.2 g/s, the time increases rapidly with increasing flow rate. It can also be observed that the initial gas temperature has negligible effect on t_{st} for gas mass flow rates greater than 0.2 g/s. For gas mass flow rates lower than 0.2 g/s, the initial gas temperature has an effect on t_{st} ; for lower initial gas temperature, t_{st} is higher.

Figure 38 also shows the outlet steam temperature (continuous red line) as a function of gas mass flow rate. The target outlet steam temperature (dotted red line) was included in Figure 38 as a reference. It is important to remember that the steady state outlet steam temperature is independent of the initial conditions of the system. The target outlet steam temperature is met for gas mass flow rates greater than 0.1 g/s. The reactor heat exchanger has a similar behavior as a regular heat exchanger. If it is assumed that the gas has an effective heat capacity rate that is augmented by the reaction, one can explain why the target outlet steam temperature is not achieved for low gas mass flow rates. For small gas mass flow rate, the gas effective heat capacity rate is smaller than the steam heat capacity rate, so its outlet temperature can approach the steam inlet temperature if the heat exchanger is long enough. Under these conditions, the steam outlet temperature depends on the ratio of the flow rates. However, for gas mass flow rates greater than 0.1 g/s, the steam heat capacity rate is lower than the effective heat capacity rate of the gas, so the steam outlet temperature approaches the gas inlet temperature.

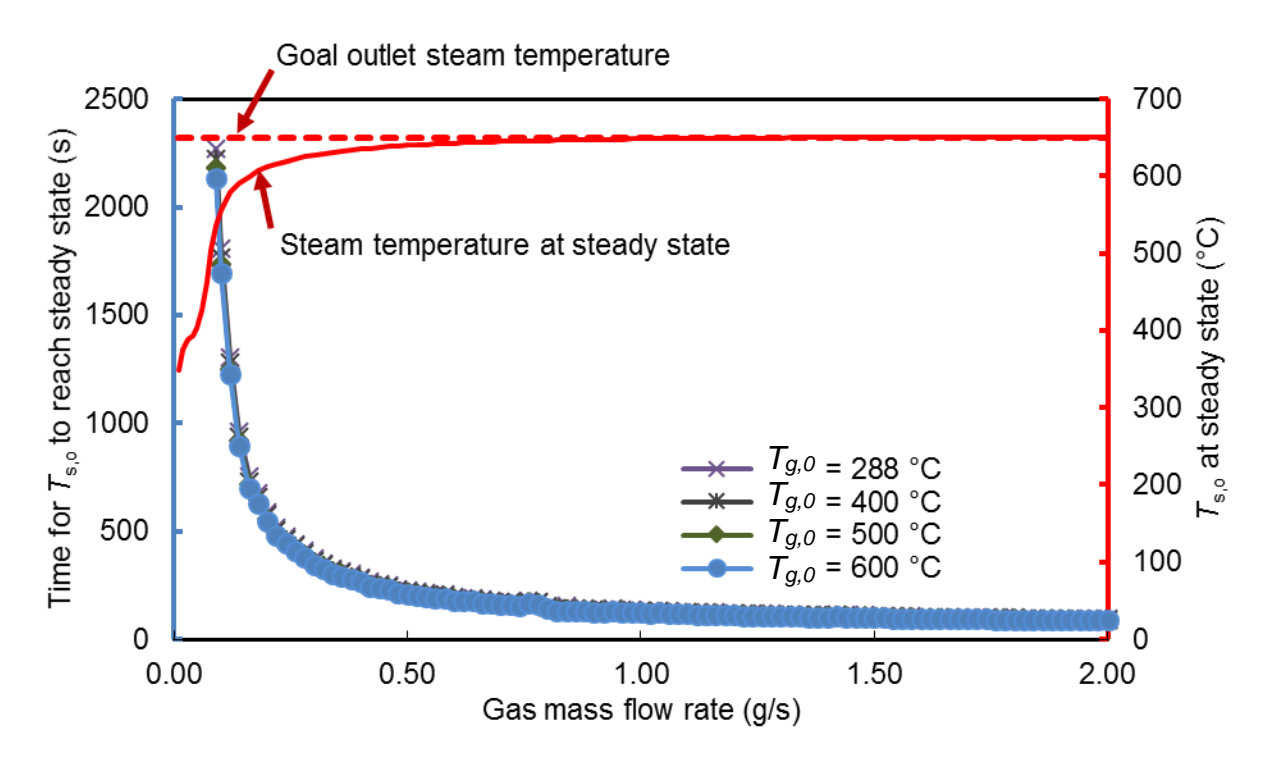


Figure 38 – Left axis: Time the outlet steam temperature takes to reach steady state (blue axis) as a function of gas mass flow rate for different initial gas temperatures. Right axis: Outlet steam temperature (red axis) as a function of gas mass flow rate. Continuous red line is outlet steam temperature from simulation, and dashed red line is the goal outlet steam temperature needed for steam turbine.

Summary

The numerical model predicts the transient behavior of a one dimensional concentric tube counter-flow reactor heat exchanger. Results show that it is possible to use ammonia synthesis reaction to heat supercritical steam to temperatures on the order of 650 °C as required for a supercritical steam Rankine cycle. It was also shown that high gas mass flow rates are preferred for both reaching the desired steam outlet temperature of 650 °C and reaching steady state in a reasonable time. The model is a tool that can be used to design an ammonia synthesis reactor heat exchanger that can achieve a steam temperature of 650 °C earlier than the steady-state is reached.

Case 2: Inlet Gas Temperature Disturbance

In this section, the response to a step change in the inlet temperature of a system shown in Figure 37 will be investigated. The same dimensionless parameters described previously were used. The gas inlet temperature was changed from $T_g(x, t = 0) = 600$ °C to $T_g(x, t > 0) = 512$ °C. The temperature at the gas inlet was decreased by 15%. All of the other conditions remained the same: the steam inlet temperature is 288 °C, the steam mass flow rate is 0.08 g/s, and the gas mass flow rate is 0.1 g/s. Figure 39 shows the effect of a disturbance in the inlet gas temperature on a steady state system. The system at t = 0 s is at steady state (dashed lines). The red-dashed line represents the steady state gas temperature profile at t = 0 s. The green-dashed line represents the steady state wall temperature profile at t = 0 s. The blue-dashed line represents the steady state steam temperature profile at t = 0 s. At $t = 0^+$ s, the temperature at the inlet of the hot fluid is decreased to $T_g(x, t > 0 \text{ s}) = 512 \,^{\circ}\text{C}$ as shown in Figure 39. The "new" steady state solution is also shown in Figure 39 (continuous lines). With an inlet gas temperature of 600 °C, the reaction heat generation heats the gas to 698.4 °C. With an inlet gas temperature of 512 °C, the gas temperature increases to 646.7°C. Even though the inlet gas temperature decreased by 88 °C, the maximum gas temperature only decreased by 51.7 °C. The heat of reaction is able to maintain a higher gas temperature. This is also reflected in the steam temperature; the steam outlet temperature drops from 619.8 °C to 585.7°C. With the decrease in the inlet gas temperature, the heat exchange between the gas and the wall (and then the steam) decrease, so the outlet gas and wall temperatures decrease by only 1 °C.

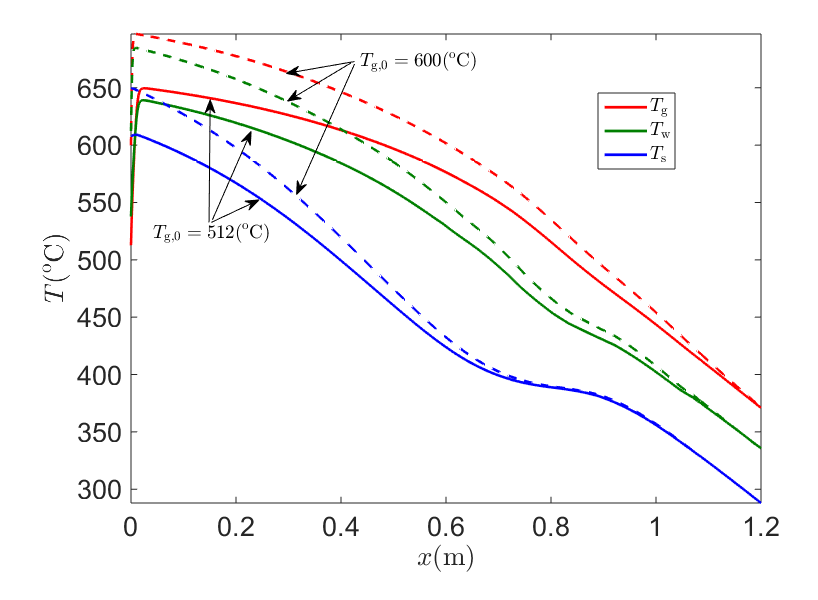


Figure 39 – Steady state temperature of the gas (red), the wall (green), and the steam (blue) of ammonia synthesis reactor heat exchanger as a function of position. Dashed line: Steady state solution for a system with a gas inlet temperature of 600 °C. Continuous line: Steady state solution after step change in gas inlet temperature from 600 °C to 512 °C.

Figure 40 shows the transient behavior after a step change in the inlet gas temperature of a steady state system. The step change does not have a big impact on the system as seen before for a heat exchanger without reaction (Figure 14). The reaction predominates in the system maintaining a high temperature along the reactor. Figure 40a shows the change in the ammonia mass fraction across the reactor as time increases. The shape of the ammonia mass fraction profile along the reactor changes with time; however, the outlet ammonia mass fraction decreases from 0.57 to 0.36. However, the gas outlet temperature does not change. Figure 40b shows the change in the gas temperature across the reactor as time increases. The temperature drop at the inlet of the reactor can be observed; however, the outlet gas temperature drops by only 1 °C. The heat exchange to the wall has decreased because the temperature difference between the wall and the gas is smaller causing the gas to exchange less heat. Figure 40c shows the change in the wall temperature as a function of position for different time steps across the reactor as time increases.

The wall temperature profiles show the same behavior as the gas. Figure 40d shows the change in the steam temperature across the reactor as time increases. The steam outlet temperature decreases as a result of the temperature drop at the inlet of the gas. However, the temperature drop is minimal compared to the gas temperature drop.

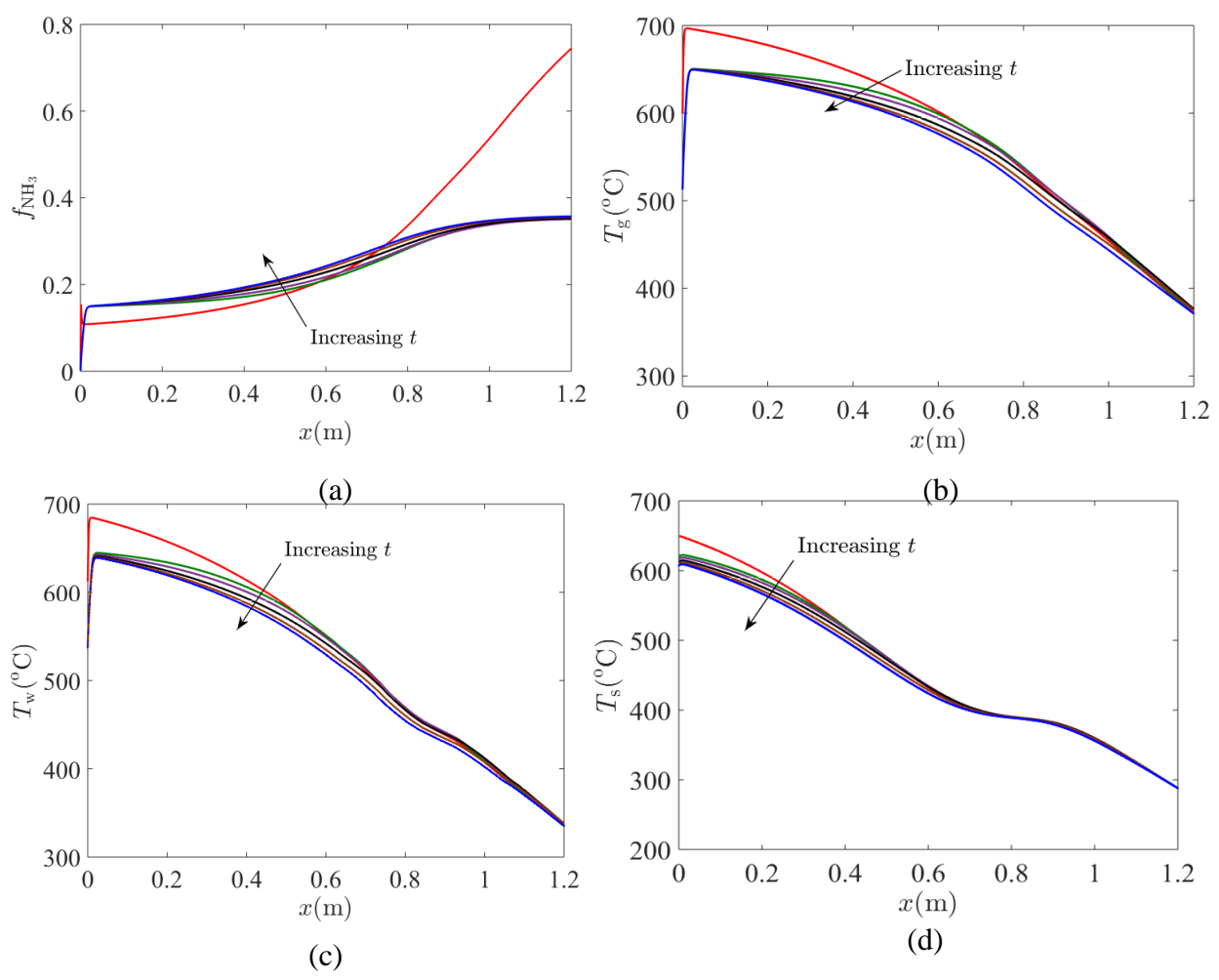


Figure 40 – Transient behavior after a step change in the inlet gas temperature of a steady state system. (a) Ammonia mass fraction, (b) gas temperature, (c) steam temperature, and (d) wall temperature as a function of position for different time steps.

Summary

If the inlet temperature of the gas suffers a step change, the maximum gas temperature is

also decreased. The gas temperature drop also affects the steam outlet temperature.

Case 3: Inlet Gas Mass Flow Rate Disturbance

It is also of interest to investigate the effect a change in gas mass flow rate has on the system at steady state. The steady state system shown in Figure 37 is disrupted by a step change in the gas mass flow rate. The gas mass flow rate was changed from $\dot{m}_h = 0.1 \, \mathrm{g/s}$ to $\dot{m}_h = 0.075 \, \mathrm{g/s}$ at t > 0 s. All of the other conditions stay the same: the steam inlet temperature is 288 °C, the steam mass flow rate is 0.08 g/s.

Figure 41 shows the effect the disturbance in the gas mass flow rate has on a steady state system. The system at t = 0 s has a gas mass flow rate of $\dot{m}_h = 0.1\,\mathrm{g/s}$ (dashed lines). The reddashed line represents the steady state gas temperature profile at t = 0 s. The green-dashed line represents the steady state wall temperature profile at t = 0 s. The blue-dashed line represents the steady state steam temperature profile at t = 0 s. At t > 0 s, the gas mass flow rate is decreased causing a change in the slope of the temperature profiles as shown in Figure 41. The "new" steady state solution is also shown in Figure 41 (continuous lines). The system takes 37.1 seconds to reach steady state.

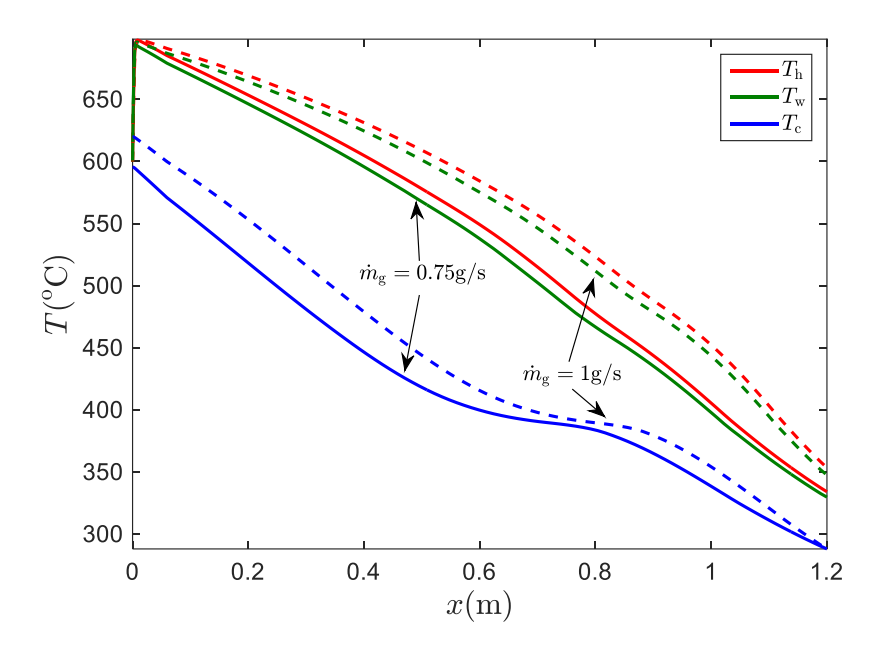


Figure 41 – Steady state temperature of the gas (red), the wall (green), and the steam (blue) of ammonia synthesis reactor heat exchanger as a function of position. Dashed line: Steady state solution for a system with a gas mass flow rate of 0.1 g/s. Continuous line: Steady state solution after step change in gas mass flow rate to 0.075 g/s.

Figure 42 shows the transient behavior after a step change in the gas mass flow rate of a steady state system. The step change does not have a big impact on the system as seen before for a heat exchanger without reaction (Figure 14). The reaction predominates in the system maintaining a high temperature along the reactor. Figure 42a shows the change in the ammonia mass fraction across the reactor as time increases. Figure 42b shows the change in the gas temperature across the reactor as time increases. Figure 42c shows the change in the steam temperature across the reactor as time increases. Figure 42d shows the change in the wall temperature as a function of position for different time steps across the reactor as time increases.

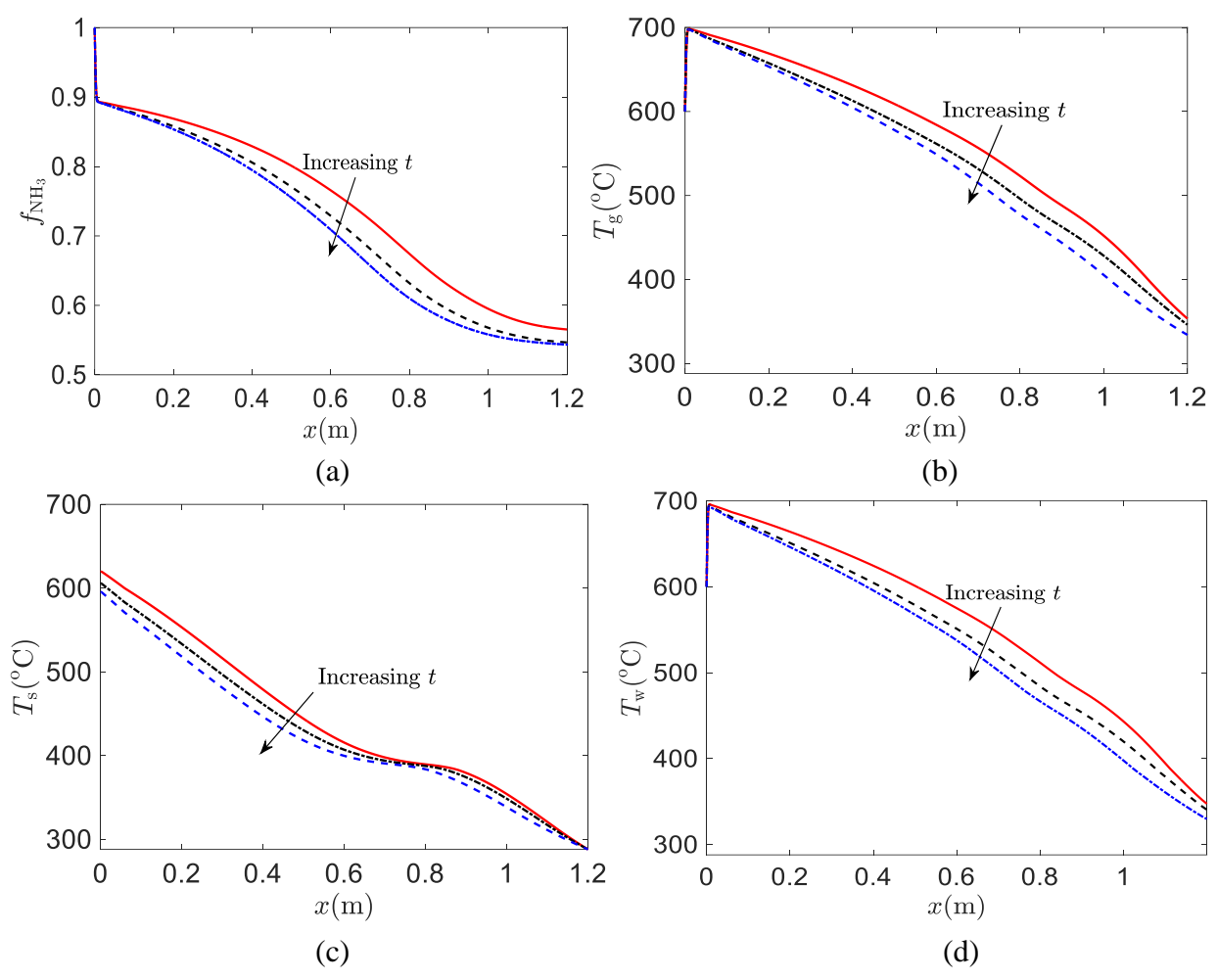


Figure 42 – Transient behavior after step change in gas mass flow rate from 0.1 g/s to 0.075 g/s. (a) Ammonia mass fraction, (b) gas temperature, (c) steam temperature, and (d) wall temperature as a function of position for different time steps.

Summary

A small perturbation in the gas mass flow rate has an effect on the profile shape. However, the maximum temperature reached in the gas due to reaction is not affected. The reaction is able to maintain the gas maximum temperature. The main effect can be observed on the shape of the gas temperature profile. The heat exchange from the gas to the wall is affected and this is reflected in the gas temperature profile. Slight perturbations in the gas mass flow rate should not be a concern for the final behavior of the system. However, if the disturbance is relatively large then

the effect on the heat transfer in the system could result in low performance.

Effect of Axial Conduction

Axial conduction in the reactor-heat-exchanger was investigated, specifically in the gas section. Most of the analysis of heat exchangers assumes axial conduction is negligible which is generally a good assumption. However, this assumption may not be valid for the reactor-heat-exchanger because of the iron-based catalytic bed and thick walls needed to withstand the high pressure. In this current effort, the effect of axial conduction was investigated. Once the phenomenon is well understood, the conditions under which axial conduction can be neglected will be determined.

In the investigation of axial conduction reported here, the model has been run to steady-state. The conditions of an existing reactor were used except that the length was shortened to speed run times. Specifically, the gas flows in an Inconel tube with inner diameter of 1.88 cm and length of 0.6 m. Steam flows through an inner tube of 0.39 cm ID and 0.64 cm OD as shown in Figure 27. The gas and the steam had mass flow rates of 0.1 g/s and 0.08 g/s, respectively.

In pipe flow analysis, it is usually assumed that axial conduction is negligible. However, axial heat conduction in the catalyst bed occurs within the iron based catalysts, which has the effect of increasing the effective thermal conductivity of the gas-catalyst system. A parametric study was performed to determine the effect axial conduction has in the system. The gas Peclet number was used to determine the conditions where axial conduction can be neglected. The gas Peclet number is defined as:

$$Pe_{g,in} = \left(\frac{\rho c_p u D_h}{k}\right)_{g,in}$$

The model was run for a range of $k_{\text{eff}} = 0 - 50 \text{ W/m-K}$. The thermal conductivity of iron at

high temperatures (600 °C – 700 °C) is $k_{\rm FE} \sim 50$ W/m-K, and typical porosities in the catalyst are on the order of 50%. For this study, the wall axial conduction was neglected.

Figure 43 shows the gas temperature (a), wall temperature (b), and steam temperature (c). It can be seen that as thermal conductivity increases, the maximum gas temperature decreases and the location of the maximum gas temperature also shifts downstream. The maximum temperature due to the reaction happens very close to the inlet of the reactor. There is a rapid temperature change right after the inlet of the channel. This causes a high heat loss through the inlet end of the reactor due to axial conduction which results in a decrease of the maximum gas temperature and consequently a decrease of the outlet steam temperature.

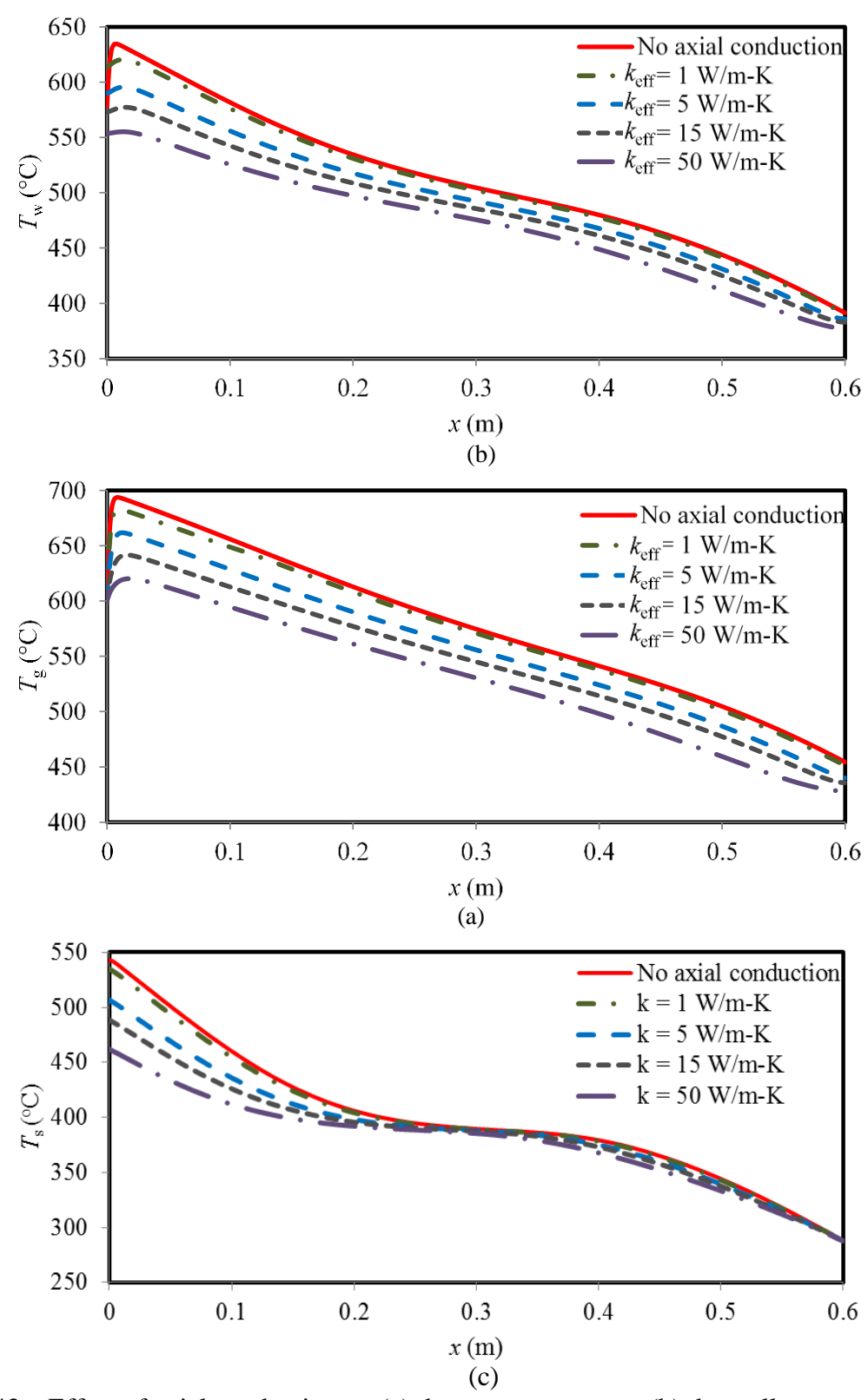


Figure 43 – Effect of axial conduction on (a) the gas temperature, (b) the wall temperature, and the (c) steam temperature.

When axial conduction in the gas and steam is neglected, a maximum gas temperature of 693°C is achieved resulting in an outlet steam temperature of 541°C as shown in Figure 44a. Next, the same conditions were run, but axial conduction was included. The Peclet number for the given parameters is approximately 18 – based on an effective thermal conductivity of 50 W/m²-K. Referring to Figure 44b, the maximum gas temperature dropped to 632°C, which is 61°C lower than the case with no axial conduction. Some rounding can also be observed in the shape of the peak gas temperature, but this is a small effect. The outlet steam temperature dropped to 466 °C, or 75 °C lower than the case with no axial conduction. For this case, axial conduction is important, and it has a negative effect on the desired outlet steam temperature.

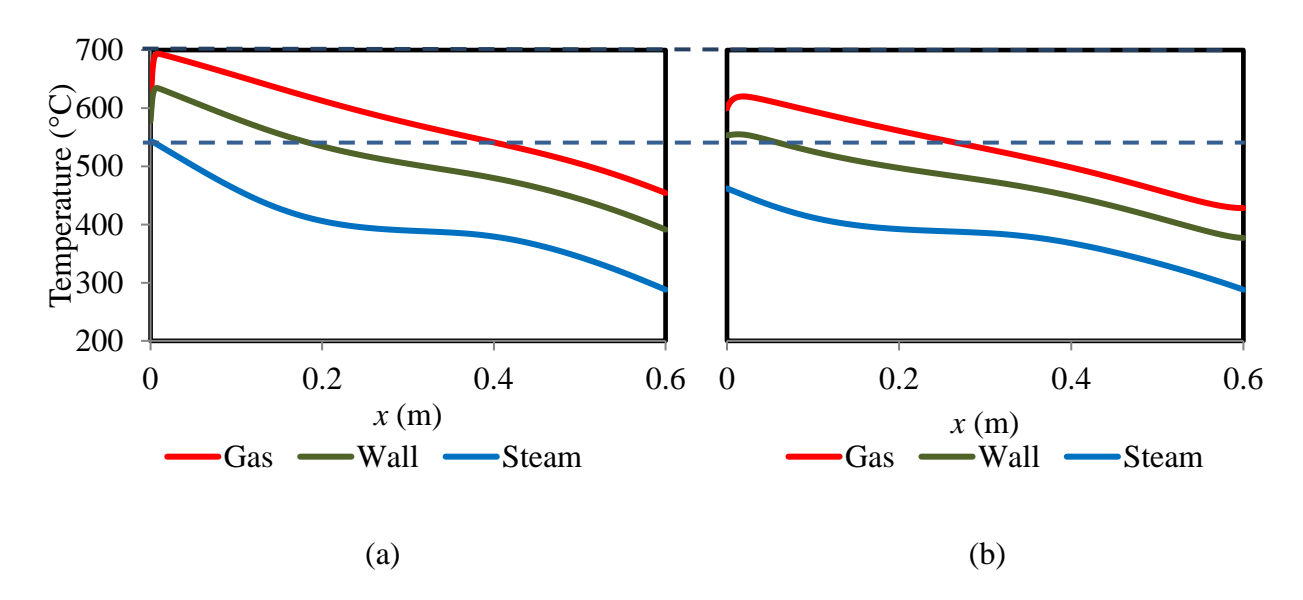


Figure 44 – Steady state temperature profiles for the gas (red), wall (green), and steam (blue) for (a) no axial conduction and for (b) axial conduction ($Pe_g = 18$).

It is of interest to find the conditions under which axial conduction is the gas/catalyst bed can be neglected. For this purpose, a non-dimensional analysis was performed. The gas Peclet number was varied between 0.4 and 400, while the rest of the parameters were kept constant. The

dimensionless maximum temperature was defined as follows:

$$heta_{ ext{max}} = rac{\left(T_{r, ext{max}} - T_{r, ext{in}}
ight)}{\left(T_{r, ext{max}_{- ext{na}}} - T_{r, ext{in}}
ight)} \qquad r = ext{gas or steam}$$

where $T_{r,\text{max}}$ is the maximum temperature of r, $T_{r,\text{in}}$ is the inlet temperature of r, and $T_{r,\text{max_na}}$ is the maximum temperature of r for the case of no axial conduction.

Figure 45 shows the effect Pe_g has on the maximum temperature of the gas and steam streams. Choosing a criterion of a 2% change in the maximum temperature, it was found that axial conduction can be neglected for $Pe_g > 100$.

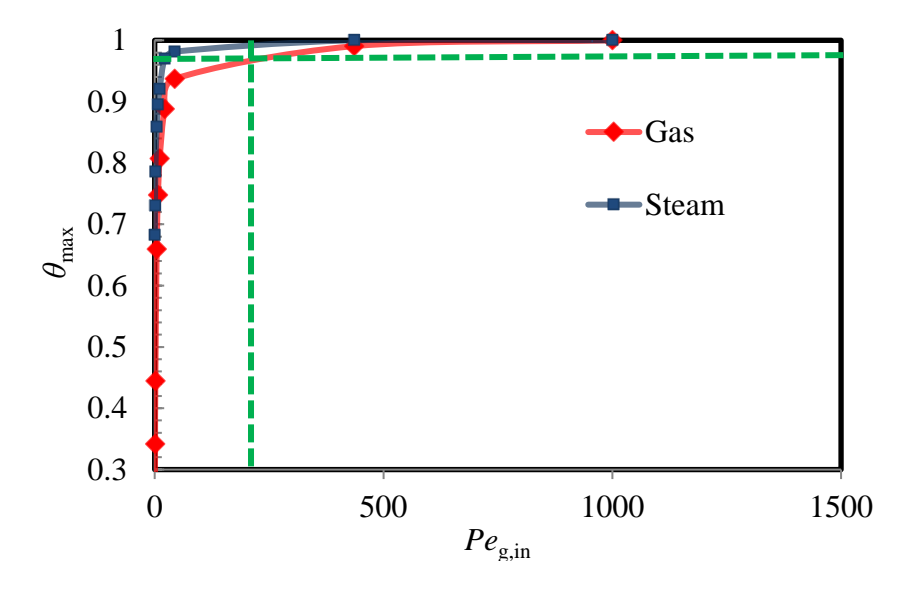


Figure 45 – Maximum dimensionless temperature of gas (red) and steam (blue) as a function of gas Peclet number for an ammonia synthesis reactor heat exchanger.

Well-insulated Non-reacting Section

The model was modified to simulate a well-insulated non-reacting section before the catalyst bed. The non-reacting section added at the entrance of the gas is shown in Figure 46. There is no heat transfer from the non-reacting section to the steam. The numerical model can easily be

modified to obtain results for this type of reactor. Heat generation and heat transfer from the wall to the cold fluid are "turned off" for the upstream section. Figure 46 shows the dimensions used in the simulations. The total reactor length is still 1.2 m, but now the catalytic bed starts at x = 0.3 m, and there is heat transfer between the wall and the steam only after x = 0.3 m.

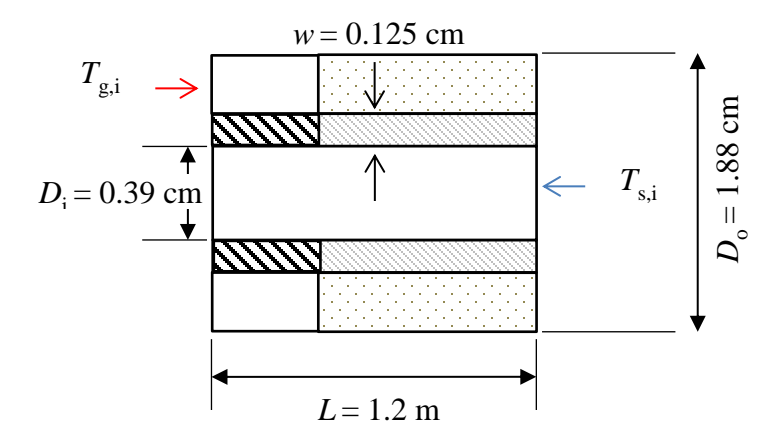


Figure 46 – Schematic of an ammonia synthesis reactor heat exchanger with a non-reacting section at the beginning of the reactor.

Figure 47 shows the steady state temperature of the gas, the wall, and the steam as a function of position when axial conduction is neglected. If axial conduction is negligible in the system, having a non-reaction section makes no difference. However, for systems in which axial conduction is important, a non-reacting section will help the system maintain the maximum temperature achieved due to the reaction.

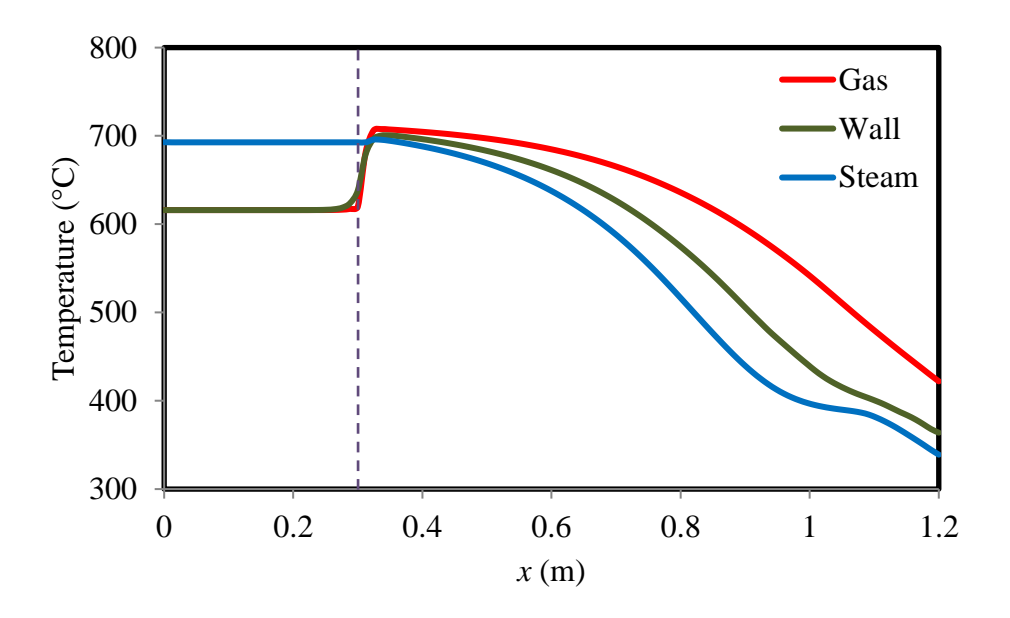


Figure 47 – Steady state solution for a reactor heat exchanger with a non-reacting section length of $x_{\rm uh} = 0.3$ m, with a gas mass flow rate of $\dot{m}_{\rm g} = 0.1\,{\rm g/s}$ for steam flow rate of $\dot{m}_{\rm g} = 0.08\,{\rm g/s}$.

Axial conduction was neglected.

Figure 48 shows the temperature of the gas, the wall, and the steam as a function of position for different effective thermal conductivities. Figure 48a shows that even for the highest thermal conductivity, the maximum temperature is maintained as compared to a reactor without a non-reacting section (Figure 43a). The outlet steam temperature is not affected by axial conduction as shown in Figure 48b. This is because the non-reacting section allows an energy recovery mechanism. If the section is long enough and well-insulated, the drastic change in temperature is avoided, making axial conduction at the inlet negligible.

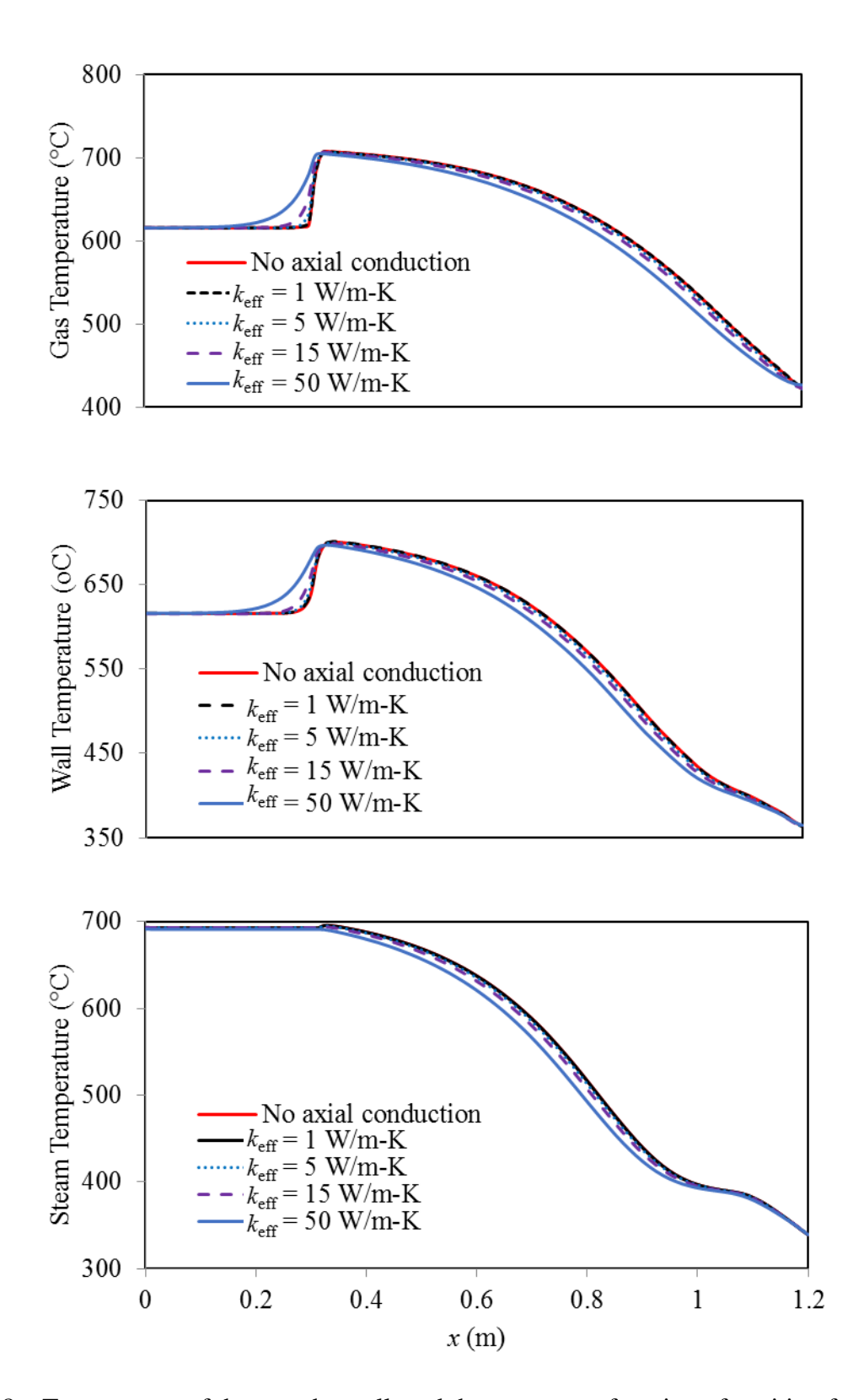


Figure 48 – Temperature of the gas, the wall, and the steam as a function of position for different effective thermal conductivities.

Effect of Gas Peclet Number

It is of interest to ensure that the non-reaction section is an effective solution for different conditions. For this purpose, a nondimensional analysis was performed. The gas Peclet number was varied between 0.4 and 50, while the rest of the parameters were kept constant. Figure 49 shows the effect Pe_g has on the maximum temperature of the gas and steam streams for a reactor heat exchanger with a non-reacting section. Choosing a criterion of a 2% change in the maximum temperature, it was found that axial conduction can be neglected for $Pe_g > 1$ when there is a non-reacting section.

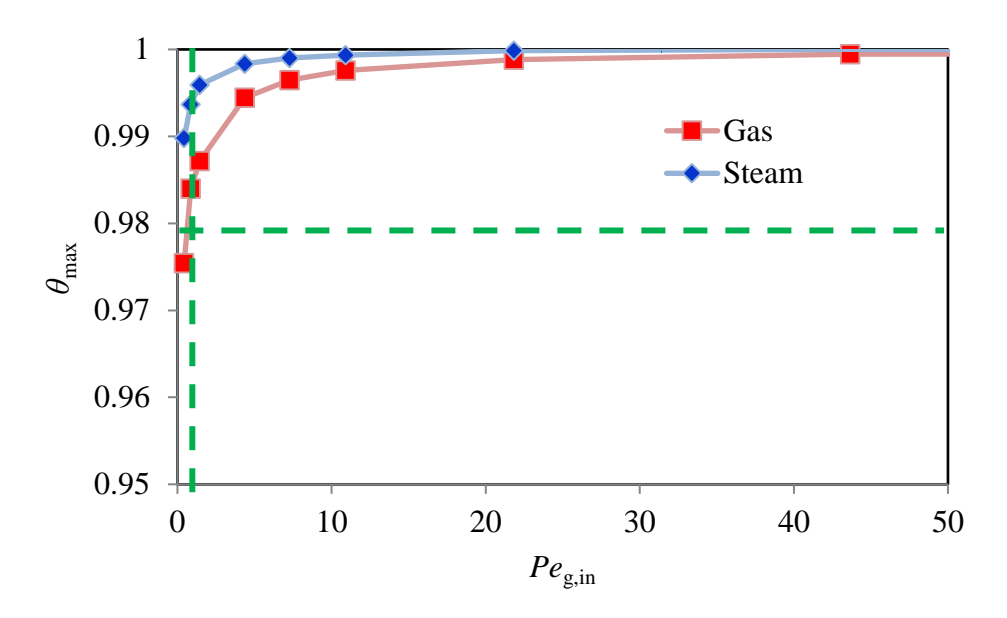


Figure 49 – Maximum dimensionless temperature of gas (red) and steam (blue) as a function of gas Peclet number for an ammonia synthesis reactor heat exchanger with a non-reaction section.

Summary

Results show that by having a non-reacting well-insulated section, axial conduction becomes unimportant. This is because the non-reacting section allows an energy recovery mechanism. If the section is long enough and well-insulated, the drastic change in temperature is

avoided, making axial conduction at the inlet negligible. From this section, an easy solution was given to deal with axial conduction in the system.

CHAPTER 5: Concluding Remarks and Future Research

Concluding Remarks

From the results gathered in Chapter 2, 3, and 4, it is evident that there was a need for a more comprehensive study on the transient behavior of heat exchangers. In Chapter 1, a summary of the available solutions for transient heat exchangers obtained by previous authors was provided. There are three main points that should be taken from this section. First, most of the work done on transient heat exchangers was done when computational power was not readily available (1956 – 1989). Because of this, most of these solutions were obtained analytically for simplified problems. More recent work has been done on transient heat exchangers (2013), but the solutions are for very specific cases. All of the solutions in literature have restrictions, and very specific assumptions. If the transient behavior of a more complex heat exchanger is needed (i.e. heat generation), then the solutions from literature are no longer valid. With the computational resources now available, there was a need to develop a numerical model that relaxes the restrictions of current solutions.

In chapter 2, the numerical model was explained in detail. The numerical model solves for a one dimensional counter-flow heat exchanger. There are no restrictions on the fluids and wall conditions. The model is able to obtain a numerical solution for a wide range of fluid properties and mass flow rates. Another innovative characteristic of the numerical model is that the boundary and initial conditions are not limited to constant values.

In Chapter 3, four different transient cases were explored in this work. The first case showed the start-up of a system that is initially at a uniform temperature. Two different behaviors were observed. One happens very early in time and is dependent on the residence time of the fluid. When a new temperature is applied to one of the channel inlets, the fluid at the new temperature

moves as a wave across the heat exchanger; as time increases the flow with the new temperature displaces the fluid at the initial temperature. Once all the fluid has been displaced, only the linear transient behavior is observed. The slope of this temperature profiles changes with time until the system reaches steady state. This transient is due to the decrease of heat exchange between the hot fluid and the wall. The second case showed what happens if the inlet temperature of a system at steady state is disturbed. The results for this case have a similar behavior to the start-up case. The "wave-like" behavior was observed at early times, and then the linear behavior happens until the system reaches a "new" steady state. For the third case, a disturbance on the mass flow rate was imposed. As expected, only the linear behavior was observed. The fourth case showed the effect of a time varying inlet temperature on one of the flows. The oscillations at the inlet get transmitted along the channel. However, the oscillations get dissipated when the heat exchange happens. The oscillations can barely be observed in the other fluid.

Next, a scaling analysis was performed to determine what influences the time a heat exchanger takes to reach steady state. The scaling analysis resulted in expressions that suggest the dependency of t_{st}^* (time a system takes to reach steady state) on the dimensionless parameters M, C, NTU_h , NTU_c , and C_w . A parametric study was then performed to determine the effect the dimensionless parameters on the time the system takes to reach steady state. The results show that t_{st}^* depends linearly on C, C_w , and M^{-1} . It was also shown that t_{st}^* has a logarithmic dependency on NTU_h and NTU_c . Gathering the information gained from the scaling analysis and the parametric study, a correlation was generated to approximate the time a system takes to reach steady state. This correlation is only valid for systems where $C_w << 1$; in other words, when wall thermal capacity is small compared to the flow thermal capacity. The work described in Chapters 2 and 3 has provided enough information to investigate a more complex system where most of the

restrictions or assumptions can be relaxed.

In Chapter 4, a more complex heat exchanger with a specific application was investigated. It was of special interest to look at a heat exchanger with varying properties, heat generation, varying heat transfer coefficient, and axial conduction. More specifically, a counter-flow heat exchanger with a reacting flow in one of the channels was investigated. The application for this reactor heat exchanger is solar energy storage, and the goal is to heat up steam to 650 °C by using the ammonia synthesis heat of reaction. One of the concerns for this system is the start-up time and also how disturbances in the reacting flow can affect the steam outlet temperature. The same three different cases investigated in chapter 2 (for a simple heat exchanger) were explored for the reactor heat exchanger.

The transient behavior during the system start-up was presented. The "wave-like" behavior was also present for this system. Since there is heat generation within one of the flows and the properties are changing with temperature, there is no longer a linear behavior. However, there is still an increase with time in the gas outlet temperature after the residence time is over. The time the system takes to reach steady state is dependent on the conditions of the system. It was found that for low mass flow rates, the system takes longer to reach steady state. This is because the predominant transient behavior is closely linked to the residence time. If the residence time is lower (by making mass flow rate higher), then the total time for a system to reach steady state decreases. It is important to keep in mind that higher mass flow rates also mean higher pressure drop across the channel. So there needs to be a tradeoff between pressure drop and the time the system should take to reach steady state.

Perturbations on a system at steady state were also investigated. If the inlet temperature of the gas suffers a step change, it affects the reaction rate as well as the outlet steam temperature. However, the system is able to recover and reach a "new" steady state. A small perturbation on the gas mass flow rate has an effect on the profile shape. However, the maximum temperature reached in the gas due to reaction is not affected. The reaction is able to maintain the gas maximum temperature. The main effect can be observed on the shape of the gas temperature profile. The heat transfer from the gas to the wall is affected and this reflects on the gas temperature profile. Slight perturbations in the gas mass flow rate should not be a concern on the final behavior of the system. However, if the disturbance is relatively large then the effect on the heat transfer in the system could result in low performance.

Finally, axial conduction in the reactor heat exchanger was investigated, specifically in the gas section. Most of the analysis on heat exchangers assumes axial conduction is negligible which is generally a good assumption. However, this assumption may not be valid for the reactor heat exchanger because of the iron-based catalytic bed. Results in this section show that axial conduction is detrimental for the system. The maximum temperature due to the reaction happens very close to the inlet of the reactor. There is a rapid temperature change right after the inlet of the channel. This causes a high heat loss through the end of the reactor due to axial conduction which results in a decrease of the maximum gas temperature and consequently a decrease of the outlet steam temperature. A parametric study was performed to determine when axial conduction can be neglected. It was concluded that for Peclet number greater than 100, axial conduction can be neglected. There was an alternative solution to deal with axial conduction in the system, this was to have a non-reacting section without a catalytic bed.

Results show that by having a non-reacting well-insulated section, axial conduction becomes unimportant. This is because the non-reacting section allows an energy recovery mechanism. If the section is long enough, the drastic change in temperature is avoided, making

axial conduction at the inlet negligible.

Future Work

The advances achieved in this work also raised new questions that need to be addressed in the future. There are three main areas that need to be addressed, as discussed below: 1) the correlation to calculate the time a system takes to reach steady state, 2) achieve a greater agreement between numerical and experimental results, and 3) modify the numerical model to simulate the dissociation receiver.

1) Time a System takes to Reach Steady State

The correlation found to estimate the time a system takes to reach steady state is only valid for a system for which the thermal mass of the wall is small. This is generally true for systems at low pressure because the thickness of the walls is small. However, for systems at high pressure (i.e. ammonia synthesis reactor at 30 MPa) the walls need to be thick resulting in high wall thermal mass. It was shown in Figure 22 that the time a system takes to reach steady state is linearly dependent on the thermal capacitance of the wall. If looking at the start-up of a system, one can predict that having a large wall thermal mass would increase the time it takes to bring the temperatures to steady state conditions. This is an important aspect that needs to be addressed. On this note, one can also then predict that the outer wall, which has a higher thermal mass, also becomes important. The numerical model can be modified to solve for an outer wall temperature as well. Once an outer wall has been incorporated in the model, it is trivial to include thermal losses to the environment. The correlation should be generalized to include scenarios when the wall thermal mass is large.

2) Modification of numerical model to analyze the dissociation receiver

The numerical model can be slightly modified to investigate the dissociation receiver in the system shown in Figure 25. Detailed modelling of the dissociation receiver was not part of the scope of this work; however, as part of this effort a model was developed to estimate the thermal efficiency of the receiver.

The dissociation receiver must be optimized to improve the thermal efficiency and reduce the cost of the system. A design for the dissociation receiver to improve the receiver efficiency was proposed by Cho et.al. [41]. Their idea was then modified for the ammonia dissociation receiver by Lavine et.al. [38], which consists of tubes filled with catalyst mounted in a series of tight skirts, as illustrated in Figure 50. The design was chosen to match the incident solar flux to the requirements of the reaction. From the perspective of enhancing receiver thermal efficiency, the tubes will be arranged with the lower temperature inlet conditions outermost and the higher temperatures towards the inside. One of the advantages of our system is that the reaction heat absorption can help maintain a lower temperature at the tip.

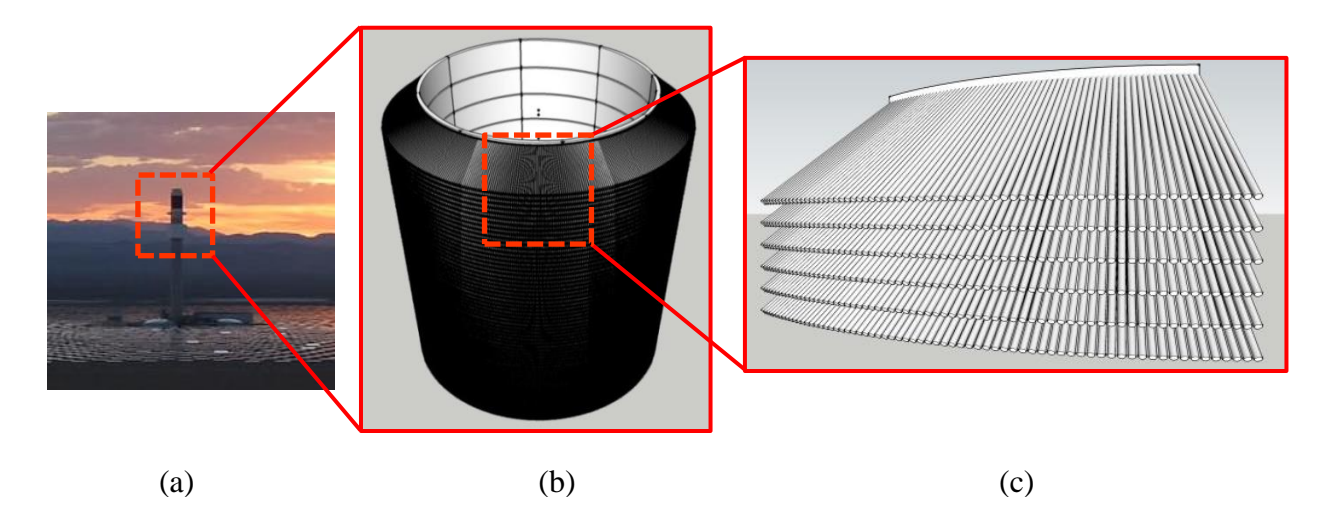


Figure 50 – (a) Tower receiver with (b) concept sketch of dissociation receiver and (c) close view of one of 80 individual panels

A numerical model that predicts the thermal losses and thermal efficiencies of the receiver was developed. Figure 51 shows the geometry assumed for the thermal losses calculations. The base and the tip temperatures are assumed to be constant, and linear temperature profile is assumed along the x-direction (see Figure 51). However, from the results shown in Chapter 4 for ammonia synthesis, we know that the temperature profile along the reactor won't be linear, especially if the losses are high. The numerical model described in Chapter 4 should be modified to obtain results for the reverse reaction.

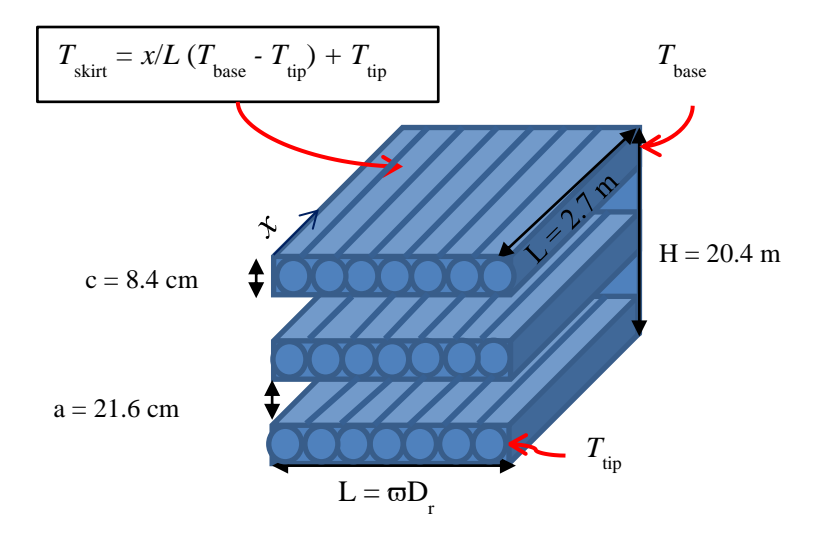


Figure 51 – Dimensions of the ammonia dissociation receiver, and the prescribed temperature at the base of the receiver, along the dissociator tubes, and at the tip of the tubes.

The initial configuration suggested here came close to the thermal performance of a molten salt based system (see Table 5). The results showed that the design of the ammonia dissociation receiver is promising. However, when making these calculations, several assumptions were made.

Table 5 – Dimensions of the ammonia dissociation receiver, and the prescribed temperature at the base of the receiver, along the dissociator tubes, and at the tip of the tubes.

	Molten	Dissociation
	Salt	
Thermal capacity	670 MW_t	670 MW_t
Minimum temperature	290 °C	450 °C
Maximum temperature	574 °C	700 °C
Radiation losses	19.5 MW _t	23.9 MW_{t}
Convection losses	17.3 MW_t	18.4 MW_{t}
Thermal efficiency	94.8%	94.1%

A more complete model needs to be developed to evaluate the feasibility of the receiver.

The reactor has not yet been optimized to increase efficiency and reduce cost. The proposed project would use the numerical model to find an optimum design for the dissociation receiver. The

dissociation receiver design must convert sufficient ammonia to meet the thermal power requirement and do so at reasonable operating temperature. Even though some work was done as part of this thesis on the dissociation receiver [42], the dissociation needs to be incorporated into the model. This can be done by merging the model that calculates the thermal losses on the receiver and the numerical model that predicts the temperature profiles inside the reactor.

References

- 1. Kakaç, S., A.E. Bergles, and F. Mayinger, *Heat exchangers: thermal-hydraulic fundamentals and design.* 1981: Hemisphere Pub. Corp.
- 2. Shah, R.K. and D.P. Sekulic, *Fundamentals of heat exchanger design*. 2003: John Wiley & Sons.
- 3. Stekli, J., L. Irwin, and R. Pitchumani, *Technical challenges and opportunities for concentrating solar power with thermal energy storage*. Journal of Thermal Science and Engineering Applications, 2013. **5**(2): p. 021011.
- 4. Ganapathi, G.B. and R. Wirz. High density thermal energy storage with supercritical fluids. in ASME 2012 6th International Conference on Energy Sustainability collocated with the ASME 2012 10th International Conference on Fuel Cell Science, Engineering and Technology. 2012. American Society of Mechanical Engineers.
- 5. Cima, R. and A. London, *The Transient Response of a Two-Fluid Counterflow Heat Exchanger—The Gas Turbine Regenerator*. Trans. ASME, 1958. **80**: p. 1169-1179.
- 6. London, A.L., D. Sampsell, and J.G. McGowan, *The Transient Response of Gas Turbine Plant Heat Exchangers—Additional Solutions for Regenerators of the Periodic-Flow and Direct-Transfer Types*. Journal of Engineering for Gas Turbines and Power, 1964. **86**(2): p. 127-135.
- 7. London, A., F. Biancardi, and J. Mitchell, *Transient Response of Gas Turbine Plant Heat Exchangers: Regenerators, Intercoolers, Precoolers, and Ducting.* 1958.
- 8. Rizika, J., Thermal lags in flowing incompressible fluid systems containing heat capacitors. Trans. ASME, 1956. **78**(7): p. 1407.
- 9. Yin, J. and M.K. Jensen, *Analytic model for transient heat exchanger response*. International Journal of Heat and Mass Transfer, 2003. **46**(17): p. 3255-3264.
- 10. Gvozdenac, D., *Analytical solution for transient response of counter flow heat exchanger with finite wall capacitance*. Wärme-und Stoffübertragung, 1993. **28**(6): p. 351-356.
- 11. Gvozdenac, D., Analytical solution of transient response of gas-to-gas parallel and

- counterflow heat exchangers. Journal of heat transfer, 1987. 109(4): p. 848-855.
- 12. Shah, R. Transient response of heat exchangers. in Conf. NATO Adv. Study Inst. Heat Exchangers: Thermal-Hydraulic Fund. & Design. 1980.
- 13. Bunce, D., *The Transient response of heat exchangers*. 1995, Rochester Institute of Technology.
- 14. Kandlikar, S.G., D.J. Bunce, and B.D. Cole, *Transient Performance of Parallel and Counter-flow Heat Exchangers with a Step Temperature Change on Minimum Capacity Rate Fluid Stream*, in *Symposium on Thermal Science and Engineering in Honor of Chancellor Chang-Lien Tien*. 1995: University of California, Berkeley.
- 15. Abbasi, K., et al. A Transient Model for Parallel Flow and Counter Flow Heat Exchangers. in ASME 2013 International Technical Conference and Exhibition on Packaging and Integration of Electronic and Photonic Microsystems. 2013. American Society of Mechanical Engineers.
- 16. Ferziger, J.H. and M. Perić, *Computational methods for fluid dynamics*. Vol. 3. 2002: Springer Berlin.
- 17. Versteeg, H.K. and W. Malalasekera, *An introduction to computational fluid dynamics: the finite volume method.* 2007: Pearson Education.
- 18. Pletcher, R.H., J.C. Tannehill, and D. Anderson, *Computational fluid mechanics and heat transfer*. 2012: CRC Press.
- 19. Fletcher, C., Computational Techniques for Fluid Dynamics, Vol. 1,(1988). Springer-Verlag.
- 20. Bergman, T.L., et al., Fundamentals of heat and mass transfer. 2011: John Wiley & Sons.
- 21. Incorpera, F.P., et al., Fundamentals of heat and mass transfer. John Wiley & Sons, 1996.
- 22. Dunn, R., K. Lovegrove, and G. Burgess, *A review of ammonia-based thermochemical energy storage for concentrating solar power*. Proceedings of the IEEE, 2012. **100**(2): p. 391-400.

- 23. Lovegrove, K., et al., *Developing ammonia based thermochemical energy storage for dish power plants.* Solar Energy, 2004. **76**(1): p. 331-337.
- 24. Richardson, J., S. Paripatyadar, and J. Shen, *Dynamics of a sodium heat pipe reforming reactor*. AIChE journal, 1988. **34**(5): p. 743-752.
- 25. Luzzi, A. and K. Lovegrove, A solar thermochemical power plant using ammonia as an attractive option for greenhouse-gas abatement. Energy, 1997. **22**(2): p. 317-325.
- 26. Kreetz, H. and K. Lovegrove, *Theoretical analysis and experimental results of a 1 kW*< sub> chem</sub> ammonia synthesis reactor for a solar thermochemical energy storage system. Solar energy, 1999. **67**(4): p. 287-296.
- 27. Lovegrove, K., A. Luzzi, and H. Kreetz, *A solar-driven ammonia-based thermochemical energy storage system.* Solar energy, 1999. **67**(4): p. 309-316.
- 28. Luzzi, A., et al., *Techno-economic analysis of a 10 MW e solar thermal power plant using ammonia-based thermochemical energy storage*. Solar Energy, 1999. **66**(2): p. 91-101.
- 29. Luzzi, A., et al., *Base-load solar thermal power using thermochemical energy storage*. Le Journal de Physique IV, 1999. **9**(PR3): p. Pr3-105-Pr3-110.
- 30. Lovegrove, K.M., *High pressure ammonia dissociation experiments for solar energy transport and storage*. International journal of energy research, 1996. **20**(11): p. 965-978.
- 31. Lovegrove, K., et al., *Exergy analysis of ammonia-based solar thermochemical power systems.* Solar energy, 1999. **66**(2): p. 103-115.
- 32. Lovegrove, K., H. Kreetz, and A. Luzzi, *The first ammonia based solar thermochemical energy storage demonstration*. Le Journal de Physique IV, 1999. **9**(PR3): p. Pr3-581-Pr3-586.
- 33. Kreetz, H., K. Lovegrove, and A. Luzzi, *Maximizing thermal power output of an ammonia synthesis reactor for a solar thermochemical energy storage system.* Journal of solar energy engineering, 2001. **123**(2): p. 75-82.
- 34. Kreetz, H. and K. Lovegrove, *Exergy analysis of an ammonia synthesis reactor in a solar thermochemical power system.* Solar energy, 2002. **73**(3): p. 187-194.

- 35. Lovegrove, K., Fortran implementation of a two dimensional pseudo homogenous packed bed catalytic reactor model. Energy Research Centre Technical Report ER-RR-62, Dept of Engineering, ANU, 1992.
- 36. Temkin, M. and V. Pyzhev, *Kinetics of ammonia synthesis on promoted iron catalysts*. Acta physiochim. URSS, 1940. **12**(3): p. 217-222.
- 37. Pioro, I.L., H.F. Khartabil, and R.B. Duffey, *Heat transfer to supercritical fluids flowing in channels—empirical correlations (survey)*. Nuclear engineering and design, 2004. **230**(1): p. 69-91.
- 38. A. Lavine, K.L., J. Jordan, G. B. Anleu, C. Chen, H. Aryafar, and A. Sepulveda, . Thermochemical Energy Storage with Ammonia: Aiming for the SunShot Cost Target. in SolarPACES 2015 Conference. 2015. Cape Town, South Africa.
- 39. C. Chen, H.A., G. Warrier, K.M. Lovegrove, and A.S. Lavine. *Ammonia synthesis system for producing supercritical steam in the context of solar thermochemical energy storage*. in *SolarPACES 2015*. 2015. Cape Town, South Africa.
- 40. Chen, C., et al. Design of an Ammonia Synthesis System for Producing Supercritical Steam in the Context of Thermochemical Energy Storage. in ASME 2015 Power Conference collocated with the ASME 2015 9th International Conference on Energy Sustainability, the ASME 2015 13th International Conference on Fuel Cell Science, Engineering and Technology, and the ASME 2015 Nuclear Forum. 2015. American Society of Mechanical Engineers.
- 41. Ho, C., J. Christian, and J. Pye, *Bladed solar thermal receivers for concentrating solar power*. 2014, USPTO.
- 42. Bran-Anleu, G., H.P. Kavehpour, and A.S. Lavine. *Transient Behavior of an Ammonia-Based Energy Recovery System*. in *10th International Conference on Energy Sustainability*. 2016. Charlotte, North Carolina, USA: ASME.